Chapter 1

Design and Fabrication of Biofunctional Magnetic Nanoparticles for Cancer Specific Targeting, Imaging and Therapy: A Brief Review and Perspective of the Present Work

1. 1 Introduction

The early genesis of **"nanomedicine"** germinates from the visionary idea of the late Nobel physicist Richard P. Feynman, according to which tiny nanorobots could be fabricated and introduced into the human body as miniature surgeons to execute cellular repairs at the molecular level [1]. Although the first brainwave of **Nanotechnology** comes from his famous lecture entitled "*There's Plenty of Room at the Bottom*," way back in 1959, the terminology was actually conceived by Norio Taniguchi and defined as the processes of separation, consolidation and deformation of materials on a molecular scale [2]. The term was later championed and popularized by K. Eric Drexler through speeches and books '*Engines of Creation: The Coming Era of Nanotechnology*' and '*Nanosystems: Molecular Machinery, Manufacturing, and Computation*'[3]. The term **'nanotechnology'**, derived from the Greek word '*nãnos*' meaning 'dwarf', is befittingly used to accentuate its fundamental premise of miniaturization. It can be broadly defined as the technology that deals with the creation and utilization of materials, devices, and systems through the control of matter on the spatial dimensions of less than 100 nanometers (1 nanometer = 1×10^{-9} meter). **Nanomedicine** refers to the medical application of nanotechnology, which deals with the monitoring, repair, construction and control of human biological systems at the molecular level, using engineered devices and nanostructures [1]. The small size and subsequent high surface to-volume ratio of these nanoparticulate systems translates into unique physical properties such as superparamagnetism, high yield and photostable luminescence or shape and size-tuneable opto-electronic properties, which are not available with their bulk counterparts. The reduction of basic "building blocks" to nanometer length scale (1-100 nm) gives rise to synthetic materials, which are capable of performing dimensionally relevant interactions with biological entities, from cells (10-100 μm), viruses (20-450 nm) and proteins (5-50 nm) down to genes (2 nm wide and 10-100 nm long). Interfacing nanostructures with these biological entities is a significant advance to resolve many key challenges being faced by the mankind which include the development of **(i)** fast and sensitive diagnostics such as "point-of-care" devices and wearable bio-sensors, **(ii)** bio-marker and drug delivery vehicles for early diagnosis, prognosis and treatment of complicated human diseases such as Atherosclerosis, Cancer, Parkinson's and Alzheimer's diseases as well as inflammatory and infectious diseases (e.g. H.I.V.) and **(iii)** the development of nanomaterial-based scaffolds and biomimetic nanostructures for tissue engineering and long-lasting, artificial implants.

Over the last few years, significant efforts have been devoted towards the successful exploitation of nanotechnology for diagnosing and treating complex diseases at the cellular and molecular level. Taking Feynman's original vision of medical nanorobotics to heart, nanomedicine have pronged into hundreds of directions, each of them exemplifying the key perception that structuring materials at the molecular scale can bring enormous immediate benefits in medical research and practices.

1. 2 Nanomedicine and Cancer

Cancer is a class of complex diseases in which a group of cells display uncontrolled growth or proliferation, invasion and sometimes metastasis. The apparent impenetrability of the disease largely owes to multiple, often redundant, pathways that appear to evolve through the genetic instability of cancer cells. Despite some recent progresses in the field of cancer therapeutics, majority of cases are still diagnosed, only after the tumor have metastasized, leaving the patient with a bleak prognosis. Moreover, as far as cancer therapeutics is concerned, traditional chemotherapy lack efficacy due in part to the drug's non-specific targeting and bio-distribution, hydrophobicity and poor oral-bioavailability. Nanotechnology has a tremendous potential to circumvent the current obstacles in cancer therapies and revolutionize the way cancer is diagnosed, imaged and treated. With the aid of nanoparticulate probes, not only lesions can be detected at cellular and molecular level but nano-delivery vehicles can be effectively used to deliver drugs with poor aqueous solubility and low permeability as well as unstable drugs and drugs undergoing extensive first pass metabolism to the target pathological zone, while sparing the adjacent normal cells.

Over the last few years, substantial interest has been devoted towards the designed fabrication of nanometer-sized targeted probes for cancer-specific targeting, imaging and therapy. A variety of functional nanostructures such as polymeric and lipid nanoparticles, hydrogels, micelles, liposomes, dendrimers, superparamagnetic nanoparticles, quantum dots, noble metal nanorods, and nanoshells have come to the fore to potentially revolutionize bio-medicine. Intelligent combinations of different nanostructured materials with different properties can offer synergetic multifunctional nanomedical platforms, which make it possible to accomplish multimodal imaging and concurrent diagnosis and therapy. For example, the combination of magnetic resonance imaging (MRI) contrast agent and fluorescent organic dye can allow the

detection of cancer through non-invasive MRI and the optical guide of surgery. Similarly, co-encapsulation of MRI contrast agent and anticancer drug in a nanostructured matrix has the potential to allow for simultaneous diagnosis and targeted chemotherapy. To further bequeath specific targeted imaging and therapeutic properties into a single system, high affinity tumor-specific ligands or monoclonal antibodies can be conjugated on the surface of these multifunctional nanoparticles. There are many possible combinations of the various imaging and therapeutic modalities. Such multifunctional therapeutic devices lead towards the concept and possibility of personalized, theragnostic (a fusion of therapeutics and diagnostics) nanomedicines for potential early detection of cancer lesions, determination of molecular signatures of the tumor by noninvasive imaging and molecularly targeted cancer therapy.

1.3 Magnetic Nanoparticles in Biomedicine

1.3.1 Magnetism in Medicine: Background

The history of magnetism in medicine is pretty old and is punctuated with astounding anecdotes regarding the pioneering work of physicians and physicists, as well. The first medical use of magnetite powder for internal applications dates back to the 10^{th} century A.D., when the Egyptian physician and philosopher Avicenna recommended the use of one magnetite grain as an antidote for the accidental swallowing of rust [4]. Taken with milk, the magnetite was believed to render the poisonous iron inert by attracting it and speeding up its excretion through the intestine. An earlier use of magnetic force consisted in the removal of iron particles embedded in eye [5]. More recently, with miniaturization of electromagnets, development of superconducting electromagnets and introduction of strong permanent magnets (Sm–Co and Nd–Fe–B), the medical use of magnets became indispensable in fields as diverse as dentistry, cardiology, neurosurgery, oncology, radiology, etc. Although the early research in this field can be dated back as old as several decades, the recent surge of interest in nanotechnology has significantly expanded the breadth and depth of the magnetic nanoparticle research.

1.3.2 What are Magnetic Nanoparticles?

Magnetic nanoparticles (MNPs) are a class of nanoparticles (i.e. engineered particulate materials of size < 100 nm) that can be manipulated under the influence of an external

magnetic field. MNPs are commonly composed of magnetic elements, such as iron, nickel, cobalt and their oxides. Although a variety of magnetic nanostructures based on metallic iron, cobalt, nickel as well as their oxides have currently come to the fore, iron-oxide nanoparticles are superior to others for their ease of synthesis, stability, outstanding superparamagnetic properties or lack of magnetic memory and more importantly, their favorable biocompatibility and biodegradability. Upon metabolism, iron ions are added to the body's iron stores and in due course incorporated by erythrocytes as hemoglobin, allowing for their safe use in vivo [6]. In view of all these, superparamagnetic iron-oxide nanoparticles based on magnetite or maghemite have been currently realized as one of the most popular multifunctional nanomagnetic materials with potential *in-vitro* and *in-vivo* applications (**Fig. 1.1**) including magnetic bio-separation, cell-sorting, immunoassay, sensing, magnetic resonance imaging (MRI) contrast enhancement, targeted drug delivery and magnetic fluid hyperthermia (MFH) for selective destruction of cancer cells [7-10].

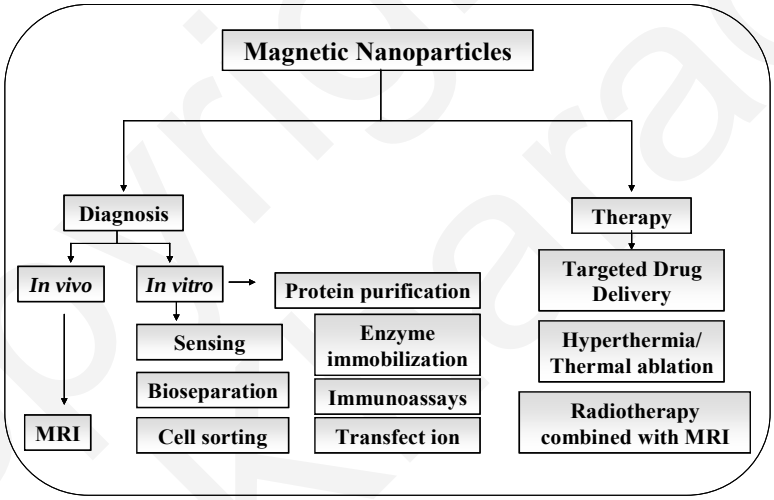

Fig. 1.1: The application of magnetic nanoparticles in biomedicine

To better address explicit biological and clinical requirements, iron-oxide nanoparticles (MNPs) with controllable size, morphology, narrow size distribution, higher magnetic moments and tailored surface chemistry are under intense development for applications in the detection, diagnosis, and treatment of malignant tumors, cardiovascular diseases and various neurological syndromes. By integrating highly specific targeting agents and other functional ligands such as fluorophores, permeation enhancers and cell-targeting antibodies or peptides

through a process commonly referred to as "**bio-functionalization"**, the applicability and efficacy of these MNPs have significantly augmented.

This chapter is planned to provide the readers with an overview of the recent advancements related to the design and fabrication of tailored, biofunctional magnetic nanoparticles for cancer diagnosis and therapy. Such a description cannot be completed without a thorough understanding of the problems involved from the perspective of their overall requirements, for their synthesis as well as bulk and surface properties. Starting with some well-known basic concepts related to the physics of magnetic nanomaterials, the present discussion expands its depth and breadth towards the design, synthesis and functionalization of MNPs for cancer-targeted imaging and drug delivery. The main objective of this contribution is to convey information about both the state of the art as well as the need for further progress and clinical development.

1. 4. Basic Concepts

1. 4. 1. Classification of Magnetic Materials

Magnetism is originated from magnetic dipole moments generated by the spin and orbital angular momenta of electrons in atoms or ions. Materials are classified as **diamagnetic, paramagnetic, ferri-** and **ferromagnetic**, based on their volumetric magnetic susceptibility (χ), which is defined by the ratio of the induced magnetization (M) to the applied magnetic field [11] **(H)** (**Eq. 1.1**).

$$\mathbf{M = \chi H} \qquad \textbf{Eq. 1. 1}$$

In **diamagnetic** materials, the magnetic moment being antiparallel to H, results in very small and negative susceptibilities of the order -10^{-6} to -10^{-3}. On the other hand, materials with magnetic moments aligned parallel to **H** and susceptibilities on the order of 10^{-6} to 10^{-1} are described as **paramagnetic** [**Fig. 1. 2 (a)-(b)].** They do not retain magnetic properties when the external field is removed. In case of **ferromagnetic, antiferromagnetic** or **ferrimagnetic** materials, magnetic moments align parallel to **H** as usual but coupling interactions between the electrons within the material result in ordered magnetic states, i.e., magnetic domains, and consequently large spontaneous magnetization. The susceptibilities of these ordered materials

not only depend on their atomic structures or temperature but also the external field *H*, which gives rise to the characteristic sigmoidal shape of the **M–H** curve, with **M** approaching saturation at large values of **H**. Hysteresis, which essentially refers to an irreversibility in the magnetization or demagnetization process, is observed in the **M–H** curve for ferro- and ferromagnetic materials. A few important magnetic properties can be derived from the hysteresis curve such as saturation magnetization ($\mathbf{M_s}$), remanence ($\mathbf{M_r}$) and coercivity ($\mathbf{H_c}$) [**Fig. 1. 2 (c)**]. $\mathbf{M_r}$ refers to the value of magnetization corresponding to a zero magnetic field, and $\mathbf{H_c}$ is the magnetic field required to reduce remanent magnetization to zero.

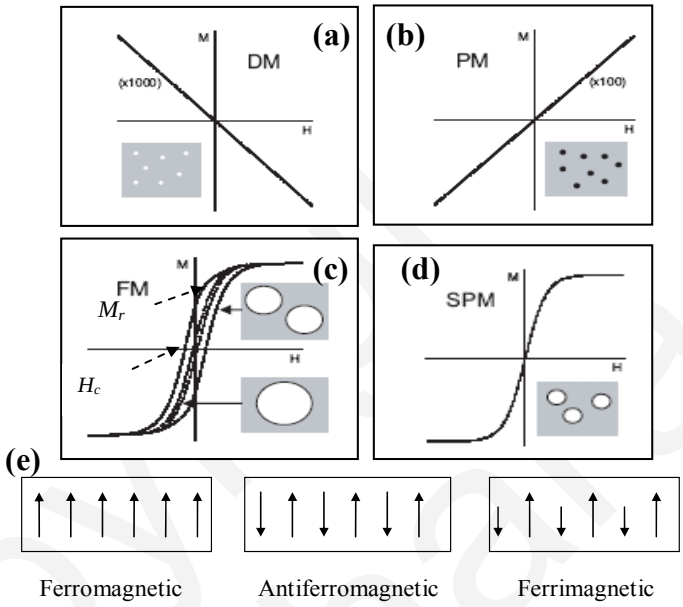

Fig. 1.2: Magnetic responses of **(a)** diamagnetic (DM) **(b)** paramagnetic (PM) **(c)** ferromagnetic (FM) and **(d)** superparamagnetic (SM) materials, adopted from [11] **(e)** illustration of alignment of magnetic moment in ferromagnetic, antiferromagnetic and ferrimagnetic materials.

1. 4. 2 Superparamagnetism: A Nanoscale Phenomenon

In non-magnetized ferromagnetic materials, magnetic domains (so called Weiss-domains) at short range are aligned, but at long range adjacent domains are anti-aligned. The transition between these two domains is called a Bloch wall [12]. At the nanometer length scale (on the order of tens of nanometer), Bloch wall formation becomes thermodynamically unfavorable leading to the formation of single domain crystals, which are classified as **superparamagnetic** .The term superparamagnetism refers to the characteristic strong paramagnetic nature of the particles at this critical size range. As compared to strictly paramagnetic materials, superparamagnetic materials such as SPIO have larger susceptibilities

owing to their existence as single domain crystals. Superparamagnetism, which is marked by the lack of coercivity and remnanance in an anhysteric but sigmoidal **M-H** curve [presented in **Fig. 1.2 (d)**], enables the particles to maintain their colloidal stability and avoid aggregation, making it feasible for their use in biomedical applications.

Although superparamagnetism is a favorable property of small particles, the consequence of particle size diminution is far-reaching. Reduction in particle size leads to increasing surface-to-volume ratios resulting in pronounced surface effects such as noncollinear spins, spin canting, and spin-glass-like behavior, which can significantly affect the magnetic properties of the material [13]. Typically, the saturation magnetization (M_s) values of nanoparticles, corresponding to the complete alignment of all individual moments in a sample, are smaller than their corresponding bulk phases. This, however, can be attributed to the disordered crystal structure resulting from their high surface curvature, which increases with particle size reduction. In addition, the same nanoparticle composition, prepared via different chemical routes may exhibit significant differences in magnetic properties. More detailed explanations of the physical properties of MNPs and nanoscale magnetic phenomena have been reviewed elsewhere [13-14].

1. 5. Synthesis of iron-oxide nanoparticles

A biomedical MNP platform has to fulfill certain physicochemical, physiological and pharmacological requirements and hence choice of a suitable synthesis method is crucial in designing functional MNPs for biomedical applications. Ideally, such a platform should comprise of particles with uniform shape, size and low polydispersity, demonstrate superparamagnetism and high magnetic strength, should have specific peripheral recognition ability for ligand attachment, high aqueous dispersion stability and low cytotoxicity.

Two types of iron-oxide are currently under Phase III clinical trials: superparamagnetic iron-oxide or **SPIO** with average diameter over 40 nm and ultrasmall superparamagnetic iron-oxides or **USPIO** with average diameter lower than 40 nm also called **MIO** for **M**onocrystalline **I**ron **O**xide. Typically composed of a biocompatible, coating-stabililized, nanocrystalline magnetite (Fe_3O_4) or maghemite (γFe_2O_3) core, these ferrite nanoparticles possess an inverse spinel crystal structure with oxygen ions forming a close-packed cubic lattice and iron ions located at interstices. In the case of Fe_3O_4, magnetization arises from electron hopping between the co-existing Fe^{2+} and Fe^{3+} ions at the octahedral sites.

A variety of chemical routes have been successfully utilized to prepare well-dispersed MNPs ranging from traditional wet chemistry solution based routes viz. co-precipitation or reverse-micelle based synthesis to more exotic gas-phase techniques such as laser pyrolysis, spray pyrolysis and flame synthesis [15-17]. Although gas phase routes for MNP synthesis are fast and highly scaleable, their suitability for biomedical applications is yet to be explored.

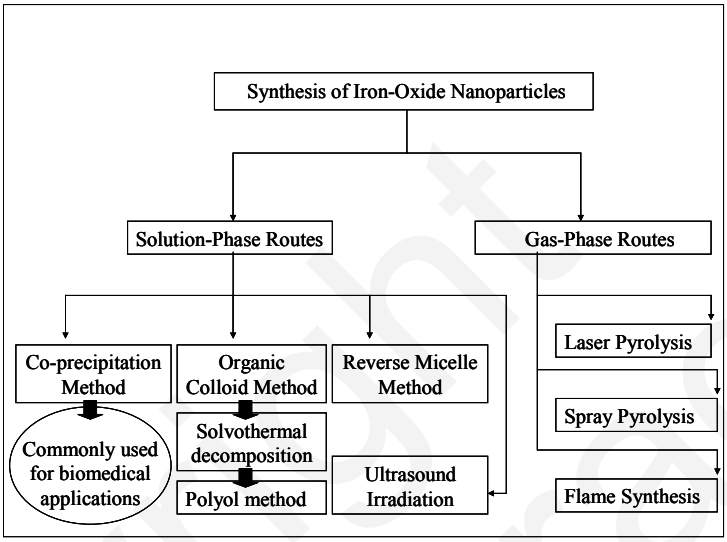

Fig. 1.3: Synthesis of iron-oxide nanoparticles via different chemical routes

Currently, most of the SPIO and USPIO based formulations are predominately synthesized in a one-step process by alkaline coprecipitation of iron (II) and iron (III) precursors in presence of a coating material [18-19]. The overall reaction of magnetite co-precipitation can be written as

$$Fe^{2+} + 2Fe^{3+} + 8OH^- \rightarrow Fe_3O_4 + 4H_2O \qquad \textbf{Eq. 1.2}$$

The use of a coating material **(i)** efficiently control the magnetic core growth during the synthesis, **(ii)** stabilize the nanoparticle dispersion in water and later in physiological medium via steric and/or electrostatic repulsions and **(iii)** reduce the opsonisation process *in vivo.* The control of size, shape and composition of nanoparticles depends on the type of salts used (e.g. chlorides, sulphates, nitrates, perchlorates, etc.), Fe^{2+} and Fe^{3+} ratio, pH and ionic strength of the media. Because of its ease in dealing and scaling up, co-precipitation method is the most common route for the large-scale synthesis of magnetite nanoparticles. Except for the work described in **Chapter 5**, throughout the entire course of this dissertation, the tailored MNPs that have been used for targeting or destroying cancer cells have been synthesized via co-precipitation method with minor modifications, wherever necessary.

Apart from co-precipitation method, the recently developed organic colloid method, based on the decomposition of organometallic iron precursors in presence of high-boiling nonpolar solvents provides an effective approach to synthesize iron-oxide nanoparticles with significant improvements in size control, size distributions, and crystallinity [20-21]. In this process, the size of the nanoparticle is controlled by changing the reaction temperature or varying the metal precursor. Sizes can be fine-tuned by a seed-mediated growth process to obtain larger particles. For example, Sun et al. reported the synthesis of highly uniform magnetite nanoparticles with size variation within 2 nm and mean diameters from 4 to 20 nm through Fe-acetylacetonate decomposition in phenyl ether [20]. One limitation of this approach is the use of hydrophobic oleic acid and oleylamine surfactants, which results in a hydrophobic coating on the particle surface, demanding additional modification to improve the dispersibility of the MNPs in aqueous medium. Approaches involving the addition of an amphiphilic polymer or surface surfactant exchange have been utilized to overcome this problem [22].

In connection with the synthesis of nanoparticles by solvothermal reduction of metal salts, the **polyol-approach** deserves special mention. Polyol process is a versatile chemical approach, which refers to the use of polyols (for example ethylene glycol or diethylene glycol) for the reduction of metal salts to metal nanoparticles [23]. The polyols in this method often serve as high-boiling solvent and reducing agent in addition to working as a stabilizer. MNPs, synthesized via polyol approach exhibit many desired properties such as narrow size distribution, superparamagnetism and good water-solubility, which makes them promising candidates for a diverse array of biomedical applications.

Although polyol approach has been successfully exploited in the generation of metal or metal-oxide nanostructures with controllable size and morphology, disadvantages are that it needs a long time (at least 7-8 h), high temperature (>200°C) and most of the reports embarking on the polyol synthesis of magnetite nanoparticles to date cannot proceed without the introduction of inert Ar or N_2 in the reaction mixture. To circumvent this problem, a small part of the present dissertation has been dedicated to the process development of existing polyol chemistry focusing on the synthesis of highly biocompatible and water-dispersible, amine functionalized magnetite nanoparticles, using a low-temperature, air-assisted polyol process. The synthesis, characterization and in-vitro studies of the synthesized magnetite nanoparticles have been detailed in **Chapter 5.**

1.6 Biomedical application of MNPs: Physical Background

The most important in vivo applications of MNPs include magnetic resonance imaging (MRI), magnetic fluid hyperthermia (MFH) and magnetic drug targeting (MDT). In this section, we briefly explain the physical background of MRI and MFH.

1.6.1 Magnetic resonance imaging: The underlying physical principles

Magnetic resonance imaging is a powerful clinical imaging technique that allows for noninvasive tomographic visualization of anatomic structures with high spatial resolution and soft tissue contrast. Of the existing noninvasive diagnostic tools such as Computed Tomography (CT), Positron Emission Tomography (PET), Single Photon Emission CT (SPECT), Ultrasound and optical imaging, MRI is currently the most sensitive and preferred cross-sectional imaging modality in most diseases of the brain, spine and musculoskeletal systems.

A major portion of all living bodies constitute water molecules, each of which contains two hydrogen nuclei or protons. MRI is based on the NMR signal of these protons through the combined effect of a strong static magnetic field $\mathbf{B_0}$ and a transverse radiofrequency-field (rf-field) [11]. When a person goes inside the powerful magnetic field of an MRI scanner, these protons align with the direction of the field. A second radio frequency electromagnetic field is then briefly turned on causing the protons to absorb some of its energy. When this field is turned off, the net magnetization vector is once again influenced by $\mathbf{B_0}$ and tries to re-align with it along the longitudinal axis, while the protons attempt to release the absorbed energy and return to a state of equilibrium. This phenomenon termed as relaxation, can be divided into two different independent processes:

- **Longitudinal relaxation:** Longitudinal relaxation is the return of longitudinal magnetization in alignment with $\mathbf{B_0}$ and is termed *T_1-recovery*. Since the hydrogen atoms release the previously absorbed energy to the surrounding tissue (lattice) in their attempt to re-align with $\mathbf{B_0}$, *T_1 recovery* is also referred to as **'spin–lattice'** relaxation.

- **Transverse relaxation:** Transverse relaxation is the vanishing of transverse magnetization and is termed T_2 *-decay*. During the rf-pulse, hydrogen nuclei spin in phase with each other. After the rf-pulse, the magnetic fields of all the nuclei interact with each other. Consequently, energy is exchanged between those nuclei. Phase coherence is lost and the nuclei spin in a random fashion. Since T_2 decay results from the exchange of energy between spinning protons, it is referred to as **'spin–spin'** relaxation.

Based on their differences in T_1 and T_2 relaxation properties, tissues can be differentiated. In order to correlate the signal to its spatial origin, at least one of the two fields (i.e. B_0 or the rf-field) has to vary over space. Relaxation data are collected by a computer, which applies a two-dimensional Fourier transform to give the amplitudes of NMR signals, thereby permitting the reconstruction of the 3-D images. By adjusting the sequence parameters such as the repetition time TR (elapsed time between successive rf excitation pulses) and the delay time TE (time interval between the rf-pulse and the measurement of the first signal), the desired type of image contrasts are obtained.

While short TRs increase T_1 effects, long TRs allow tissues to reach complete longitudinal magnetization, thereby reducing T_1 effects. On the other hand, short TEs minimize T_2 effects of tissues whereas long TEs allow the loss of transverse signal, enhancing T_2 effects. Therefore T_1-weighted imaging is obtained by utilizing a short TR and a short TE whereas T_2-weighted imaging is achieved by employing long TRs and long TEs. Fluids, in general, have a very long T_2 and they are frequently associated with pathologies, e.g. internal injuries, cancer lesions, etc., so T_2-weigted images are generally preferred for such diagnostics [11].

In certain clinical situations, tissues cannot be differentiated on the basis of their intrinsic difference between T_1 and T_2 relaxation properties. In such cases, an **exogenous contrast media** need to be applied for a better delineation of tissues. The first generation of MRI contrast agents consists of T_1-agents i.e. high spin paramagnetic ions, usually Gd^{3+} in very stable chelate form obtained through complexation by low molecular weight chelating molecules such as diethylenetriaminepentaacetic acid (DTPA). Although Gd-DTPA shows a strong T_1 shortening effect and is widely accepted in clinics, it has relatively low contrast effects and a very short retention time *in vivo* [24-25]. In addition, the toxicity and biocompatibility of gadolinium during and after endocytosis by cells are not clearly known. Recently, magnetic iron oxide nanoparticles (MNPs) have emerged as a new class of target-

specific MRI T_2 contrast agents with much better efficiency than Gd-DTPA as relaxation promoters and their magnetic properties can be manipulated by controlling the sizes of core and nature of surface coating. Moreover, MNPs have a long blood retention time, excellent biocompatibility and biodegradability, which make them a promising platform for targeted imaging and therapy.

1.6.2. Magnetic Fluid Hyperthermia: Physical background

Cancer cells are less tolerant to heat as compared to normal cells. The concept of applying local "**hyperthermia**" (a Greek word for overheating) for cauterization of surface tumors is as old as medicine itself. Today, hyperthermia remains a potential form of cancer therapy aside from the well-known methods of surgery, chemotherapy and radiotherapy. Two kinds of heating treatments are currently distinguished: (mild) hyperthermia, which is performed between 41° and 46° C to stimulate the immune response for non-specific immunotherapy of cancers, and thermoablation (more than 46° C, up to 56° C) leading to tumour destruction by direct cell necrosis, coagulation or carbonisation.

Magnetic Fluid Hyperthermia (MFH) is based on the heating of nanoscale mediators in the form of intravenously injectable colloidal dispersion of magnetic particles [26]. The origin of magnetic heating via inductive mediators essentially depends on the size and the magnetic properties of particles. In case of multidomain ferro- or ferrimagnetic materials, heating is due to hysteresis losses. Large particles of such materials comprise of numerous sub-domains, each of them having an explicit magnetization vector. On exposure to a magnetic field, the domain with magnetization direction aligned along the magnetic field axis grows while the other ones shrink. This phenomenon, called "domain wall displacements" is not reversible, i.e. magnetization curves for increasing and decreasing magnetic field amplitudes do not coincide. Under this circumstance, the material is said to exhibit a "hysteresis behavior" and produces heat under AC magnetic field. In sub-domain particles (superparamagnetic particles) no heating due to hysteresis losses can occur because there is no domain wall. In this case, energy is supplied by an external AC magnetic field, which assists magnetic moments to rotate in overcoming the energy barrier, given by Eq. **1.3**

$$E = KV \qquad \textbf{Eq. 1.3}$$

where *K* is the anisotropy constant and *V* is the volume of the magnetic core. This energy is dissipated when the particle moment relaxes to its equilibrium orientation (Néel relaxation). For ferro-/ferri- as well as superparamagnetic particles, heating can originate out of the rotational Brownian motion within a carrier liquid. In this case, the energy barrier for re-orientation of a particle is determined by rotational friction within the surrounding liquid i.e. the rotation of the magnetic particle as a whole because of the torque exerted on the magnetic moment by the external AC magnetic field. Irrespective of the origin of heating, specific absorption rate (SAR), also termed specific loss power, is defined as the power of heating of a magnetic material per gram and expressed as:

$$\mathbf{SAR = C\,\Delta T/\Delta t} \qquad \textbf{Eq. 2.4}$$

where **C** is the specific heat capacity of the sample (J/g/K) and **ΔT/Δt** is the initial slope of the temperature versus time dependence. Most of magnetic hyperthermia experiments are performed with laboratory-made generators in the frequency range of 50 kHz to 1 MHz, with magnetic field amplitudes up to few tens of mT, using an induction coil or in the air-gap of a magnetic inductor. A full sized human prototype of such AC generator has been built by MFH Hyperthermiesystem GmbH (Berlin) and recently used for first clinical trials.

1.7 Surface functionalizations of MNPs for biomedical applications

1.7.1 Why surface modification is necessary?

For biomedical applications, the size, charge and surface chemistry of magnetic nanoparticles is particularly important, as it plays a significant role in the biokinetics, bio-distribution and bioavailability of nanoparticles in vivo [27]. Due to anisotropic dipolar attraction, arising out of large surface area to volume ratio, unmodified magnetic nanoparticles of iron oxide tend to aggregate into large clusters. The clusters formed by agglomerated nanoparticles not only loose the specific properties associated with the single domain but are also non-biocompatible. These agglomerated nanoparticles have a very short circulation time in blood and are rapidly cleared by macrophages of the mononuclear phagocytic system (MPS), immediately after intravenous administration[28]. The mononuclear phagocyte system (MPS), also known as the reticuloendothelial system (RES) comprises of a family of cells, which include the bone marrow progenitors, blood monocytes and tissue macrophages (such as Kupffer cells in the liver). These macrophages are widely distributed and strategically placed in many tissues of the body. They have the unique capacity to clear and recognize senescent

cells as well as invading micro-organisms or particles. The first step of the clearance mechanism involves opsonization. Opsonins are circulating plasma proteins, which include various sub-classes of immunoglobulins, complement proteins, fibronectin etc. These opsonins adsorb spontaneously onto the surface of any invading entity. Particle recognition is promoted through the interaction of opsonins with the specialized plasma membrane receptors on monocytes and macrophages. On exposure to blood, particles of different size, morphology and surface characteristics (viz. charge, surface chemistry, hydrophilicity/ hydrophobicity etc.) attract different arrays of opsonins, the content and conformation of which may influence the rate and site of particle clearance from the blood compartment. For example, the smaller, the more neutral and the more hydrophilic the particle surface, longer is its plasma half-life. The subsequent step consists of endocytosis/ phagocytosis of the particles by the circulating monocytes or the fixed macrophages, leading to their elimination from circulation and their simultaneous accumulation in organs with high phagocytic activity. Therefore, after i.v. administration, MNPs are cleared up within minutes from the bloodstream and their typical final bio-distribution is around 60–90% in the liver, 5–8% in the spleen and 1–2% in the bone marrow. Effect of size and other parameters on the bio-distribution of MNPs have been detailed in **Section 1.10.2.** Summarily, avoidance of MPS attack is the key goal towards the synthesis of long circulating MNPs. For this purpose, MNPs require protective coatings, which should ideally have a high affinity for the iron-oxide core, are nonimmunogenic, nonantigenic, and capable of evading opsonin attack.

1.7.2 Surface coatings and functionalizations

Common biocompatible coatings include lipids, liposomes, proteins, dendrimers, synthetic as well as natural macromolecules (bio-polymers) or inorganic matrices such as gold, silver, gadolinium or silica. Small molecules such as alkoxysilanes, alkyl phosphates and phosphonates, bisphosphonates, amino acids or mercaptosuccinic acid are also used.

1.7.3.1 Polymeric Coatings

Polymeric coatings afford a steric barrier to prevent nanoparticle agglomeration, reduce complement activation and evade the opsonization process in vivo. Some critical aspects with regards to polymeric coating that determine the ultimate performance and fate of MNPs *in*

vivo include [8]: **(i)** Hydrophilic/hydrophobic nature and/or biodegradation characteristics of the polymer; **(ii)** The length or molecular weight of the polymeric chain; **(iii)** The manner in which the polymer is attached/anchored onto the NP surface (electrostatic/covalent bonding); **(iv)** The conformation of the polymer; **(vi)** The degree of particle surface coverage. The molecular weight and geometric orientation of the polymer on the surface of the MNPs in different forms such as loops, trains, tails, end-grafted brushes or as fully encapsulated polymer shells not only affect their antifouling characteristics, but significantly contribute to their effective hydrodynamic size, which plays a key role in avoiding recognition by the RES.

A variety of polymeric coatings for MNP surface has been investigated which include polyethylene glycol (PEG), poloxamers, poloxamines, polyacrylamide and polysaccharide based materials viz. starch, cellulose, or dextran. Dextran-coated iron oxide nanoparticles have become an important part of clinical cancer imaging and have been shown to increase the accuracy of cancer nodal staging. These nanoparticles have also been effectively used to delineate primary tumors, image angiogenesis and detect metastases. Modification of dextranated iron oxide with targeting ligands, such as antibodies has also been accomplished [29], with an aim to increase the affinity of the nanoparticles for their target tissues. It is quite interesting to note that most clinical preparations have been based upon dextran or similar carbohydrate coatings, partly due to their previous use as plasma expanders, and also their intrinsic affinity for iron oxide, although one recent preparation has described the use of citrate-stabilized particles [30]. Cross-linked iron-oxide or CLIO prepared through cross-linking (caging) of the dextran and its subsequent amination facilitates further bio-functionalization via amide bond formation [31]. It also offers superb stability under harsh conditions without a change in size, blood half-life, or loss of its dextran coat, which makes them a promising probe for MR imaging and drug delivery applications.

Poly (ethylene glycol) (PEG) is another extensively used polymer for nanoparticle coating in biomedical applications. Surfaces covered with PEG have been proven to be nonimmunogenic and aid in enhancing the stealth character of the nanoparticles. Several methods have so far been utilized to attach PEG to MNPs including silane grafting to oxide surfaces, polymerization at the surface of MNPs and modification through sol–gel approaches. Kohler et al. developed bifunctional PEG silanes, which formed self-assembled monolayers (SAMs) on the surface of MNPs via condensation. Terminal amine or carboxyl groups extending out from the nanoparticle surface provided complementary sites for conjugation with functional ligand such as folic acid[32]. More recently, stealth MR probes

comprising of SPIONs modified with a protein or cell-resistant polymer such as poly (TMSMA-r-PEGMA) has been developed [33]. Polymer coating was either done in situ during nanoparticle precipitation or separately after the formation of iron-oxide core. When these anti-biofouling polymer coated SPION s were incubated with macrophage cells, uptake was significantly lower in comparison to that of the popular contrast agent, Feridex I.V., suggesting that the polymer-coated SPIONs can be long-circulated in plasma while resisting uptake by the MPS organs. Indeed, when the coated SPIONs were administered to tumor xenograft mice via i.v. injection, the tumor could be detected in T_2-weighted MR images within 1 h as a result of target-specific accumulation of the nanomagnets into the tumor site.

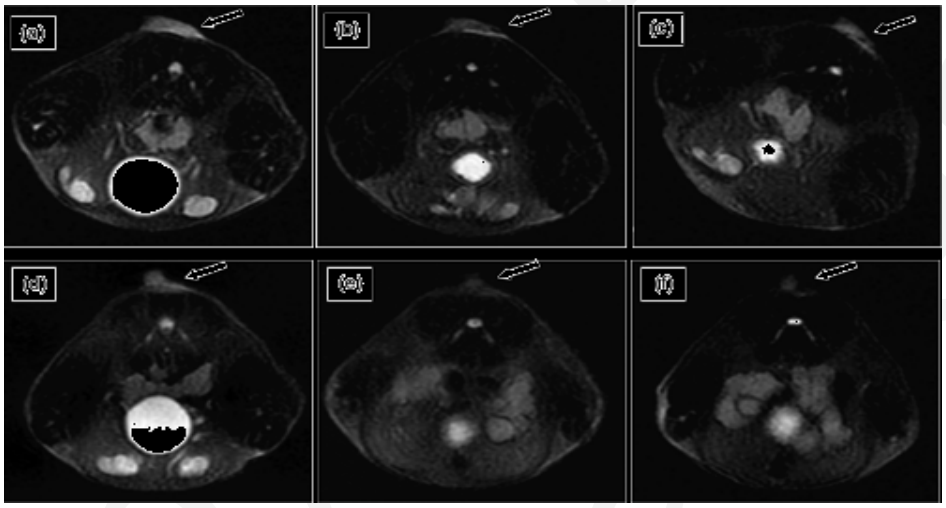

Fig. 1.4: T_2-weighted fast-spin-echo images (TR/TE of 4200 ms/102 ms) taken at 0, 1, and 4 h postinjection of 15 mg/kg of IS-SPION (**a**, **b**, and **c**) and 13 mg/kg of SW-SPION (**d**, **e**, and **f**) at the level of the tumor on the back of mice, adopted from [33]. "IS" and "SW" are used to denote SPIONs formed through "in situ" and "stepwise" methods respectively. T_2-weighted images (**b** and **e**) at 1 h postinjection of SPION show a marked signal drop at the tumor areas compared with those of 0 h (**a** and **d**). The arrows denote xenograft tumors.

1.7.3.2 Liposomes and Micelles

The development of liposomes as drug delivery vehicles can be regarded as one of the earliest forms of nanomedicine. These phospholipid bilayered membrane vesicles ranging from 100 nm-5 μm in size have been utilized for the delivery of small molecules, proteins and peptides, DNA, and MR imaging contrast agents. Liposomes can encapsulate a large number of MNP cores and deliver them to the target site together, avoiding dilution. Integration of

therapeutic agent in the payload further improves the multifunctionality of these delivery vehicles. Similarly, multifunctional micelles formed with amphiphilic block copolymers have also been used to entrap MNPs for drug delivery applications. Martina et al. developed magnetic fluid-loaded liposomes (MFLs) by encapsulating maghemite nanocrystals within unilamellar vesicles of egg phosphatidylcholine and DSPE-PEG_{200} [34]. MFLs with hydrodynamic size of 195 ± 33 nm were formed by film hydration coupled with sequential extrusion. These MFLs were capable of encapsulating up to 1.67 mol of iron per mol of lipid. MR angiographic evaluation in mice demonstrated that these MFLs were still present in the blood after 24 h of intravenous injection, corroborating their long-circulating behavior. More recently, fluorescently tagged, cationic magnetoliposomes containing 3.33 % 1, 2-distearoyl-3-trimethylammoniumpropane (DSTAP) with a positive zeta-potential of 31.3+/-7.3 mV have been evaluated for stable, long-term intracellular labelling without producing any cytotoxic effect. These bio-nanocolloids showed high intracellular uptake through clathrin-mediated endocytosis, following an endosomal pathway. Once internalised, MLs are not actively exocytosed and remain within the cell, which results in a highly persistent label, which can be detected, even in highly proliferative 3T3 fibroblasts, for up to at least one month [35].

1.7.3.3 Magnetodendrimers

Dendrimers have well-defined structure, compact globular shape, size monodispersity and controllable 'surface' functionalities, which make them excellent candidates for evaluation as drug carriers or imaging agents. The use of dendrimers in medical imaging rests mainly on the fact that they have a multiplicity of reactive chain ends. This allows a large number of contrast agents or drug moieties to be introduced onto a single molecule in a controllable manner, thereby enhancing the diagnostic or therapeutic efficiency. The availability of magnetodendrimers opens up the possibility of MR tracking of a wide variety of (stem) cell transplants including human neural stem cells (NSCs) and mesenchymal stem cells (MSCs) [36]. Cellular labeling, initiated through a nonspecific membrane adsorption process with subsequent intracellular (non-nuclear) localization in endosomes enables ready detection *in vivo* through MR imaging.

1.7.3.4 Core-shell nanostructures

Apart from the polymer-based modifications discussed above, the use of inorganic matrices such as silica, gold, silver and gadolinium to form core-shell nanoparticle designs have also been reported. Such core shell MNP s are composed of a functionalized nanomagnetic core, a modifiable shell and bio-molecules immobilized on the surface of the NPs. As mentioned in the previous section, these inert coatings or shells in addition to providing protection against chemical degradation of magnetic cores prevent the release of potentially toxic components. Furthermore, functionalization chemistries are better established with these materials than those comprising of bare MNPs. Among the various core-shell designs, silica shells are the most attractive options to serve as protective coatings on MNPs due to their stability under aqueous conditions and ease of synthesis. An extensive literature survey shows that sol–gel processes, using tetraethoxysilane (TEOS) are generally employed to produce coatings of controlled thickness [37-38]. The use of functional alkoxysilanes, such as 3-aminopropyltriethyoxysilane (APS), allows for surface reactive groups to be easily added to these core–shell structures. Multifunctional core–shell MNPs, comprising of 10 nm iron oxide cores, surrounded by a 10–15 nm thick SiO_2 shells have been reported. An organic dye viz. tris (2, 2′-bipyridine) ruthenium, was doped inside a second silica shell to provide luminescence and prevent quenching by interaction with the magnetic core. Such core–shell structures, exhibiting simultaneous superparamagnetism and luminescent properties show considerable promise in biomedical imaging applications [39]. Gold offers several advantages as a coating material for MNPs due to its low chemical reactivity and unique ability to form self-assembled monolayers (SAM) on their surface using alkanethiols. Plasmonic property of gold, combined with the superparamagnetism of magnetite or maghemite nanoparticles are currently being exploited for numerous biomedical and bio-sensing applications. In a recent investigation, epidermal growth factor receptor antibody (EGFRA) has been conjugated to dumbbell-shaped Au-Fe_3O_4 nanoparticles through polyethylene glycol (PEG, M_r=3000) and dopamine and used as magnetic and optical probes for imaging EGFR over-expressing A431 cells [40]. In another example, the same authors have demonstrated the feasibility of Herceptin conjugated, dumbbell-like Au−Fe_3O_4 nanostructures to serve as a multifunctional platform for target-specific delivery of cis-platin into Her2-positive breast cancer cells (Sk-Br3) with strong therapeutic effects [41].

1.7.3.5 Small Molecules or Coupling Agents

Although polymeric modifications as well as core-shell designs prevent aggregation problem and improves bio-compatibility, the large overall size of such systems may significantly limit their tissue distribution, penetration, intravenous delivery, and metabolic clearance. This is further accompanied by significant loss in magnetic response (~40-50%) of the core magnetic material, which negatively influences the magnetic targeting ability of the carrier system *in vivo* [42]. An alternative approach involves the chemical modification of the magnetic nanoparticles surface with small intermediary molecules or coupling agents that ensure availability of complementary attachment to functional bio-molecules, in addition to sol stabilization. Although there are lots of inconveniences in applications, organosilanes are by far the most widely used reagents, chosen for metal oxide functionalization. Silanes are bifunctional molecules with the general chemical formula Y-$(CH2)_n$-Si-R_3, where Y represents the headgroup functionality, $(CH_2)_n$ an alkane chain, and Si-R_3 the anchor group by which the silane will be grafted to the metal oxide surface (with R being Cl or OR). The major drawback in the functionalization with organosilanes is homocondensation in the presence of traces of water, which may lead to multilayer or even gel formation instead of condensation with the surface [43]. Although much less widespread, organophosphorous compounds offer a promising alternative in some the coupling of organic components to metal oxides [44]. The use of bifunctional phosphonic acid based surface coupling agents [R-(CH_2) n PO_3H] where [R = -COOH, -OH, -NH_2] not only render the nanoparticles hydrophilic and stable with respect to aggregation but also imparts functionality on the surface for facile access to bio-conjugates. In the present dissertation, phosphonic acid coupling agents have been extensively used for the introduction of amine or carboxyl functionalized phosphonate monolayer on the surface of iron-oxide nanoparticles. These amine or carboxyl groups are readily interchangeable with a wide variety of reactive functional groups, thus allowing easy manipulation of the surface and covalent modification with functional ligands.

1.8 Chemistry of surface modification

A host of chemical approaches are available for the integration of targeting, therapeutic, and imaging reporter molecules on the surface of nanoparticles, which can be subdivided into **(i)** conventional bio-conjugation strategies in which functional groups at the nanoparticle

surfaces are either directly bonded to reactive ligands or a linkage reaction is facilitated with the aid of catalyst and **(ii)** click chemistry. Irrespective of the conjugation strategy chosen, the primary goal is to conjugate the targeting, imaging, or therapeutic moiety without compromising its functionality once attached. In the following section, the unique features of the respective strategies have been highlighted with example application of each in bio-conjugation.

1.8.1. Conventional bio-conjugation strategies

The surface of MNPs may be tailored with diverse functionalities based on the nature and chemical composition of the coating material and the reactive groups present on the targeting ligand. Since amines or carboxylic acids are the most common functional targets in bio-molecules, either of these two functionalities should be present on the nanoparticle surface to allow further derivatization with biological ligands. These groups are readily interchangeable. Reaction of amine-functionalized NPs with succinic anhydride or glutaric anhydride, converts the surface to carboxylates, whereas the activation of carboxylic acid functionalized particles with *N*-hydroxysuccinimide (NHS) or *N*-hydroxysulfosuccinimide (sulfo-NHS) and 1-ethyl-3-(dimethylaminopropyl) carbodiimide (EDC) and subsequent reaction with a diamine results in amine-functionalized nanoparticles. Amine-coated nanoparticles are easily modified by ligands containing NHS-modified carboxylic acids or isothiocyanates, such as fluorescein isothiocyanate (FITC) (**Fig. 2.4**).

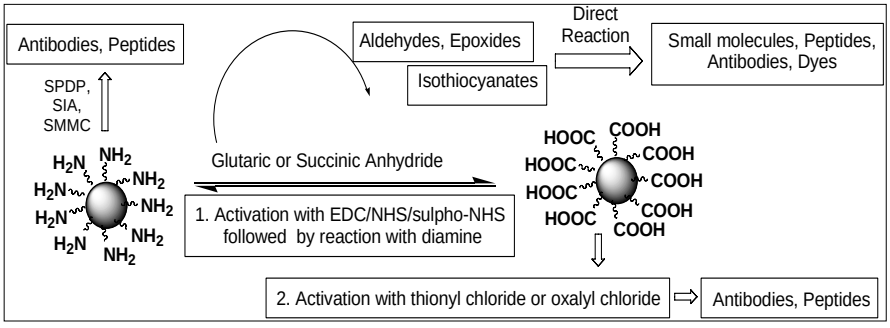

Fig. 1.5: A schematic representation, elaborating the conventional bio-conjugation strategies.

Epoxides and anhydrides can also be directly reacted in sodium bicarbonate buffer at pH 8.6 [45]. Functionalization of these particles with carboxylic acid containing ligands ideally occurs in the presence of activating agents such as EDC and NHS or sulfo-NHS. Ligands bearing sulfhydryl groups can also be immobilized onto the surface of amine-coated particles after modification with heterobifunctional linkers such as succinimidyl iodoacetate (SIA),

succinimidyl-4-(*N*-maleimidomethyl)cyclohexane-1-carboxylate (SMCC) or *N*-succinimidyl-3-(2-pyridyldithio)propionate (SPDP). One of the main advantages of utilizing SPDP is that it allows simultaneous quantification of the number of reactive amine groups on the nanoparticle surface. Pyridine-2-thione is released upon reaction of surface amine groups with dithiothreitol (DTT), enabling its spectrophotometric determination. In comparison to amine-coated nanoparticles, which are readily conjugated to a number of reactive ligands, carboxylic acid-coated particles require activation prior to conjugation. Amine containing ligands are typically conjugated to carboxylic acid functionalized particles in the presence of EDC and sulfo-NHS to yield the corresponding amide. Ligands containing hydroxyl groups can also be reacted with carboxylic acid coated particles via esterification. For this purpose, the particles are initially precipitated from aqueous solution by addition of acetone, and then washed thrice with acetone to remove the residual water. These dried particles are then suspended in anhydrous dimethyl-sulfoxide (DMSO), followed by the addition of thionyl or oxalyl chloride in order to form the corresponding acid chloride. Once the activation has been accomplished, a drop of water is added to the solution to quench the remaining thionyl chloride, followed by addition of an excess of the alcohol and a base catalyst. Alternatively, the EDC-NHS activation method can be employed. In all cases, purification of the functionalized MNP s is facilitated by magnetic concentration, followed by repeated washing with deionized water. Throughout the course of entire dissertation, these simple chemical approaches have been successfully utilized to synthesize tailored MNPs with a variety of reactive functional groups.

1.8.2 Click Chemistry

The selectivity of a bio-conjugation process can be considerably improved by attaching a ligand to the nanoparticle, where the ligand includes a functional portion that is capable of forming an irreversible bond with an object at a site, complementary and chemoselective to the functional portion. The "click chemistry" concept, introduced by Dr. Barry Sharpless in 1999 refers to a group of reactions that are fast, environment-friendly, simple to use, easy to purify, versatile, regiospecific, and give high product yields. While there are a number of reactions that fulfill the aforementioned criteria, the Cu (I) catalyzed Hüisgen 1, 3-dipolar cycloaddition between terminal alkynes and azides (**Fig. 1.6**), also known as the CuAAc reaction has been proved to be highly beneficial in the functionalization of MNPs, especially, when a chemoselective conjugation is desired. The reaction is irreversible and the resulting linkage is very stable owing to the formation of a triazole ring. The method provides an

effective means for introducing various organic functional groups to substrates in solution under mild conditions with a great functionality tolerance.

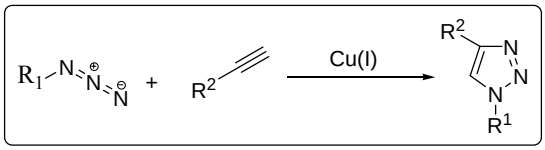

Fig. 1.6: The Cu (I) catalyzed Huisgen 1, 3-dipolar Cycloaddition of Terminal Alkynes and Azides

The robustness of the "click" technique has been demonstrated with CLIO [46]. CLIO can be functionalized with azide or alkyne moieties by reaction of carboxylic acid-functionalized nanoparticles with azido propylamine or propargylamine using the standard carbodiimide method. As proof-of-principle, several biologically relevant molecules such as the succinimidyl esters of biotin or VivoTag-S 680 (a near infrared fluorophore), or the isothiocyanate of fluorescein, were directly reacted with azido propylamine or propargylamine, while ligands containing hydroxyl groups, such as estradiol, paclitaxel, and Disperse Red 1, were first activated with 1,1′-carbonyldiimidazole (CDI), followed by reaction with the alkynyl or azido amine. Conjugation reactions between the functionalized nanoparticles and ligands occurred in aqueous solution at 37 °C for 5–8 hours, resulting in greater than 90% conversion. Although application of click chemistry to MNPs is still in an age of infancy, some recent reports have explored the possibility to exploit click chemistry for chemoselective synthesis of multifunctional, MNP based platforms. For example, chemoselective synthesis of folic acid (FA) decorated magnetite (Fe_3O_4) nanoparticles (NPs) via click reaction between azide-functionalized Fe_3O_4-NPs and alkyne bound folate has been reported by Hayashi et al for application in cancer hyperthermia [47]. In another example, azide-alkyne click chemistry has been successfully used for specifically linking the cyclic tumor-targeting peptide LyP-1(CGNKRTRGC) to polymer-coated magnetofluorescent nanoparticles [48].

LyP-1 binds to p32, a mitochondrial protein that is both overexpressed and aberrantly localized at the cell surface of tumor cells, macrophages and lymphatic endothelial cells in certain experimental tumors and human cancers. Such LyP-1 clicked nanoparticles can stably traverse the systemic circulation, extravasate into tumors and penetrate the tumor interstitium to specifically bind to receptors on p32-expressing cells in the tumors (**Fig. 1.7),** which provides a strong motivation for future use of "click" functionalization as a strategy for developing theragnostic nanoparticles for application in vivo. Some recent studies have

successfully exploited the "click" strategy to design and synthesize biocompatible, multimodal, theragnostic iron-oxide nanoformulation [49] for concurrent cancer diagnosis and therapy. The positive attributes of the in-vitro results make these functional nanoparticles a promising platform for further in-vivo evaluation. In the present dissertation, **Chapter 4** has been exclusively dedicated to the chemoselective synthesis of a multifunctional, theragnostic nanoplatform for combined cancer-targeted therapy and multimodal imaging, combining a unique collage of classical bio-conjugation strategies with surface diazo transfer and "click chemistry.

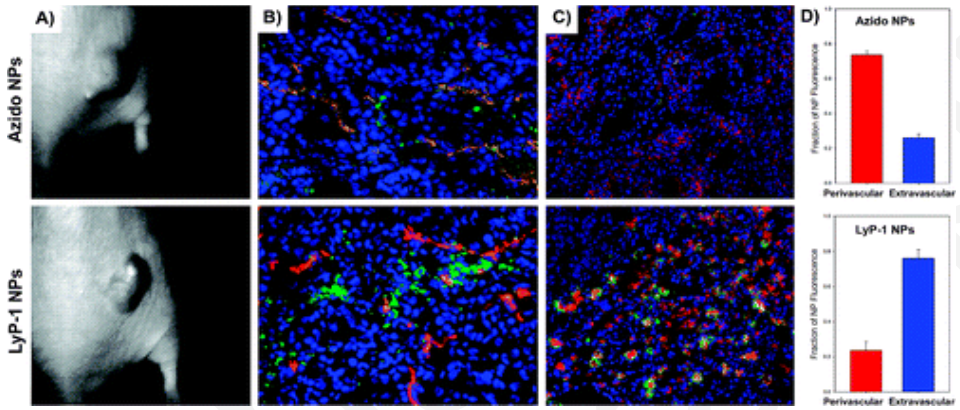

Fig. 1.7: "Click" LyP-1-nanoparticle targeting to tumor cells *in vivo,* adopted from [48]. Nanoparticles bearing only azide groups (top) or labeled with LyP-1 peptides (bottom) that are matched in circulation time were injected intravenously via the tail vein into mice bearing human MDA-MB-435 cancer xenografts. Histological sections were obtained 24 h postinjection. **(A)** Light reflectance images of mice bearing the tumor xenografts. **(B)** Fluorescent LyP-1-nanoparticles (VT680 fluorescence pseudocolored as green) did not colocalize with CD31, a blood vessel marker (red), while untargeted azide-PEG nanoparticles remained localized to the blood vessels or their immediate periphery. **(C)** LyP-1-nanoparticles (green) accumulated in regions of high p32 expression (red), whereas untargeted, azido-bearing nanoparticles did not accumulate in these areas. **(D)** Histological quantitation using CD31 stain to assess nanoparticle localization to immediate periphery of blood vessels. The fraction of LyP-1 nanoparticles outside of the perivascular space of CD31-stained blood vessels is significantly higher than azido-nanoparticles ($P < 0.005$) as assessed from three randomly chosen views in each set of mice (n=3). Together, LyP-1-coated nanoparticles penetrate into the tumor interstitium to target p32-expressing cells.

1.9 Clinically approved iron-oxide based contrast agents

SPIO/ USPIOs have been examined extensively as MRI contrast agents to improve the detection, diagnosis, and therapeutic management of solid tumors. Some recent advancements include clinical imaging of liver tumors and metastases through RES-mediated uptake of SPIOs. USPIO s can further shown to be effective in the identification of lymph node metastases with a diameter of 5–10 mm under MRI. This non-invasive approach has broad

implications, as identification of lymphatic dissemination is an essential component of staging and determining the approaches to treatment of diseases such as prostate, breast, and colon cancers. In the last few years, a number of SPIO/USPIO based contrast agents have been approved by FDA and commercialized, the characteristic features of which have been detailed in **Table 1.1**.

Almost all the formulations listed in **Table 1.1** viz. **AMI-25**, **SHU 555A** or **AMI-227** comprises of a SPIO or USPIO core, surrounded by a dextran/ carbo-dextran corona with the exception of **AMI-121**, which is a representative silica coated, iron-oxide contrast agent. Although silica coated MNP s are reasonably stable in aqueous media, they tend to aggregate in blood, and, therefore are inadequate for blood injection. In view of their excellent colloidal stability, even under harsh physiological conditions, dextran coated nanoparticles are superior to the silica based MNPs for MR imaging applications. Smaller dextran coated iron-oxide nanoparticles including MION and its derivative CLIO have relatively smaller hydrodynamic sizes with considerably long half-life and their surface can be readily linked with biologically relevant molecules, which make them promising candidates for *in vivo* molecular MRI of biological targets. Several other MNP based contrast agents such as magnetoliposomes, protein coated magnetoferritin magnetodendrimers and mixed metal-oxides, based on nano-ferrites or manganatites are currently under active investigation. Further studies are yet to be completed before these formulations can be successfully implemented into clinics.

Table 1.1: Non-exhaustive list of clinically approved, iron-oxide based MR contrast agents*

MR contrast agent	Corona	PCS size (nm)	T_2 relaxivity $(mMs)^{-1}$	Blood half life	Target
AMI-25 [a, b] [50 (a-b)]	Dextran	58	107 (0.47 T)	~ 6 min	MPS (Liver)
SHU-555A[a, c] [51]	Carbo-Dextran	62	188 (0.94 T)	3 min	MPS organs
AMI-227 [a, d] [50]	Dextran	17-20	53 (0.47 T)	> 24 h	Lymph nodes
AMI-121. [a, e, f] [52]	Silica	300	72 (0.47 T)	< 5 min	Abdomen
USPIO MION-46L [53]	Dextran	18-24	35 (0.47 T)	~ 10 h	MPS organs
Magnetoliposomes [54]	PEG	40	240 (1.5T)	~53.2 min	Bone marrow

* Relaxivities were measured at 37° C except for magnetoferritin, which was measured at 25° C. The static magnetic field B_0, expressed in Tesla is provided in the brackets. [a] Commercialized; [b] Endorem® from Guerbet and Feridex IV® from Berlex Lab [c] ; Resovist® from Schering; [d] Combidex® from Advanced Magnetics and Sinerem® from Guerbet; [e] Lumirern® from Guerbet and Gastromark ® from Advanced Magnetics; [f] AMI-121 is delivered orally.

1.10 Targeting MNPs to cancer cells

A promising approach for targeted cancer therapy relies on the ability of therapeutic agents to selectively accumulate in the pathological site of interest following intravenous administration. This could be done by means of *physical* targeting, *passive targeting* or *active* targeting.

1.10.1 Physical targeting

Physical targeting can be achieved *via* the guidance of superparamagnetic nanoparticles through an external magnetic field. Site-specific delivery of chemotherapeutic agents can be significantly improved by magnetic drug targeting (MDT).

The process in general involves**:**

- The attachment of a cytotoxic drug to a biocompatible MNP carrier
- Intravenous injection of these MTCs in the form of a colloidal suspension.
- Application of a magnetic field gradient to direct the MTC to the pathological site.
- Release of the therapeutic agent from the MTC.

Although seemingly straightforward, the effectiveness of this method depends upon a number of parameters ranging from the physicochemical properties of the drug-loaded MNPs, magnetic field strength and geometry to depth of the target tissue, rate of blood flow, and vascular supply. Early clinical trials of colloidal iron oxide MTCs, loaded with epirubicin and directed toward solid tumors have demonstrated successful accumulation in the target site in about half the patients in this study [55]. A few years later, Alexiou et al. demonstrated the successful *in vivo* delivery of MCT composed of starch coated USPIO loaded with mitoxantrone into VX2-squamous cell carcinomas on the hind limbs of New Zealand White Rabbits [56]. The group demonstrated the effectiveness of these MCTs to completely eradicate tumors approximately after 35 days of treatment. Although these MTC s were well-tolerated *in vivo,* several problems were identified with this technique, which included the possibility of memorization of the blood vessels, difficulty in scaling up from animal models due to limited field penetration of commercial magnets, control of drug diffusion after release from the MTC, and toxic responses to the MTCs. To address some of these issues and develop a

theoretical basis for the technique, Grief and Richardson [57] created a mathematical model adding in the effects of hydrodynamics within blood vessels, particle volumes, magnetic field strength, and even the effects of cells within the plasma. In this study the authors concluded that MDT could only be used effectively for targets close to the surface of the body.

1.10.2 Passive targeting

Nanoparticle systems exploit the characteristics of tumor growth for the use of a passive form of targeting [58]. Tumor becomes diffusion-limited at a volume of 2 mm^3 or above. This diffusion limitation impacts nutrition intake, waste excretion, and oxygen delivery to a considerable extent. Diffusion limitations of tumors can be overcome by increasing the surrounding vasculature in an event called angiogenesis, characterized by aberrant tortuosity and abnormalities in the basement membrane and the lack of pericytes lining endothelial cells [59]. The incomplete tumor vasculature results in leaky vessels and based on the type or nature of the tumor presents gap sizes of 100 nm to 2 μm. In addition, interstitial pressure is higher at the center of tumors than at the peripheral regions since tumors lack a well-defined lymphatic system. The increased internal pressure leads to an outward convective interstitial fluid flow, which decreases drug diffusion to the center of the tumor. However, drugs and nanoparticles that gain access to the tumor interstitium have higher retention times, as compared to normal tissues. The combination of leaky vasculature and poor lymphatic drainage results in what is known as the **Enhanced Permeability and Retention (EPR)** effect.

Passive extravasation through the leaky tumor vasculature is the primary mechanism by which nanoparticle vectors gain access to tumor interstitium. Size is a critical issue, which dictates the fate of MNPs *in vivo*. The overall size of MNPs must be sufficiently small to avoid rapid splenic filtration but large enough to evade renal clearance. Nanoparticles larger than 200 nm are sequestered by phagocytotic cells of the spleen, while particles smaller than 5.5 nm are rapidly removed through renal clearance [60]. Particles escaping filtration are subject to opsonization resulting in recognition and clearance by Kupffer cells and other tissue macrophages. As described in the previous sections, various coatings including hydrophilic polymers, inorganic matrices and small molecules have been utilized to create a non-fouling coating on the particle surface

Passive targeting can also occur through the inherent clearance by the RES whereby phagocytosis by blood monocytes and tissue macrophages of MNPs provides a means of

delivering contrast agents and drug carriers to related organs. This RES-mediated targeting is the basis for the first clinical application of MNPs in the form of Ferumoxides AMI-25 (Endorem® and Feridex IV®) for liver imaging [61]. The rapid uptake of these MNPs by Kupffer cells of healthy hepatic parenchyma allows for their differentiation from diseased tissue by the contrast enhancement observed under MRI [62].

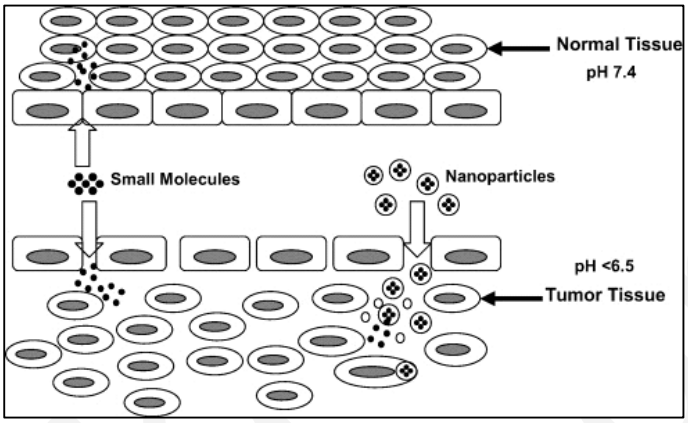

Fig. 1.8 Schematic illustration for passive targeting using the **E**nhanced **P**ermeability and **R**etention (EPR) effect.

Passive targeting also involves the use of other innate characteristics of the nanoparticle which can induce targeting to the tumor, such as charge. In general, positively charged non-targeted MNPs bind to cells through electrostatic interaction with the negatively charged cell membranes and are then internalized by cells. On the other hand, endocytosis of negatively surface-charged MNPs may occur through both protein-mediated phagocytosis and diffusion. A change in surface charge of MNPs can be induced by covalently coupling different chemical materials such as amino, PEG and carboxyl groups. As for example, surface modification of magnetite nanoparticles with aminosilanes (magnetic core diameter 10 nm, hydrodynamic diameter 30 nm) afford numerous positively charged surface groups under physiological conditions. Cellular uptake of these aminated-magnetite nanoparticles in glioblastoma cells was 500–2000 times as large as in normal cells [63]. Similarly, anionic nanoparticles have also found applications in cellular MR imaging, in particular, for *in-vivo* tracking of T-lymphocytes with direct implications in cell-based anticancer therapy [64].

Although long-circulating nanocarriers significantly increase the tumor localization of the payload, the strategy is not free from limitations [65]. First, the targeting effect is highly

dependent on the degree of tumor vascularization and angiogenesis. Passive targeting effect may not be always achieved in all tumors as the porosity and pore size of tumor vessels vary with the type and status of the tumors [66]. Secondly, the elevated interstitial fluid pressure, a common condition prevailing in most of the solid tumors inhibits efficient uptake and homogeneous distribution of MNPs and/or drugs in the tumor tissues. In addition, the passive targeting can be further limited due to the very presence of polymeric coatings on the surface of the nanoparticles. Such a polymer-capped surface not only prevents the interaction between the nanocarriers and opsonins but also that between the nanocarriers and cell surface. As for instance, PEGylated liposomal doxorubicin was less efficient in entering the tumor cells, with a much lower AUC_{tumor}/AUC_{plasma} (0.31) (AUC: area under the curve) compared to that of non-PEGylated liposomes (0.87) [67]. The reduced interactions inhibit effective uptake of the payload by the tumor cells. In order to circumvent these problems, targeting molecules such as antibodies, peptides, nucleic acids and other molecules that bind directly to a receptor overexpressed on a tumor-cell surface are conjugated to the surface of nanocarriers (**Fig. 1. 8).** This strategy, known as active targeting strategy was first proposed by Paul Ehrlich in the 19^{th} century, even before a rational targeting ligand was discovered. Ehrlich coined the term "magic bullet" to describe an idealized package that would target and deliver drugs to a specific place in the body, thereby reducing the systematic side effects, associated with nonspecific targeting and bio-distribution associated with the chemotherapeutic drug [68]. This idea translates directly to the ongoing effort in cancer research to develop a targeted therapy, in which increased efficacy and decreased toxicity are the motivating factors.

1.10.3. Active Targeting

It is well known that, cancer cells, unlike normal cells are rapidly proliferating. One mechanism underlying this growth is the over-expression of receptors that allows the uptake of growth factors *via* receptor-mediated endocytosis more efficiently than normal cells. This could be use as a *"Trojan horse"* to deliver anticancer agents, decorating the surface of nanoparticles with antibodies or ligands that specifically binds to these receptors (**Table 1. 2**). The current section will review some specific examples on active targeting of MNPs with special emphasis on cancer diagnosis and imaging.

1.10.3.1. Antibodies as targeting agents

Monoclonal antibodies (mAbs) were the first targeting agents to exploit molecular recognition for delivering MNPs to their target pathological zone and continue to be used because of their

high specificity [69-71]. Recently, the development of Herceptin™, an FDA-approved mAb to the HER2/neu (erbB2) receptor, has made it a popular targeting agent for nanoparticles [72]. Multifunctional magnetic nanocrystals, coupled with Herceptin™ have been found to be effective for the *in-vivo* MR diagnosis of cancer in mice xenograft model [73]. Further conjugation of these nanocrystal probes with fluorescent dye-labeled antibodies enables both *in vitro* and *ex vivo* optical detection of cancer as well as *in vivo* MRI, which are potentially applicable for an advanced multimodal detection system. Very recently, Kou *et al.* [74] have developed a targeted contrast agent (SM-USPIO) by conjugating coprecipitated USPIO to a humanized SM5-1 antibody which can specifically react with human hepatocellular carcinoma (HCC) cells. These SM-USPIO nanoparticles were demonstrated to be able to selectively accumulate in the tumor cells resulting in a marked decrease of MRI T_2-weighted signal intensity (**Fig. 1.9**). Bio-distribution studies demonstrated the efficient accumulation of SM-USPIO in the ch-hep-3 tumor in nude mice. MRI studies indicated that SM-USPIO had the potential to be a promising targeted contrast agent for diagnosis of HCC.

Another interesting example of these antibody conjugated nanomagnetic probes is provided by the recently developed epidermal growth factor receptor (EGFR) targeted nanoparticles. This nanoprobe is synthesized by conjugating a single-chain anti-EGFR antibody (ScFvEGFR) to surface functionalized quantum dots (QDs) or magnetic iron oxide (IO) nanoparticles, which specifically bind to and are internalized by EGFR-expressing cancer cells, thereby producing a fluorescent signal or magnetic resonance imaging (MRI) contrast into an orthotopic pancreatic cancer model [75].

Despite their wide-spread applicability, one drawback of mAbs is their large size and inherent immunogenicity, which can cause conjugated nanoparticles to diffuse poorly through biological barriers [76]. This however instigates the researchers to explore the efficacy of other affinity ligands based on short peptides or small molecules for cancer-specific targeting.

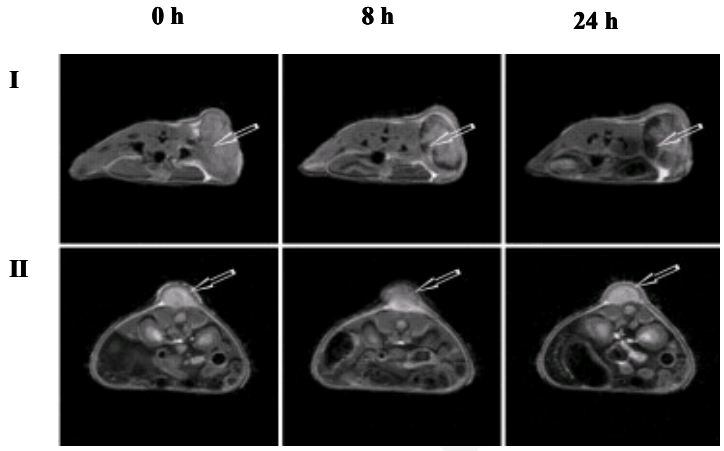

Fig. 1.9 T_2-weighted axial spin-echo images through the abdomen and lower flank of nude mice bearing ch-hep-3 tumor, adopted from [74]. Images are taken at various times (0, 8 and 72 h) after the administration of SM-USPIO (I) or H-USPIO (II) via tail vein. The arrows indicate the tumor area. (H-USPIO denotes the control rhuMAbHER2 conjugated USPIO)

1.10.3.2 Aptamers as targeting agents

Another important class of affinity ligands is the aptamers which contend antibodies in their diagnostic potential. Aptamers are oligonucleotides derived from an *in vitro* evolution process called SELEX (**S**ystematic **E**volution of **L**igands by **EX**ponential Enrichment). Highly specific DNA aptamers are selected by SELEX to bind with specific molecular or cellular targets. Aptamers are able to fold into unique three-dimensional conformations with distinct biomolecular binding properties and have successfully been used for protein detection by sensor array and affinity capillary electrophoresis and targeted therapeutic applications. Biodegradable, nanoparticle-aptamer based method has now emerged as a promising strategy towards cancer-specific targeting. Although further optimization is necessary for application in clinical diagnostics, aptamer conjugated magnetofluorescent nanoparticles have shown considerable promise in the specific recognition of CCRF-CEM acute leukemia cells from complex mixtures, including whole blood samples [77]. The use of aptamer targeted nanoparticles for the collection and detection of multiple cancer cells have been further extended by Smith et al [78].

1.10.3.3 Peptides as targeting agents

In the last few years, significant research has focused on targeting MNPs to cancerous cells using tumor-homing peptides. Some representative examples are discussed below.

- **Targeting angiogenesis pathway of tumors:** Targeting of MNPs to receptors overexpressed on tumor neovasculature has currently become an extensive area of research. The formation of new blood vessels, or angiogenesis, is an essential component of tumor growth and has been shown to be highly specific for neoplasia [79]. A relatively large number of angiogenesis markers, which include the αvβ3 integrin, vascular endothelial growth factor (VEGF), cell surface nucleolin, and heparin sulfates, have been identified as potential targets for the delivery of diagnostic and therapeutic agents [80-81]. Targeting agents, such as the Arg-Gly-Asp (RGD) peptide demonstrating high affinity for the αvβ3 integrin, have been evaluated for the delivery of MNPs to a variety of neoplastic tissues including breast tumors, malignant melanomas, and squamous cell carcinomas [82-84]. In a recent study, a vascular homing peptide, F3, which binds to nucleolin expressed on tumor endothelium and cancer cells, was utilized to deliver a multifunctional MNP to brain tumors [85]. Through combination of photodynamic therapy (PDT) with MR contrast property of the MNP component, this group was able to monitor the treatment efficacy of 9L gliomas in rats. Ultrasmall c(RGDyK) peptide-coated magnetite nanoparticles with average hydrodynamic diameter < 10 nm have demonstrated their potential applicability as contrast agents for *in vivo* tumor detection through MRI [86]. When administrated intravenously, these nanoparticles accumulate preferentially in the integrin $\alpha_v\beta_3$-rich tumor area, which are readily tracked by MRI. In another example, the tumor-homing peptide CREKA (Cys-Arg-Glu-Lys-Ala), capable of forming distinct meshwork in the tumor stroma has been synthesized and explored for cancer-specific targeting [87]. Specific accumulation of CREKA-conjugated nanoparticles in both tumor vessels and stroma led to intravascular clotting in tumor blood vessels, which attracted more nanoparticles into the tumor, amplifying the targeting and sensitivity of detection through combined MR/ optical based imaging techniques.

- **MMP-2 targeted MNPs:** Chlorotoxin (CTX), a peptide originally purified from the venom of the *Leiurus quinquestriatus* scorpion, has also been shown to be an

effective targeting agent for tumors of neuroectodermal origin. Studies suggest that the target of CTX is associated with the membrane-bound matrix metalloproteinase-2 (MMP-2) protein complex, which is up-regulated on gliomas, as well as a variety of other tumors. CTX has been shown to facilitate targeted delivery of MNPs to brain tumor cells. In course of their investigation Veish *et al.* constructed a multimodal nanoprobe composed of poly (ethylene glycol) (PEG) coated iron oxide nanoparticle that is capable of specifically targeting glioma tumors via the surface-bound targeting peptide, chlorotoxin (CTX) [88]. Preferential accumulation of the nanoprobe within gliomas and subsequent magnetic resonance imaging (MRI) contrast enhancement were demonstrated *in vitro* in 9L cells and *in vivo* in tumors of a xenograft mouse model. High targeting specificity and benign biological response corroborated to the successful utilization of this nanoprobe as a potential platform for diagnosis and treatment of gliomas and other tumors of neuroectodermal origin.

- **Bombesin targeted MNPs:** Another important target is constituted by the bombesin (BN) receptors, present on normal acinar cells of the pancreas. A specific example can be cited in which the BN targeted CLIO nanoparticles, labeled with a NIR dye Cy5.5 has been found to accumulate in the mouse pancreas in receptor dependant fashion, which was however absent in other tissues, as detected by the tissue fluorescence measurements. The use of BN-CLIO (Cy5.5) nanoparticle as a normal tissue-targeted, T_2-reducing contrast agent offers a promising approach towards imaging pancreatic ductal adenocarcinoma (PDAC) [89].

- **Hepsin targeted MNPs:** Hepsin (HPN) is a type II transmembrane serine protease that is expressed in precursor lesions, high-grade prostate intra-epithelial neoplasia, and in hormonerefractory metastatic tumors. Its cell surface expression and malignant cell localization make it an ideal candidate for the development of prostate cancer-targeted imaging agents [90]. Phage screening against PC3 cells, stably transfected to over-express HPN (HPN-PC3) was able to identify a consensus binding sequence, IPLVVPL (IPL-F). Fluorescein-labeled-IPL-F conjugated CLIO nanoparticles have shown their specific binding affinity towards HPN-expressing LNCaP xenografts in mice model, which however testifies to their potential utility for *in vivo* detection of prostate cancer through combined optical/MR-based imaging.

- **E-selectin targeted MNPs:** E-selectin, also known as CD62E is a cell adhesion molecule expressed only on endothelial cells activated by cytokines. Fluorescent peptide-magnetic nanoparticle conjugates have demonstrated their potential utility for imaging the E-selectin expression in mouse xenograft models of Lewis lung carcinoma (LLC) via fluorescence reflectance imaging [91]. The conjugate, synthesized by covalent conjugation of the E-selectin-binding peptide (ESBP; CDSDSDITWDQLWDLMK) to the surface of CLIO (Cy5.5) MNPs showed rapid E-selectin mediated rapid internalization of the as-synthesized nanoparticles by activated human umbilical vein endothelial cells (HUVECs)

- **uMUC-1 targeted MNPs:** Underglycosylated mucin-1 antigen (uMUC-1) is an early tumor marker, ubiquitously expressed on almost all human epithelial cell adenocarcinomas, making it an accessible target for binding and imaging. EPPT1 peptide shows specific binding affinity towards uMUC-1 and has been used by various groups to target tumor cells over-expressing uMUC-1 on their surface [92-93]. EPPT-1 has been conjugated to the dextran coat of CLIO to generate a multimodal MR/ optical imaging probe, which led to significant T_2 signal reduction of certain regions of uMUC-1-positive LS174T tumors within 24 hours of nanoparticle injection while no significant change was seen in uMUC-1-negative U87 tumors. These results were re-validated by near-infrared fluorescence (NIRF) imaging, in which NIRF Cy5.5 dye-labeled CLIO nanoparticles were used both as MR- and NIRF-imaging contrast agent. This unique imaging probe produced a high-resolution signal on MR images and real-time NIRF imaging data, providing comprehensive information on tumor localization, environment, and status.

- **LHRH conjugated MNPs:** Binding sites for luteinizing hormone-releasing hormone (LHRH, a decapeptide with the primary sequence of EHWSYGLRPG) is found on 52 % of human breast cancers [94], about 80 % of human ovarian and endometrial cancers and 86 % of human prostatic carcinoma specimens. As LHRH receptors are not expressed on most normal tissues, they represent a specific target for cancer chemotherapy with antineoplastic agents linked to an LHRH vector molecule. LHRH-conjugated SPIO nanoparticles have been successfully employed for the *in-vivo* detection and MR imaging of a wide variety of tumors including metastatic lung

and breast cancer cells with high sensitivity and precision [95]. As indicated by transmission electron microscopic (TEM) studies, LHRH-SPIO nanoparticles accumulate in the cytosol and the nucleus in the breast cancer cells. Because of their unique capacity to escape from the endosome, LHRH-SPIO have promising implications in future drug-delivery for the detection of metastases and disseminated cells in lymph nodes, bones and peripheral organs, since it seems these unique targeted MNPs could escape from the endosome.

- **uPAR targeted MNPs:** The urokinase plasminogen activator (uPA) system consists of the serine protease uPA, its glycolipid-anchored receptor, uPAR and its 2 serpin inhibitors, plasminogen activator inhibitor-1 (PAI-1) and plasminogen activator inhibitor-2 (PAI-2). Recent findings suggest that the uPA system is causally involved at multiple steps in cancer progression, which makes it an excellent surface molecule for receptor-targeted imaging of pancreatic cancer using multifunctional nanoparticles. In a very recent report Yang *et al.* has reported a uPAR-targeted dual-modality molecular imaging nanoparticle probe, prepared by conjugating a near-infrared dye-labeled amino-terminal fragment of the receptor binding domain of urokinase plasminogen activator to the surface of functionalized magnetic iron oxide nanoparticles. Systemic delivery of uPAR-targeted nanoparticles leads to their selective accumulation within tumors of orthotopically xenografted human pancreatic cancer. The dual imaging capability of the nanoparticles facilitate *in vivo* optical and magnetic resonance imaging of uPAR-elevated pancreatic cancer lesions [96].

1.10.3.5 Small molecules as targeting agents

Functionalization of MNPs with small molecules as targeting ligands has recently been described as an alternative targeting strategy, with potential for major biomedical advances. In this particular context folate-receptor (FR) mediated targeting of MNPs (**Fig. 1.11**) have roused meticulous interest because: **(i)** FR is upregulated in many human cancers, including malignancies of the ovary, brain, kidney, breast, myeloid cells and lung [97-98] **(ii)** access to the folate receptor in those normal tissues that express it can be severely limited due to its location on the apical membrane of polarized epithelia; **(iii)** folate receptor density increases as the stage/grade of the cancer worsens; and **(iv)** the high affinity of the folate for its cell surface receptor (K_d about 10^{-10}) appears attractive [99]. In addition to all these, folic acid is nonimmunogenic, highly stable, inexpensive and has low molecular weight, which facilitates

the easy internalization of nanoparticle-folate conjugates through cell membrane. Therefore, the development of an efficient magnetic nanoparticle–folic acid conjugate system is a current challenge in this area of research.

Several attempts have been made to develop biodegradable hydrophilic magnetic nanoparticle–folate conjugate delivery systems using dextran, poly-(D, L-lactic-*co*-glycolic acid) (PLGA), poly-(ethylene glycol) (PEG), (poly-L-Lysine) (PLL) and their block copolymers [100-102]. Although these delivery systems improve biocompatibility, resist protein adsorption, and increase the circulation time and internalization efficiency, the large size of these macromolecule-based systems does not facilitate intravenous delivery. So an effective design of the nanoparticle–folate-conjugate system must take into account its size and colloidal stability in the physiological environment which promises the easy perfusion of the nanoparticle system out of the blood stream to reach the target cell of interest.

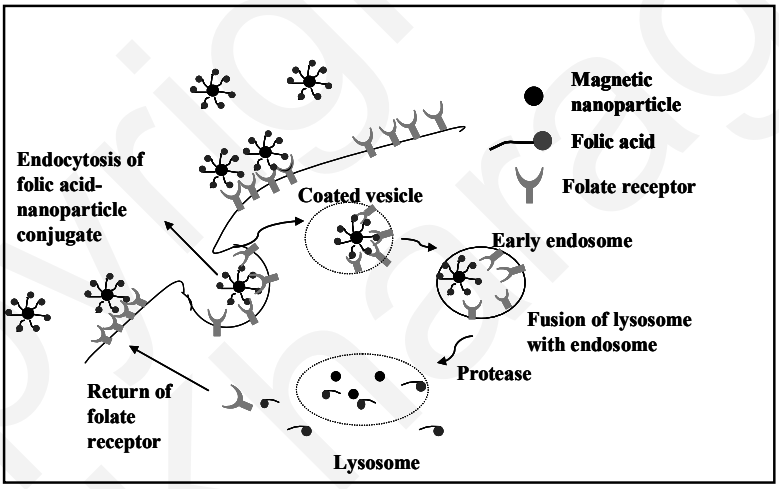

Fig. 1.10: Folate-receptor mediated internalization of magnetic nanoparticles in cancer cells

Very limited, recent reports have investigated on such non-polymer based MNP designs. In a recent report, Kohler et al. have demonstrated the sustained release of methotrexate (MTX) in folate-receptor over-expressing cancer cells using a non-polymer based iron-oxide nano-formulation [103]. In this study, the authors covalently attached MTX to 3-aminopropyl trimethoxy-silane (APTS) grafted magnetite nanoparticles through amidation between the γ-carboxyl groups of MTX and surface-pendant amino groups. Through the use of covalent linkage, the group demonstrated the controlled release of MTX to the cellular cytosol and the subsequent cytotoxicity to these cancer cells. Cleavage of the MTX from the MNPs was

evaluated over a range of pH values and in the presence of lysozymes to mimic conditions present in the lysosomal compartments. In a more recent investigation from our laboratory, using 2-Carboxyethyl phosphonic acid (CEPA) as the surface-coupling agent and 2, 2'-(ethylenedioxy)-bis-ethylamine (EDBE) as a non-polymeric hydrophilic linker, we were able to synthesize highly stable, folic acid (FA) conjugated magnetite (Fe_3O_4) nanoparticles for specifically targeting the folate-receptor over-expressed cancer cells [104]. The exciting *in-vitro* outcome of this novel surface design was practically a starting point for our multifunctional nanoparticle research, involving phosphonate-grafted MNPs as the precursor material. Later, 2-aminoethyl phosphonic acid (APA) grafted MNPs were used to develop a series of highly water-dispersible, magnetofluorescent iron-oxide folate conjugates for cancer-specific targeting [105]. Encouraged with the high aqueous dispersion stability and good cancer-targeting properties of the as-synthesized conjugates, we moved one-step ahead with the design of a multifunctional, theragnostic nanomedicine for concurrent diagnosis, imaging and cancer-targeted therapy, using N-phosphonomethyl iminodiacetic acid (PMIDA) modified ultrasmall magnetite nanoparticles (USPIO) as the base material. Using appropriate spacers, functional molecules such as rhodamine B isothiocyanate (RITC), folic acid (FA) and methotrexate (MTX) have been coupled to the amine-derivated USPIO-PMIDA support to endow simultaneous targeting, imaging and intracellular drug delivery. Such a multifunctional nanoprobe could selectively target, detect and kill folate-receptor over-expressed cancer cells, while allowing a real-time monitoring of tumor response to drug treatment through dual-modal optical fluorescence and magnetic resonance imaging [106].

Other than receptor mediated targeting approaches, multivalent attachment of small molecules on MNP surface has also emerged as a useful strategy for cancer-specific targeting [107]. Weissleder *et al.* have synthesized a library comprising 146 nanoparticles decorated with different synthetic small molecules. Using fluorescent magnetic nanoparticles, the library against different cell lines were screened and a series of nanoparticles with high specificity for endothelial cells, activated human macrophages or pancreatic cancer cells were discovered. Hits from the last-mentioned screen were shown to target pancreatic cancer in vivo. The method and described materials could facilitate development of functional nanomaterials for applications such as differentiating cell lines, detecting distinct cellular states and targeting specific cell types.

Table 2: A non-exhaustive list of active targeting MNP s useful for cancer diagnosis

Vector	Target	Targeting ligand	Selected Reference (s)
DMSA conjugated SPIO	HER2/neu	Herceptin™	72, 73
USPIO	Human hepatocellular carcinoma (HCC)	SM5-1	74
Quantum dots/ SPIO	EGFR	Sc-FvEGFR	75,
SPIO (magnetofluorescent)	CCRF-CEM acute leukemia	Aptamer	77, 78
SPIO	αvβ3 integrin	RGD peptides	82, 83, 84
SPIO	Nucleolin	F3	85
SPIO	Tumor vessels and stroma	CREKA	87
SPIO	Membrane bound Matrix Metalloproteinase (MMP-2)	Chlorotoxin	88
CLIO	Bombesin (BN)	BN like peptide	89
CLIO	Hepsin	IPLVVPL (IPL-F)	90
CLIO	E-selectin	E-selectin binding peptide	91
Cy 5.5 conjugated CLIO	Underglycosylated mucin-1 antigen (uMUC-1)	EPPT	92, 93
SPIO	Leutinizing Hormone Releasing Hormone (LHRH) receptor	LHRH	94, 95
SPIO	Urokinase Plasminogen Activator receptor (uPAr)	uPA	96
Cy 5.5 conjugated CLIO, QD s entrapped in paramagnetic micelle	Phosphatidylserine	Annexin A5	108
Dextran/PLGA/PEG/PLL/ Silane/ Phosphonate functionalized SPIO	Folate receptor (FR)	Folic acid	100,101,102,104, 105,106
Aminosilane coated SPIO	Folate receptor (FR)	Methotrexate	103

In addition to all the strategies discussed in the previous sections, there are several other approaches for the preferential targeting of MNPs to cancer cells. For e.g. Annexin A5 conjugated MNPs and MNPs encapsulated within protein cage architectures has the potential to serve as a versatile platform for diagnostic imaging. By using Annexin A5 conjugated fluorescent CLIO (AnxCLIO-Cy5.5), Sosnovik et al.[108] have demonstrated the feasibility of obtaining high-resolution MR images of cardiomyocyte apoptosis *in vivo*. More recently, a novel annexin A5-conjugated bimodal nanoparticle has been developed, which comprises of a quantum dot encapsulated in a paramagnetic micelle to enable its use both for optical imaging and MRI [109]. Similarly, genetically modified protein cage architectures have demonstrated the

capability to serve as a multifunctional nanoscale container for simultaneous iron oxide loading and cell-specific targeting.

It should however be remembered that active targeting strategy also has certain limitations. First, the targeting molecules can expose the nanocarriers to the RES system during the circulation. Although *in-vitro* experiments have demonstrated the high accumulation of these nanocarriers into the target cells, studies *in-vivo* reveal that a significant percentage of the injected dose per gram (IDPG) accumulates in the RES organs (liver or spleen) [110], which is quite undesirable unless they are the intended targets, because the anticancer drugs may potentially damage the RES organs and/or be destroyed before they reach the tumor. Second, while the long circulation time is critical for selective distribution of the nanocarriers at the tumor sites, the recognition of these targeted nanocarriers by RES expedites the clearance of the nanocarriers during circulation [111]. The addition of antibodies on the surface appears to appease the shielding effect of the polymeric coating associated with the nanoparticle core. These limitations may partly explain the lack of active targeting nanocarriers currently approved by the FDA. Considering all these points, MNPs targeted with small molecules serve as a better option in comparison to their antibody or peptide targeted variants. Because of their small size versus peptides and antibodies, MNPs targeted with folate or other small molecules provides an added advantage to functionalize the nanoparticle surface with increased number of ligands with limited steric constraints. In the present dissertation, FR mediated targeting have been extensively used for localizing drug/dye loaded MNPs to folate-receptor over-expressing cancer cells.

Despite some of its limitations, active targeting strategy improves the anticancer effect of a drug by facilitating cellular uptake and intracellular retention of the drug carriers. In particular, actively targeted nanocarriers can provide an intracellular drug reservoir, which offers a promising tool for overcoming the multidrug resistance for which the passively targeted nanocarriers do not much avail [112]. On the other hand, tumor distribution of the targeted nanocarriers is more or less guided by the same principle as nontargeted nanocarriers (the EPR effect) and the targeting molecules do not seem to play a role until the carriers reach the target tissues. Therefore, an ideal nanocarrier should be "**maximally targeted and maximally stealth**" so that the nanocarriers in addition to maintaining stealth property during circulation (passive targeting) should be transformable to a more cell-interactive form (active targeting) upon arrival at the target tumor sites. While both the stealth and targeting features are important for effective and selective drug delivery to the tumors, achieving both features

simultaneously is often found to be difficult. Some of the recent targeting strategies have the potential to overcome this challenge. These strategies utilize the unique extracellular environment of tumors such as slightly acidic pH or high level of proteinases, which trigger drug release from the long-circulating nanocarrier and allow these targeted nanoparticles to interact with cells in a tumor-specific manner.

1. 11 Magnetic nanoparticles in cancer therapy

As described in the previous sections, the attachment of targeting agents to MNPs can be used to increase their specific accumulation within diseased tissue. By integrating therapeutic agents, these multifunctional MNPs can serve strictly as a vehicle for drug delivery. The key advantage of these MNPs, as well as well as any nanoparticulate carrier is their high surface area-to-volume ratios, which allows a large number of therapeutic molecules to be attached to individual nanoparticles. Additionally, while utilizing an active targeting strategy for specific delivery, the magnetic properties of the nanoparticles may be simultaneously exploited to provide imaging modality for monitoring of drug delivery through MRI, or an alternative source of treatment through magnetic fluid hyperthermia (MFH) therapy.

1.11.1 MNPs as mediators for hyperthermic treatment of malignant cells

Since the pioneering work of Gilchrist et al. in 1957 [113], magnetic fluid hyperthermia (MFH) has been the aim of numerous *in vitro* and *in vivo* investigations . A variety of MNP based MFH mediators have currently come to the fore. Dextran–magnetite nanoparticles were classified as non-suitable for an intracellular MFH strategy because electron microscopy experiments showed that dextran corona may be attacked by enzymes in lysosome [114]. This problem has however been circumvented by modifying MNPs with positively charged surface groups such as aminosilanes. Such positively charged MNPs showed a very high degree of internalization and long retentivity inside cancerous cells. Daughter cells from a particle-containing parent cell should therefore contain up to 50% of the particle amount of the parent cell. Therefore the descendants would still be cured by future MFH sessions. This approach for treating glioblastoma led to hopeful reproducible results in animal trials and very recently the first successful human treatment has been carried out on a patient with local residual disease (chondrosarcoma). However, in most animal and clinical trials, magnetite nanoparticles were directly injected into the tumour site, restricting this strategy to solid ones. To the best of our knowledge, only one work has yet been reported concerning intravenous

administration of colloidal mediators (the single administration route allowing in theory to treat any small and scattered tumor) [115]. This very early study consisted of the injection of MNPs (dispersed in a solution of sucrose) into a tail vein of rats containing implanted mammary tumours. As expected, particles were internalized by the tumor cells but substantial amounts were also present outside tumor cells, in normal liver tissue and MPS organs with high phagocytic activity. This fact unambiguously proves the necessity of ligand-labelling for active targeting, which appears as one of the most promising aspects of hyperthermia mediated by nanoparticles. Active targeting of tumors using Herceptin™ bound MNPs have already been discussed in the preceding sections. Interestingly, these nanoparticles also exert a therapeutic effect causing cells to undergo arrest during the G1 phase of the cell cycle, thereby reducing cell proliferation. By incorporating Herceptin™ into magnetite nanoparticle loaded liposomes, Ito et al. demonstrated an antiproliferative effect on breast tumor cells. In this *in vitro* study, similar therapeutic effects were observed for the nanoparticle conjugates as that of the free mAb at equal concentrations [116]. Furthermore, the group exploited the magnetic properties of the magnetite nanoparticles to induce hyperthermia resulting in a combined therapeutic approach with an increased cytotoxic effect. More recently, Sonvico et al. have reported a new type of dextran coated maghemite superparamagnetic nanoparticles targeted towards solid tumors through folate [106]. SAR measurements established the potential of these ultra-dispersed nanoparticles as intermediators for targeted, intracellular hyperthermic treatment of cancer cells, over-expressing the folate receptor.

In MNP assisted hyperthermic treatment of malignant cells, temperature control however becomes a necessary concern because local overheating may damage healthy tissue. The smartest way to control hyperthermia is to tune the Curie temperature at a value just above the treatment temperature because in that case particles simultaneously act as both heaters and fuses. Magnetite and maghemite, which are generally used for biomedical applications, display too high Curie temperatures (585 and 477 $^{\circ}$C, respectively). A possible improvement of the MFH technique consists in using mixed magnetic metal oxides or their composites such as cobalt/ nickel ferrite ($CoFe_2O_4$, $NiFe_2O_4$) and derived phases, $La_{1-x}Sr_xMnO_3$ perovskites or $SrFe_{12}O_{19}/\gamma$-Fe_2O_3 composites with lower Curie temperature. Very recently, Ag-doped perovskite manganites particles have demonstrated the effect of adjustable Curie temperature necessary for highly controllable cellular hyperthermia. The magnetic relaxation properties of these particles are comparable with that of SPIO, which allows for real-time monitoring of particle movement and retention through MRI [117].

1. 11. 2. MNPs as targeted carriers for conventional chemotherapeutic agents, peptides, antisense oligonucleotides (ODN) and siRNA

Current nanoparticle-based therapeutic strategies for cancer treatment are mainly based on delivery of chemotherapeutic agents to induce apoptosis or DNA/siRNA to regulate oncogene expression. Traditional drugs such as etoposide, doxorubicin, and methotrexate have been covalently conjugated or encapsulated in MNPs for potential treatment of diseases ranging from rheumatoid-arthritis to highly malignant prostate and breast tumors. Yang et al. investigated the synthesis and release characteristics of poly (ethyl-2-cyanoacrylate) (PECA) coated magnetite nanoparticles containing anti-cancer agents cisplatin and gemcitabine [118]. More recently, Jain et al. have developed a nanoformulation based on oleic acid coated iron-oxide nanoparticles, stabilized with pluronic F-127 to form a water-dispersible system [119]. By incorporating doxorubicin and paclitaxel into this formulation alone or in combination, the group has demonstrated their potential utility as a dual functional probe with combined drug delivery and MR imaging properties.

In addition to drug molecules, MNPs have been investigated as carriers for various therapeutic proteins and peptides. As described earlier in this review, CTX, a peptide with high affinity for a variety of tumors, is currently being evaluated for applications in cancer imaging and therapy, in particular, for the treatment of highly invasive brain tumors such as gliomas . Although the mechanism of this therapeutic effect continues to be investigated, it is believed that the role of CTX as a Cl^--channel inhibitor influences the ability of tumor cells to regulate volume changes which allows for their migration into narrow extracellular spaces [120]. In a very recent study, CTX bound MNPs have been evaluated for the treatment of cancers through the inhibition of cell invasion, while serving as a dual (MR/optical) imaging contrast agent. Investigations from flow cytometry analysis, transmission electron microscopy, and fluorescent imaging reveals that the CTX-enabled nanoparticles deactivated the membrane-bound matrix metalloproteinase 2 (MMP-2) and induced increased internalization of lipid rafts, that contain surface-expressed MMP-2 and volume-regulating ion channels through receptor-mediated endocytosis, leading to enhanced prohibitory effects [121].

In recent years, antisense and gene therapy have become a hot area of research due to their potential to generate a significant impact on medicine. However, the delivery of genes and their resulting transfection efficiencies are often restricted by their short half-life *in vivo*, lack of specificity and poor diffusion across cell membranes as well. The use of MNPs as carriers

for antisense oligonucleotides or gene vectors can overcome many of the problems associated with the targeted delivery of these therapeutic agents. This technique, often referred to as magnetofection has demonstrated their potential utility *in-vitro* and currently being optimized for *in-vivo* applications. Dendrimer modified MNPs have been used to deliver antisense *survivin* ODNs to breast and liver cancer cells.

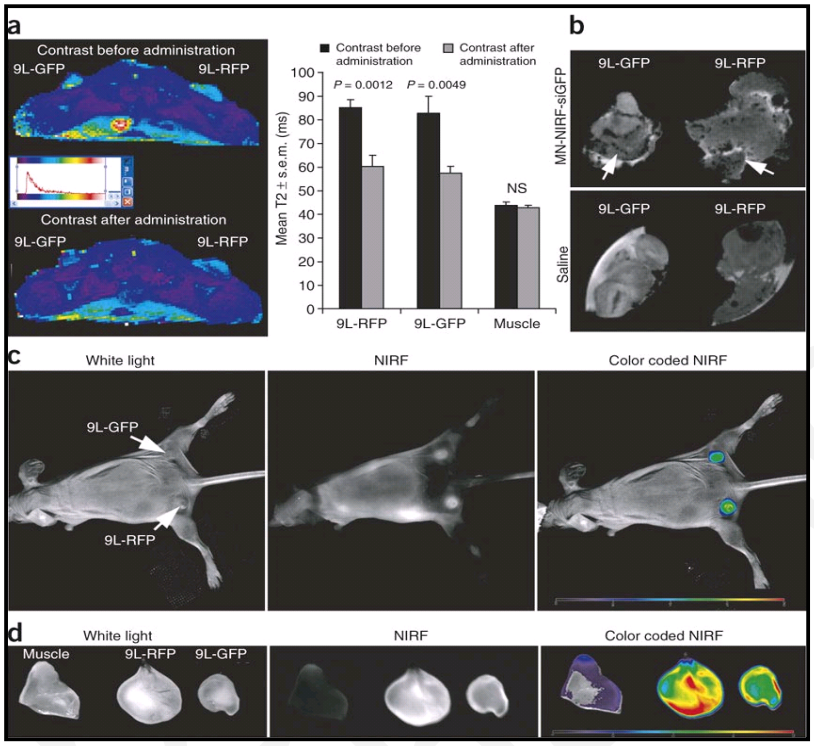

Fig. 1.11 (**a**) *In vivo* MRI performed on mice bearing bilateral 9L-GFP and 9L-RFP tumors (taken as control) before and 24 h after MN-NIRF-siGFP administration, adopted from [121] (MN = magnetic nanoparticle). After injection of the probe, there was a significant drop in T_2 relaxivity associated with the tumors although T_2 relaxation times of muscle tissue remained unchanged. (**b**) *Ex vivo* high-resolution MR images of excised tumors (78 µm isotropic). Distinct foci of signal loss (arrows), reflecting probe accumulation, were easily identifiable in tumors derived from mice injected with the probe but not from saline-injected controls. (**c**) *In vivo* NIRF optical imaging of the same mice as in (**a**) produced a high-intensity NIRF signal associated with the tumors. This confirmed the delivery of the MN-NIRF-siGFP probe to these tissues. (**d**) *Ex vivo* NIRF optical imaging demonstrated a significantly higher fluorescence in tumors than in muscle tissue ($P = 0.0058$).

By coupling ODNs to the positively charged polyamidoamine (PAMAM) coated MNPs, the authors established down regulation of the *survivin* gene and protein within 15 min as well as inhibited cell growth in a concentration and time dependent manner [122]. Similarly, MNPs have also been investigated as carriers or the delivery of small interfering RNA (siRNA). Medarova et al. recently reported on the development of a MNP-based probe for siRNA

delivery and imaging *in vivo*. In this work, MNPs labeled with a NIR dye (Cy5.5) and covalently bound with siRNA were shown to silence green fluorescent protein (GFP) production in a GFP expressing xenograft tumor mouse model. Exploiting the EPR effect, the group demonstrated the feasibility of in vivo tracking of MNP up-taken by tumor with MRI and optical imaging [123] (**Fig. 1.12**).

1.12 Major contributions of the thesis

Despite significant efforts in developing MNP based targeted contrast agents and drug delivery systems, considerable challenges and issues still remain to be resolved before their successful implementation in clinics come to a fruition. For example, heterogeneity of nanomaterials remains a major problem, and it is hard to precisely control the number of functional molecules on the surface of nanoparticles. Designing multifunctional MNPs with well-defined composition, uniform surface modification and reproducible functionalization as also their precise characterization still remains a major challenge for the scientific community. As far as *in vivo* applications of multifunctional MNPs are considered, their purity, aqueous dispersivity and stability in a physiologically tolerable environment remain a major concern. In addition, there are several other obstacles encountered to the *in vivo* application of targeted MNPs for tumor imaging which include heterogeneous expression levels of the targeted receptor in human tumor cells, various physiological barriers preventing the MNP from reaching the targeted cells and a lack of information on the intratumoral distribution and imaging capability of targeted nanoparticles within tumor sites that are relevant to the locations of most human primary and metastatic tumors. Further studies, however, have to be completed before an effective clinical solution emerges.

In addition to addressing many of the lacunas associated with the design and synthesis of multifunctional MNPs for theragnostic applications, the current research effort consists in developing new tool-boxes for the facile, water-based synthesis and biofunctionalization of magnetic iron-oxide nanoparticles for cancer-specific targeting, imaging and therapy. In line with that approach, magnetite nanoparticles with average diameter between 5-15 nm has been synthesized via conventional co-precipitation method or a modified, low-temperature and air-assisted polyol process. To circumvent many of the difficulties associated with traditional polymer or silane based coatings that are commonly being employed for surface modification of iron-oxide based nanoparticles, seldom-used bifunctional phosphonic acid-based coupling agents and/ or hydrophilic mini-PEG like spacers viz. 2, 2′-(ethylenedioxy)-bis-(ethylamine)

have been used for the introduction of reactive functionality on the surface of magnetite nanoparticles. Covalent immobilization of functional ligands viz. fluorophores, targeting agents and chemotherapeutic drugs on to the nanomagnetic support have been successfully accomplished through classical bio-conjugation as well as click chemistry. Considering the advantages of small molecule based targeting ligands such as folic acid as compared to antibodies, peptides or proteins, folate-receptor mediated targeting have been extensively used in the present work for localizing drug/dye loaded MNPs to folate-receptor over-expressing cancer cells. In all cases, the chemotherapeutic drug such as methotrexate or paclitaxel has been covalently conjugated to the surface of MNPs through a pH-labile ester linkage so that while the bond strength makes the NP-drug conjugates highly stable under normal physiological conditions, the drug is susceptible to facile cleavage from the NP surface under harsh environments inside the lysosomes. To further improve the selectivity of bio-conjugation process, "smart", tailored MNPs with mixed surface functional groups, amenable to chemoselective conjugation with multiple diagnostic and therapeutic entities have been attempted and successfully executed through a combined collage of classical bio-conjugation strategies with surface diazo transfer and "click chemistry". All the synthesized materials, developed in course of our research have been extensively characterized using a variety of complementary techniques and their diagnostic as well as therapeutic potential has been evaluated *in vitro.* Although further studies are yet to be done, considering their excellent theragnostic potential *in vitro*, it can be anticipated that the functional MNPs that have been developed in course of the present dissertation work well for future studies *in vivo*.

In 1997, R. Duncan said: ''The drug development process is inevitably lengthy and the breakthroughs more frequently a dream rather than reality''. Certainly, researchers envision a day when a smart nanodevice will be able to fingerprint a particular cancer and dole out the appropriate drug at the proper time in a malignant cell's life cycle, creating individualized platform technologies that can be mixed and matched with new targeting agents that will come from large-scale proteomics programs already in action as well as therapeutics both old and new. To attain this goal, physicians, pharmacologists, biologists, organic chemists, solid state chemists and physicists have to dream altogether and work hand in hand, because if such a "smart", multifunctional drug delivery device can really be implemented in clinics one day, it will necessarily be the result of joint effort.

References

1. Freitas, R.A. What is nanomedicine? *Nanomedicine: NBM* **2005**, *1*, 2-9

2. Taniguchi, N. On the Basic Concept of Nano-Technology Proc. Intl. Conf. Prod. London, Part II British Society of Precision Engineering. **1974**

3. Drexler, E. *Nanosystems: Molecular Machinery, Manufacturing, and Computation. MIT PhD thesis*. New York: Wiley. ISBN 0471575186. **1991**

4. Häfeli, U. History of Magnetism in Medicine in *Magnetism in medicine* (Andrä W, Nowak H, eds.) John Wiley and Sons, Berlin **1997**, 5-25

5. Percival, A. S. Removal Of Iron From Interior Of The Eye By Electro-Magnet, *The British Medical Journal* **1905**, 2, 1176-1177

6. Weissleder, R.; Stark, D.D.; Engelstad, B.L. ; Bacon, B.R.; Compton, C.C.; White, D.L.; Jacobs, P.; Lewis, J. Superparamagnetic iron oxide: pharmacokinetics and toxicity. *Am. J. Roentgenol.* **1989**, *152*, 167–173.

7. Sun, C.; Lee, J. S.H.; Zhang, M. Magnetic nanoparticles in MR imaging and drug delivery. *Adv. Drug Deliv Rev.* **2008,** *60*, 1252–1265

8 (a) Weissleder, R.; Elizondo, G.; Wittenberg, J.; Lee, A.S.; Josephson, L.; Brady, T.J. Ultrasmall superparamagnetic iron oxide: an intravenous contrast agent for assessing lymph nodes with MR imaging. *Radiology* **1990,** *175*, 494–498 (b) Weissleder, R.; Hahn, P.F.; Stark, D.D.; Rummeny, E.; Saini, S.; Wittenberg, J.; and Ferrucci, J.T. MR imaging of splenic metastases: ferrite-enhanced detection in rats, *Am. J. Roentgenol*. **1987**, *149*, 723–726

9. Thiesen, B.; Jordan, A. Clinical applications of magnetic nanoparticles for hyperthermia. *International Journal of Hyperthermia* **2008**, *24*, 467–474

10. (a) Duran, J.D.G.; Arias, J.L.; Gallardo V.; Delgado, A.V. Magnetic colloids as drug vehicles. *Journal of Pharmaceutical Sciences* **2008**, *97,* 2948–2983 (b) Dobson, J. Magnetic nanoparticles for drug delivery, *Drug Development Research* **2006**, 67, 55–60.

11. Pankhurst, Q A.; Connolly, J.; Jones, S. K.; Dobson, J. Applications of magnetic nanoparticles in biomedicine. *J. Phys. D: Appl. Phys.* **2003,** *36*, R167–R181

12. Thorek, D. L. J.; Chen, A. K.; Czupryna, J.; Tsourkas, A. Superparamagnetic Iron Oxide Nanoparticle Probes for Molecular Imaging**.** *Annals of Biomedical Engineering* **2006,** *34,* 23-38.

13. Lu, A.H.; Salabas, E.L.; Schuth, F.; Magnetic nanoparticles: synthesis, protection, functionalization, and application. *Angew. Chem. Int. Ed.* **2007**, *46,* 1222–1244.

14. Lin, X.M.; Samia, A.C.S.; Synthesis, assembly and physical properties of magnetic nanoparticles, *J. Mag. Mag. Mat*. **2006**, *305,* 100–109

15. Tartaj, P.; Morales, M.D.; Veintemillas-Verdaguer, S.; Gonzalez-Carreno, T.; Serna, C.J.; The preparation of magnetic nanoparticles for applications in biomedicine, *J. Phys. D: Appl. Phys* **2003**, *36*, R182–R19

16. Gupta, A.K.; Gupta, M.; Synthesis and surface engineering of iron oxide nanoparticles for biomedical applications. *Biomaterials* **2005**, *26,* 3995–4021

17. Willard, M.A.; Kurihara, L.K.; Carpenter, E.E.; Calvin, S.; Harris, V.G. Chemically prepared magnetic nanoparticles. *Int. Mat. Rev.* **2004,** *49*, 125–170

18. Molday, R.S.; Mackenzie, D. Immunospecific ferromagnetic iron-dextran reagents for the labeling and magnetic separation of cells. *J. Immunol. Methods* **1982**, *52* 353–367.

19. Shen, T.; Weissleder, R.; Papisov, M.; Bogdanov, A. Jr.; Brady, T. J.; Monocrystalline iron oxide nanocompounds (MION): physicochemical properties. *Magn Reson Med*. **1993**, *29***,** 599–604.

20. Sun, S.H.; Zeng, H.; Robinson, D.B.; Raoux, S.; Rice, P.M.; Wang, S.X.; Li, G.X.; Monodisperse MFe_2O_4 (M = Fe, Co, Mn) nanoparticles. *J. Am. Chem. Soc.* **2004**, *126,* 273–279.

21. Lee, J.H.; Huh, Y.M.; Jun, Y.W.; Seo, J.W.; Jang, J.T.; Song, H.T.; Kim, S.; Cho, E.J.; Yoon, H.G.; Suh, J.S.; Cheon, J. Artificially engineered magnetic nanoparticles for ultra-sensitive molecular imaging, *Natural Medicines* **2007**, *13,* 95–99.

22. Xu, C.J.; Sun, S.H.; Monodisperse magnetic nanoparticles for biomedical applications, *Polymer International* **2007**, *56*, 821–826.

24. Bulte, J.W.; Kraitchman, D.L. Iron oxide MR contrast agents for molecular and cellular imaging. *NMR Biomed*. **2004**, *17*, 484–99.

25. Kim, D.; Hong, K.S.; Song, J. The present status of cell tracking methods in animal models using magnetic resonance imaging technology. *Mol Cells* **2007**, *23*, 132–7.

26. Mornet, S.; Sebastien, V.; Grasset, F.; Duguet, E. Magnetic nanoparticle design for medical diagnosis and therapy. *J. Mater. Chem.* **2004**, *14*, 2161 – 2175

27. Stolnik, S.; Illum, L.; Davis, S.S. Long circulating microparticulate drug carriers. *Adv. Drug Delivery Rev.* **1995**, *16* 195–214

28. Allemann, E.; Gurny, R.; Doelker, E.; Drug loaded nanoparticles - Preparation methods and drug targeting issues. *Eur. J. Pharmacol. Biopharm*. **1993,** *39*, 173-191.

29. Weissleder, R.; Lee A.S.; Khaw; B. A.; Shen; T.; Brady, T. J.; Antimyosin-labeled monocrystalline iron oxide allows detection of myocardial infarct: MR antibody imaging. *Radiology*, **1992**, *182*, 381–385.

30. Taupitz, M.; Wagner, S.; Schnorr, J.; Kravec, I.; Pilgrimm, H.; Bergmann-Fritsch H.; Hamm B. Phase I clinical evaluation of citrate-coated monocrystalline very small superparamagnetic iron oxide particles as a new contrast medium for magnetic resonance imaging. *Invest. Radiol.* **2004**, *39*, 394–405.

31. Josephson, L.; Tung, C.H.; Moore, A.; Weissleder, R. High-efficiency intracellular magnetic labeling with novel superparamagnetic-tat peptide conjugates. *Bioconjug. Chem.* **1999**, *10*, 186–191.

32. Kohler, N.; Fryxell, G.E.; Zhang, M.Q. A bifunctional poly(ethylene glycol) silane immobilized on metallic oxide-based nanoparticles for conjugation with cell targeting agents. *J. Am. Chem. Soc.* **2004,** *126***,** 7206–7211.

33. Lee, H.; Lee, E.; Kim, D.K.; Jang, N.K.; Jeong, Y.Y.; Jon, S. Antibiofouling polymer-coated superparamagnetic iron oxide nanoparticles as potential magnetic resonance contrast agents for in vivo cancer imaging, *J. Am. Chem. Soc*. **2006**, *128,* 7383–7389.

34. Martina, M.S.; Fortin, J.P.; Menager, C.; Clement O.; Barratt, G.; Grabielle-Madelmont, C., Gazeau, F.; Cabuil, V.; Lesieur, S. Generation of superparamagnetic liposomes revealed as highly efficient MRI contrast agents for in vivo imaging. *J. Am. Chem. Soc*. **2005,** *127***,** 10676–10685.

35. Soenen Stefaan, J. H.; Vercauteren, D.; Braeckmans, K.; Noppe, W.; De Smedt S.; De Cuyper M. Stable long-term intracellular labelling with fluorescently tagged cationic magnetoliposomes. *ChemBioChem* **2009**, *10***,** 257-67

36. Bulte, J. W. M.; Douglas, T.; Witwer, B.; Zhang, S. C.; Strable, E.; Lewis, B. K.; Zywicke, H.; Miller, B.; Gelderen, P. van; Moskowitz, B. M.; Duncan, I. D.; Frank, J. A. Magnetodendrimers allow endosomal magnetic labeling and in vivo tracking of stem cells. *Nat Biotechnol*. **2001,** *19*, 1141–1147

37. Stober, W.; Fink, A.; Bohn, E. Controlled growth of monodisperse silica spheres in micron size range, *J Colloid Interface Sci*. **1968**, *26*, 62–69

38. Lu, Y.; Yin, Y.D.; Mayers, B.T.; Xia, Y.N. Modifying the surface properties of superparamagnetic iron oxide nanoparticles through a sol–gel approach. *Nano Lett.* **2002**, *2* 183–186.

39. Ma, D.L.; Guan, J.W.; Normandin, F.; Denommee, S.; Enright, G.; Veres, T.; Simard, B. Multifunctional nano-architecture for biomedical applications*. Chem. Mater*. **2006,** *18*, 1920–1927.

40. Xu, C.; Xie, J.; Ho, D.; Wang, C.; Kohler, N.; Walsh, E.G.; Morgan, J. R.; Chin, Y. E.; Sun S.; Au-Fe_3O_4 Dumbbell Nanoparticles as Dual-Functional Probes. *Angew Chem Int Ed Engl.***2007**, *120*, 179-182

41. Xu, C.; Wang, B.; Sun, S.; Dumbbell-like Au−Fe_3O_4 Nanoparticles for Target-Specific Platin Delivery, *J. Am. Chem. Soc.* **2009**, *131*, 4216–4217

42. Strable, E.; Bulte, J. W M.; Moskowitz, B.; Vivekanandan, K.; Allen, M.; Douglas, T. Synthesis and Characterization of Soluble Iron Oxide−Dendrimer Composites. *Chem. Mater.* **2001**, *13*, 2201-2209.

43. Smaihi, M.; Gavilan, E.; Durand, J.; Valentin P. V. Colloidal functionalized calcined zeolite nanocrystals *J Mater. Chem*. **2004**, *14,* 1347-1351.

44. Hubert, M. P.; Guerrero, G.; Vioux, A. Hybrid materials from organophosphorus coupling molecules *J. Mater. Chem.* **2005,** *15*, 3761-3768

45. Sun, E.Y.; Josephson, L.; Kelly, K.A.; Weissleder, R., Development of nanoparticle libraries for biosensing, *Bioconjug. Chem.* **2006**, *17*,109–113.

46. Sun, E.Y.; Josephson, L.; Weissleder, R. Clickable nanoparticles for targeted imaging, *Mol. Imaging*, **2006,** *5*, 122–12847.

47. Hayashi, K.; Moriya, M.; Sakamoto, W.; Yogo, T. Chemoselective Synthesis of Folic Acid-Functionalized Magnetite Nanoparticles via Click Chemistry for Magnetic Hyperthermia. *Chem. Mater.*, **2009**, 21, 1318–1325

48. Maltzahn, G.; Ren, Y.; Park, J. H.; Min, D. H.; Ramana, V. ; Jayakumar, K. J.; Fogel, V.; Sailor, M. J.; Ruoslahti, E. ; Bhatia, S. N.; *In Vivo* Tumor Cell Targeting with "Click" Nanoparticles. *Bioconjug Chem.* **2008**, *19*, 1570–1578.

49. Santra, S.; Kaittanis, C.; Grimm, J.; Perez, J. M. Drug/Dye-Loaded, Multifunctional Iron Oxide Nanoparticles for Combined Targeted Cancer Therapy and Dual Optical/Magnetic Resonance Imaging. *Small* **2009**, *5*, 1862-1868.

50. **(a)** Jung, C. W.; Jacobs, P. Physical properties of superparamagnetic iron-oxide MR contrast agents: Ferumoxides, ferumoxtrans and ferumoxsil. *Magn. Reson. Imaging* **1995,** *13* 661–674 **(b)** Bonnemain, B. Superparamagnetic Agents in Magnetic Resonance Imaging: Physicochemical Characteristics and Clinical Applications A Review *J Drug Target*. **1998**, 6,167-174.

51. Reimer, P.; Balzer, T. Ferucarbotran (Resovist): a new clinically approved RES-specific contrast agent for contrast-enhanced MRI of the liver: properties, clinical development, and applications. *Eur. Radiol.* **2003**, *13***,** 1266-1276.
52. Challa, S. S. R. Kumar. Nanomaterials for cancer diagnosis **2007**, 150

53. Bulte, J. W. M.; Brooks, R. A.; Moskowitz, B. M.; Bryant, L.H. Jr.; Frank, J.A. Relaxometry and magnetometry of the MR contrast agent MION-46L. *Magn. Reson. Med.* **1999,** *42***,** 379-384.
54. Bulte, J. W. M.; Cuyper, M de.; Despres, D.; Frank, J. A.; Preparation, relaxometry and biokinetics of PEGylated magnetoliposomes as MR contrast agent *J. Mag. Mag. Mat*. **1999,** *194*, 3204-209

55. Lubbe, A.S.; Bergemann, C.; Riess, H.; Schriever, F.; Reichardt, P.; Possinger, K.; Matthias, M.; Dorken, B.; Herrmann, F.; Gurtler, R.; Hohenberger, P.; Haas, N.; Sohr, R.; Sander, B.; Lemke, A.J.; Ohlendorf, D.; Huhnt, W.; Huhn D. Clinical experiences with magnetic drug targeting: a phase I study with 4′-epidoxorubicin in 14 patients with advanced solid tumors, *Cancer Res.* **1996,** *56***,** 4686-4693.

56. Alexiou, C.; Arnold, W.; Klein, R.J.; Parak, F.G.; Hulin, P.; Bergemann, C.; Erhardt, W.; Wagenpfeil, S.; Lubbe, A.S. Locoregional cancer treatment with magnetic drug targeting, *Cancer Res.* **2000,** *60*, 6641-6648.

57. Grief, A.D.; Richardson, G. Mathematical modelling of magnetically targeted drug delivery. *J. Mag. Mag. Mat*. **2005**, *293***,** 455-463.

58. Byrne, J. D.; Betancourt, T.; Brannon-Peppas, L. Active targeting schemes for nanoparticle systems in cancer therapeutics. *Adv. Drug Deliv Rev.* **2008**, *60*, 1615-1626.

59. Maeda H. The enhanced permeability and retention (EPR) effect in tumor vasculature: the key role of tumor-selective macromolecular drug targeting. *Adv Enzyme Regul* **2001**, *41***,** 189–207.

60. Chen L.T.; Weiss, L. The role of the sinus wall in the passage of erythrocytes through the spleen. *Blood* **1973**, *41***,** 529–537.

61. Clement, O.; Siauve, N.; Lewin, M.; Kerviler, E. de.; Cuenod, C.A.; Frija, G. Contrast agents in magnetic resonance imaging of the liver: present and future, *Biomed Pharmacother* **1998,** *52***,** 51-58.

62. Stark, D.D.; Weissleder, R.; Elizondo, G.; Hahn, P.F.; Saini, S.; Todd, L.E.; Wittenberg, J.; Ferrucci, J.T. Superparamagnetic iron-oxide-clinical-application as a contrast agent for MR imaging of the liver. *Radiology* **1988,** *168***,** 297–301.

63. Dupin L. New generation of genetically-modified organisms, *Biofutur* **2003,** *39***,** 8.

64. Smirnov P. Cellular magnetic resonance imaging using superparamagnetic anionic iron oxide nanoparticles: applications to in vivo trafficking of lymphocytes and cell-based anticancer therapy. *Methods Mol Biol*. **2009**, *512***,** 333-53.

65. Gullotti, E.; Yeo, Y. Extracellularly Activated Nanocarriers: A New Paradigm of Tumor Targeted Drug Delivery. *Mol. Pharmaceutics*, **2009**, *6*, 1041-1045.

66. Bae, Y. H. Drug targeting and tumor heterogeneity. *J. Control. Rel*. **2009**, *133*, 2-3.

67. Hong, R. L.; Huang, C. J.; Tseng, Y. L.; Pang, V. F.; Chen, S. T.; Liu, J. J.; Chang, F. H. Direct comparison of liposomal doxorubicin with or without polyethylene glycol coating in C-26 tumor-bearing mice: Is surface coating with polyethylene glycol beneficial**.** *Cancer Res*. **1999**, *5*, 3645– 3652.

68. Winau, F.; Westphal, O.; Winau, R. Paul Ehrlich-in search of the magic bullet, *Microbes and Infection* **2004**, *6***,** 786–789.

69. Certain, S.; Lotscher, H.R.; Kunnecke, B.; Seelig, J. Monoclonal antibody-coated magnetite particles as contrast agents in magnetic resonance imaging of tumors**.** *Magn Reson. Med***, 1989**, *12***,** 151–163.

70. Bulte, J.W.M.; Hoekstra, Y.; Kamman, R.L.; Magin, R.L.; Webb, A.G.; Briggs, R.W.; Go, K.G.; Hulstaert, C.E.; Miltenyi, S. Specific MR imaging of human lymphocytes by monoclonal antibody-guided dextran-magnetite particles. *Magn. Reson. Med.* **1992,** *25***,** 148-157.

71. Weissleder, R.; Lee, A.S.; Fischman, A.J.; Reimer, P.; Shen, T.; Wilkinson, R.; Callahan, R.J.; Brady, T.J. Polyclonal human immunoglobulin G labeled with polymeric iron oxide: antibody MR imaging. *Radiology* **1991,** *181***,** 245–249.

72. Artemov, D.; Mori, N., Ravi, R.; Bhujwalla, Z.M. Magnetic resonance molecular imaging of the HER-2/neu receptor. *Cancer Res.* **2003**, *63***,** 2723–2727.

73. Huh, Y.M.; Jun, Y.W.; Song, H.T.; Kim, S.; Choi, J.S.; Lee, J.H.; Yoon, S.; Kim, K.S.; Shin, J.S.; Suh, J.S.; Cheon, J. In vivo magnetic resonance detection of cancer by using multifunctional magnetic nanocrystals. *J. Am. Chem. Soc.* **2005,** *127***,** 12387–12391.

74. Kou, G.; Wang, S.; Cheng, C.; Gao, J.; Li, B.; Wang, H.; Qian, W.; Hou, S.; Zhang, D.; Dai, J.; Gu, H.; Guo, Y. Development of SM5-1-conjugated ultrasmall superparamagnetic iron oxide nanoparticles for hepatoma detection*. Biochem Biophys Res Commun* **2008,** *374* 192-197.

75. Yang, L.; Mao, H.; Wang, Y.A.; Cao, Z.; Peng, X.; Wang, X.; Duan, H.; Ni, C.; Yuan, Q.; Adams, G.; Smith, M.Q.; Wood, W.C.; Gao, X.; Nie, S. Single chain epidermal growth factor receptor antibody conjugated nanoparticles for in vivo tumor targeting and imaging. *Small* **2009,** *5*, 235-243**.**

76. Jain, R.K. Transport of molecules in the tumor interstitium-a review. *Cancer Res.* **1987,** *47***,** 3039–3051.

77. Herr, J.K.; Smith, J.E.; Medley, C.D.; Shangguan, D.; Tan, W. Aptamer-conjugated nanoparticles for selective collection and detection of cancer cells. *Anal Chem.* **2006,** *78***,** 2918-24.

78. Smith, J.E.; Medley, C.D.; Tang, Z.; Shangguan, D.; Lofton, C.; Tan, W. Aptamer-conjugated nanoparticles for the collection and detection of multiple cancer cells, *Anal Chem.* **2007,** *79*, 3075-3082.

79. Folkman, J. Tumor angiogenesis: therapeutic implications. *N Engl J Med* **1971,** *285*, 1182–1186.

80. Ruoslahti, E. Specialization of tumour vasculature, *Nat Rev Cancer*. **2002**, *2*, 83–90.

81. Neri, D.; Bicknell, R. Tumour vascular targeting, *Nat Rev Cancer*. **2005**, *5***,** 436–446.

82. Sunderland, C.J.; Steiert, M.; Talmadge, J.E.; Derfus, A.M.; Barry, S.E. Targeted nanoparticles for detecting and treating cancer. *Drug Development Research* **2006**, *67***,** 70–93.

83. Montet, X.; Montet-Abou, K.; Reynolds, F.; Weissleder, R.; Josephson, L.; Nanoparticle imaging of integrins on tumor cells. *Neoplasia* **2006,** *8,* 214–222.

84. Zhang, C.F.; Jugold, M.; Woenne, E.C.; Lammers, T.; Morgenstern, B.; Mueller, M.M.; Zentgraf, H.; Bock, M.; Eisenhut, M.; Semmler, W.; Kiessling, F. Specific targeting of tumor angiogenesis by RGD-conjugated ultrasmall superparamagnetic iron oxide particles using a clinical 1.5-T magnetic resonance scanner*. Cancer Res.* **2007,** *67***,** 1555–1562.

85. Reddy, G.R.; Bhojani, M.S.; McConville, P.; Moody, J.; Moffat, B.A.; Hall, D.E.; Kim, G.; Koo, Y.E.L.; Woolliscroft, M.J.; Sugai, J.V.; Johnson, T.D.; Philbert, M.A.; Kopelman, R.; Rehemtulla, A.; Ross, B.D. Vascular targeted nanoparticles for imaging and treatment of brain tumors. *Clinical Cancer Research* **2006, 12,** 6677–6686.

86. Xie, J.; Chen, K.; Lee, H.Y.; Xu, C.; Hsu, A. R.; Peng, S.; Chen X.; Sun S. Ultrasmall c(RGDyK)-Coated Fe_3O_4 Nanoparticles and Their Specific Targeting to Integrin $\alpha_v\beta_3$-Rich Tumor Cells *J. Am. Chem. Soc.*, **2008**, *130*, 7542–7543

87. Simberg, D.; Duza, T.; Park, J. H.; Essler, M.; Pilch, J.; Zhang, L.; Derfus, A. M.; Yang, M.; Hoffman, R. M.; Bhatia, S.; Sailor, M. J.; Ruoslahti, E. Biomimetic amplification of nanoparticle homing to tumors. *PNAS* **2007**, 104, 3932–936

88. Veiseh, M.; Gabikian, P.; Bahrami, S.B.; Veiseh, O.; Zhang, M.; Hackman, R.C.; Ravanpay, A.C.; Stroud M.R.; Kusuma, Y.; Hansen, S.J.; Kwok, D.; Munoz, N.M.; Sze, R.W. ; Grady, W.M.; Greenberg, N.M.; Ellenbogen, R.G.; Olson, J.M. Tumor paint: a chlorotoxin: Cy5.5 bioconjugate for intraoperative visualization of cancer foci. *Cancer Res.***2007** *67* 6882–6888.

89. Montet, X.; Weissleder, R.; Josephson, L Imaging pancreatic cancer with a peptide-nanoparticle conjugate targeted to normal pancreas *Bioconjug Chem.* **2006,** *17* 905-911.

90. Kelly, K. A.; Setlur, S. R.; Ross, R.; Anbazhagan, R.; Waterman, P.; Rubin, M. A.; Weissleder, R. Detection of Early Prostate Cancer Using a Hepsin-Targeted Imaging Agent, *Cancer Res.* **2008,** *68,* 2286

91. Funovics, M.; Montet, X.; Reynolds, F.; Weissleder, R.; Josephson L. Nanoparticles for the optical imaging of tumor. E-selectin. *Neoplasia.* **2005**, *10***,** 904-11

92. Moore, A.; Medarova, Z.; Potthast, A.; Da, G. In Vivo Targeting of Underglycosylated MUC-1 Tumor Antigen Using a Multimodal Imaging Probe. *Cancer Research* **2004**, 64, 1821-1827.

93. Medarova, Z.; Pham, W.; Kim, Y.; Dai, G. Moore, A. In vivo imaging of tumor response to therapy using a dual-modality imaging strategy. *Int J Cancer* **2006**, *11***,** 2796-802.

94. Chatzistamou, L.; Schally, A.V.; Nagy, A. Effective treatment of metastatic MDA-MB-435 human estrogen-independent breast carcinomas with a targeted cytotoxic analogue of luteinizing hormone-releasing hormone AN-207. *Clin Cancer Res* **2000,** *6,* 4158–65.

95. Leuschner, C.; Kumar, C.S.; Hansel, W.; Soboyejo, W.; Zhou, J.; Hormes, J. LHRH-conjugated magnetic iron oxide nanoparticles for detection of breast cancer metastases, *Breast Cancer Res Treat*. **2006,** *99*, 163-76.

96. Yang, J.; Lim, E. K.; Lee, H. J.; Park, J.; Lee, S. C.; Lee, K.; Yoon, H. G.; Suh, J. S.; Huh, Y. M.; Haam, S. Fluorescent magnetic nanohybrids as multimodal imaging agents for human epithelial cancer detection *Biomaterials*. **2008,** *29,* 2548-55.

97. Sudimack, J.; Lee, R. J. Targeted drug delivery via the folate receptor, *Adv. Drug Delivery Rev.* **2000,** *41*, 147-162.

98. Gabizon, A.; Horowitz, A. T.; Goren, D.; Tzemach, D.; Mandelbaum-Shavit, F.; Qazen, M. M.; Zalipsky, S. Targeting folate receptor with folate linked to extremities of poly(ethylene glycol)-grafted liposomes: in vitro studies. *Bioconjugate Chem*. **1999**, *10*, 289-298.

99. Lu, Y.; Low, P. S. Folate-mediated delivery of macromolecular anticancer therapeutic agents. *Adv. Drug Delivery Rev*. **2002**, *54*, 675.

100. Choi, H.; Choi, S. R.; Zhou, R.; Kung, H. F.; Chen, I. W. Iron oxide nanoparticles as magnetic resonance contrast agent for tumor imaging via folate receptor-targeted delivery. *Acad. Radiol.* **2004,** *11,* 996.

101. Kim, S. H.; Jeong, J. H.; Joe, C. O.; Park, T. G. Folate receptor-mediated intracellular delivery of recombinant caspase-3 for inducing apoptosis. *J. Control.Release.* **2005,** *103,* 625.

102. Sonvico, F.; Mornet, S.; Vasseur, S.; Dubernet, C.; Jaillard, D.; Degrouard, J.; Hoebeke, J.; Duguet, E.; Colombo, P.; Couvreur, P. Folate-Conjugated Iron Oxide Nanoparticles for Solid Tumor Targeting as Potential Specific Magnetic Hyperthermia Mediators: Synthesis, Physicochemical Characterization, and in Vitro Experiments. *Bioconjug. Chem.* **2005,** *16***,** 1181.

103. Kohler, N.; Sun, C.; Wang, J.; Zhang, M. Q. Methotrexate-modified superparamagnetic nanoparticles and their intracellular uptake into human cancer cells. *Langmuir* **2005**, *21***,** 8858–8864.

104. Mohapatra, S.; Mallick, S. K.; Maiti, T. K.; Ghosh, S. K.; Pramanik, P. Synthesis of highly stable folic acid conjugated magnetite nanoparticles for targeting cancer cells, *Nanotechnology*, **2007,** *18,* 385102.

105. Das, M.; Mishra, D.; Maiti, T. K.; Basak, A.; Pramanik, P. Bio-functionalization of magnetite nanoparticles using an aminophosphonic acid coupling agent: new, ultradispersed, iron-oxide folate nanoconjugates for cancer-specific targeting. *Nanotechnology* **2008**, *19***,** 415101.

106. Das, M.; Mishra, D.; Dhak, P.; Gupta, S.; Maiti, T. K.; Basak, A.; Pramanik, P. Biofunctionalized, Phosphonate-Grafted, Ultrasmall Iron-Oxide Nanoparticles for Cancer-Targeted Therapy and Multimodality Imaging, *Small***, 2009,** 5, 2883 – 2893.

107. Weissleder, R.; Kelly, K.; Sun, E.Y.; Shtatland, T.; Josephson, L. Cell-specific targeting of nanoparticles by multivalent attachment of small molecules*, Nat Biotechnol*. **2005,** *11,* 1418-23108.

108. Sosnovik, D. E.; Schellenberger, E. A.; Nahrendorf, M.; Novikov, M. S.; Matsui, T.; Dai, G.; Reynolds, F.; Grazette, L.; Rosenzweig, A.; Weissleder, R.; Josephson, L. Magnetic resonance imaging of cardiomyocyte apoptosis with a novel magneto-optical nanoparticle, *Magn Reson Med*. **2005,** *54,* 718–24.

109. Van Tilborg, G. A.; Mulder, W. J.; Chin, P. T.; Storm, G.; Reutelingsperger, C. P.; Nicolay, K.; Strijkers, G. J. Annexin A5-conjugated quantum dots with a paramagnetic lipidic coating for the multimodal detection of apoptotic cells, *Bioconjug Chem.* **2006,** *17,* 865-8.

110. Gu, F.; Zhang, L.; Teply, B. A.; Mann, N.; Wang, A.; Radovic-Moreno, A. F.; Langer, R.; Farokhzad, O. C. Precise engineering of targeted nanoparticles by using self-assembled biointegrated block copolymers. *Proc. Natl. Acad. Sci. U.S.A.* **2008**, *105*, 2586– 2591.

111. ElBayoumi, T. A.; Torchilin, V. P. Tumor-Specific Anti-Nucleosome Antibody Improves Therapeutic Efficacy of Doxorubicin-Loaded Long-Circulating Liposomes against Primary and Metastatic Tumor in Mice, *Mol. Pharmaceutics* **2009**, *6*, 246– 254.

112. Bae, Y. H. Drug targeting and tumor heterogeneity, *J. Controlled Release* **2009**, *133*, 2–3.

113. Jordan. A.; Wust, P.; Scholz, R.; Tesche, B.; Fahling, H.; Mitrovics, T. Cellular uptake of magnetic fluid particles and their effects on human adenocarcinoma cells exposed to AC magnetic fields in vitro, *Int J Hyperthermia* **1996**, *12*, 705-722.

114. Jordan, A.; Scholz, R.; Wust, P.; Schirra, H.; Schiestel, T.; Schmidt, H. Endocytosis of dextran and silan-coated magnetite nanoparticles and the effect of intracellular hyperthermia on human mammary carcinoma cells in vitro. *J. Magn Magn Mater* **1999**, *194*, 185-196.

115. Gordon, R. T.; Hines, J. R.; Gordon, D. Intracellular hyperthermia a biophysical approach to cancer treatment via intracellular temperature and biophysical alterations. *Med Hypotheses* **1979, *5*,** 83-102.

116. Ito, A.; Kuga, Y.; Honda, H.; Kikkawa, H.; Horiuchi, A.; Watanabe, Y.; Kobayashi, T. Magnetite nanoparticle-loaded anti-HER2 immunoliposomes for combination of antibody therapy with hyperthermia. *Cancer Letter* **2004,** *212*, 167–175.

117. Melnikov, O. V.; Gorbenko, O. Y.; Markelova, M. N.; Kaul, A. R.; Atsarkin, V. A.; Demidov, V. V.; Soto, C.; Roy, E. J.; Odintsov, B. M. Ag-doped manganite nanoparticles: New materials for temperature-controlled medical hyperthermia. *J Biomed Mater Res A.* **2009,** *91*, 1048-1055.

118. Yang, J.; Lee, H.; Hyung, W.; Park, S. B.; Haam, S. Magnetic PECA nanoparticles as drug carriers for targeted delivery: synthesis and release characteristics. *J. Microencapsul*. **2006,** *23*, 203–212.

119. Jain, T.K.; Richey, J.; Strand, M.; Pelecky, D. L. L.; Flask, C. A.; Labhasetwar, V. Magnetic nanoparticles with dual functional properties: Drug delivery and magnetic resonance imaging, *Biomaterials* **2008,** *29,* 4012–4021.

120. McFerrin, M. B. Sontheimer, H. A role for ion channels in glioma cell invasion, *Neuron Glia Biology* **2006**, 2, 39–49.

121. (a) Deshane, J.; Garner, C. C.; Sontheimer, H. Chlorotoxin inhibits glioma cell invasion via matrix metalloproteinase-2, *Journal of Biological Chemistry* **2003**, *278*, 4135–4144. (b) Veiseh, O.; Gunn, J. W.; Kievit, F. M.; Sun, C.; Fang, C.; Lee, J. S.; Zhang, M. Inhibition of tumor-cell invasion with chlorotoxin-bound superparamagnetic nanoparticles, *Small* **2009,** *5,* 256-264.

122. Pan, B. F.; Cui, D. X.; Sheng, Y.; Ozkan, C. G.; Gao, F.; He, R.; Li, Q.; Xu, P.; Huang, T. Dendrimer-modified magnetic nanoparticles enhance efficiency of gene delivery system, *Cancer Research* **2007**, 67, 8156–8163.

123. Medarova, Z.; Pham, W.; Farrar, C.; Petkova, V.; Moore, A. In vivo imaging of siRNA delivery and silencing in tumors, *Natural Medicines* **2007**, ***13*,** 372–377.

Chapter 2

Biofunctionalization of Magnetite Nanoparticles Using an Aminophosphonic Acid Coupling Agent: Highly Water-Dispersible, Folate-Decorated Iron-Oxide Nanoparticles for Cancer-Specific Targeting

2. 1. Introduction

In recent years, superparamagnetic iron oxide nanoparticles (SPION) with tailored surface chemistry have triggered a surge of interest among the scientific community for their eclectic biomedical applications which include magnetic resonance imaging (MRI) contrast enhancement, tissue repair, immunoassay, detoxification of biological fluids, hyperthermia, drug delivery, cell separation and magnetic field assisted radionuclide therapy [1-6]. All these applications rely on two major advantages of magnetic iron oxides: their low toxicity to human beings [7] and the possibility to exploit their outstanding superparamagnetism for site specific drug targeting and delivery through external static magnetic fields [8]. Although research in this area has achieved substantial advancement, a number of issues still remain to be concerned before successful implementation of iron-oxide nanoparticles in clinics come into fruition.

As for any biomedical application is concerned, the size, charge and surface chemistry of magnetic nanoparticles (MNPs) play a key role in the biokinetics, biodistribution and bioavailability of the nanoparticles *in vivo* [9-10]. As already discussed in **Chapter 1**, magnetic nanoparticles have a natural tendency to agglomerate. Agglomerated nanoparticles are non-biocompatible as they have very short circulation time in blood due to rapid clearance by macrophages of the mononuclear phagocyte system (MPS), before reaching the target cell or tissue [11-12]. Key to the successful application of MNPs is surface modification with amphiphilic polymeric surfactants such as poloxamers, poloxamines or polyethylene glycol (PEG) derivatives which significantly increases the blood circulation time by minimizing or eliminating the protein adsorption to the nanoparticles [13-15]. Although polymeric coatings on MNPs reduce aggregation and improve biocompatibility, their large overall size may significantly limit the tissue distribution, penetration, intravenous delivery and metabolic clearance. This is further accompanied by considerable loss in magnetic response (~40-50%) of the core magnetic material, which negatively influences the magnetic targeting ability of the carrier system in vivo [16]. An alternative approach involves the chemical modification of MNPs with small intermediary molecules or coupling agents that ensure availability of complementary attachment to functional bio-molecules, in addition to sol stabilization. Despite their inconveniences in applications, by far, organosilanes are the most extensively used reagents chosen for metal oxide functionalization. The major drawback in the functionalization with organosilanes is homocondensation in the presence of traces of water,

which may lead to multilayer or even gel formation instead of condensation with the surface [17]. Although much less widespread, organophosphorous compounds offer a promising alternative in the coupling of organic components to metal oxides. The bonding of organophosphorus molecules to the inorganic phase takes place via the formation of strong M–O–P bonds through heterocondensation and coordination [18]. Homocondensation with the formation of P-O-P bridges is unlikely and such bridges, even if formed, are not stable in the presence of water. Organophosphorus coupling agents (OPCA) thus react specifically with metal-oxide surfaces and insist the formation of monolayers, which are highly stable under physiological conditions [19, 20]. Unlike silane based coupling agents, the quality of surface modification is independent on the amount of water added and no preliminary surface conditioning is required.

As for bio-functionalization of magnetic nanoparticles involving organophosphorous coupling molecules is considered, literatures are extremely sparse. In this chapter, we attempt to develop hydrophilic, biocompatible magneto-fluorescent nanoparticles with surface-pendant amine, carboxyl and aldehyde groups, to be later used for bio-conjugation, using a seldom-used aminophosphonic acid coupling agent. Diverse synthetic protocols have been explored to re-decorate these functionalized, magneto-fluorescent nanoparticles with folic acid, a well-known cancer targeting agent. These ultra-dispersed nano-systems were extensively analyzed for their size, surface-charge, surface-chemistry, composition, magnetic properties and colloidal stability. Cell-uptake behaviors and cancer targeting abilities of the different MNP preparations were studied using magnetically activated cell-sorting (MACS) and confocal microscopy, against folate-receptor positive human cervical HeLa cancer cell line.

2.2 Materials and Methods

2.2.1 Materials

$FeCl_3$ and $FeSO_4$ were obtained from Merck, Germany. N-2 (Bromo-ethyl) Phthalimide, Triethyl Phosphite, Succinic anhydride, Glutaraldehyde, 2*,* 2′ -(ethylenedioxy)-bis-(ethylamine) (EDBE), folic acid (FA), di-*tert*-butyldicarbonate (BoC_2O), dicyclohexyl carbodiimide (DCC), Trifluoroacetic acid (TFA), *N*-hydroxysuccinimide (NHS), 1-[3-(Dimethylamino) propyl]-3-ethylcarbodiimide hydrochloride (EDC), Sodium Cyanoborohydride ($NaBH_3CN$), Trinitrobenzene sulphonic acid (TNBS), Rhodamine isothiocyanate (RITC), MTT [3-(4,5-dimethylthiazol-2-yl)-2,5-diphenyltetrazolium] bromide,

4′, 6-diamidino-2-phenylindole dihydrochloride (DAPI) were purchased from Sigma Chemical Co. (St. Louis, MO, USA). Commercially available dimethyl sulphoxide (DMSO) was purified by reduced pressure distillation. Pyridine and triethyl amine were purified by distillation over KOH. 2-Aminoethyl phosphonic acid (APA) was synthesized according to a reported literature procedure, which consisted of refluxing N-2 (Bromo-ethyl) Phthalimide with triethyl phosphite under inert atmosphere, followed by hydrolysis with HBr [21]. γ-{N-{2-[2-(2-aminoethoxy) ethoxy] ethyl} folic acid (FA-EDBE) was synthesized according to the standard protocol developed in our laboratory and has been reported elsewhere [22].

2.2.2 Synthesis methodology

2.2.2.1 Synthesis of magnetite nanoparticles

Superparamagnetic nanosized magnetite was prepared by controlled chemical co-precipitation of Fe^{2+} and Fe^{3+} (1:2 ratio) from ammoniacal medium at 80° C under argon atmosphere. In a typical experiment, ferrous sulphate (1 mmol) and $FeCl_3$ (2 mmol) were dissolved in 10 ml of de-ionized and de-oxygenated water. The resulting solution was vigorously stirred and heated to 80° C under an inert argon atmosphere. Subsequently, about 5 ml of 32% ammonia solution was injected into the flask and stirring was continued for another 20 minutes to allow the growth of the nanoparticles. The solution was then cooled to room temperature and the resulting particles were subjected to magnetic decantation followed by repeated washing with distilled water. The pH of the suspension was adjusted to near neutral by dropwise addition of dilute HCl. Particles were re-washed with distilled water and finally separated through magnetic concentration

2.2.2.2 Surface modification with 2-Aminoethyl-Phosphonic acid (APA)

For amine functionalization, a freshly prepared aqueous solution of APA (1 mmol) was added to around 200 mg of colloidal suspension of magnetite nanoparticles at pH~ 6 with sonication using a high intensity ultrasonic probe (Branson Ultrasonics–2210) operated at 20 kHz with power 100 W for an hour. The resulting nanoparticle suspension was then stirred vigorously on a magnetic stirrer at 60°C for 12 hours. The particles were then isolated with a rare earth magnet, washed three times with de-ionized water and resuspended in PBS. These amine-functionalized nanoparticles (Fe_3O_4-NH_2) were divided into two parts: a part was labeled with RITC and the subsequent functionalization-steps as well as folate-conjugation were

performed using these magnetofluorescent nanoparticles while the other part was kept unlabeled and further functionalizations (including carboxyl-modification as well as folate-conjugation reactions) were performed with this unlabeled part, using the same protocol. The different nanoparticle preparations, obtained from these unlabeled part were freeze-dried and preserved for various physicochemical characterizations.

2.2.2.3 Synthesis of amine-functionalized magnetofluorescent nanoparticles (1. 1)

1 mg of rhodamine isothiocyanate (RITC) was dissolved in 1ml of DMSO-H_2O mixture and added dropwise to an aqueous suspension of APA functionalized nanoparticles at pH ~ 8. The resulting suspension was sonicated for an hour in the dark. Particles were recovered by magnetic concentration and washed thoroughly with de-ionized water.

2.2.2.4 Synthesis of carboxyl-functionalized magnetofluorescent nanoparticles (1. 2)

To a freshly prepared solution of succinic anhydride (1 mmol) in distilled DMSO (5 ml) aminated, magnetofluorescent nanoparticles (~50 mg nanoparticles dispersed in 10 ml DMSO) were added dropwise with ultrasonication. A catalytic amount of triethylamine was added to the resultant suspension and the reaction was continued for about twenty-four hours in the dark. The particles were finally recovered by magnetic concentration and washed thoroughly with de-ionized water to remove the unreacted impurities.

2.2.2.5 Syntheses of iron-oxide folate conjugate (2. 1)

To conjugate **1.1** with folic acid, FA (0.025 mmol) was dissolved in ~10 ml of DMSO due to the limited solubility of FA in aqueous medium. The resulting solution was then mixed with an aqueous solution of 1-ethyl-3-(3-dimethylamino)-propyl) carbodiimide (EDC) (75 mmol) and N-hydroxy succinimide (NHS) (15 mmol). The pH of the solution was then adjusted to 8 by dropwise addition of pyridine. An aqueous dispersion of around 200 mg of APA functionalized nanoparticles was added to it and the reaction mixture was stirred overnight at 37°C in the dark. Following the conjugation of FA, the modified particles were again isolated with a rare earth magnet, washed 5 times with de-ionized water and re-dispersed in PBS.

2.2.2.6 Syntheses of iron-oxide folate conjugate (2.2)

To conjugate **1.2** with folic acid, 25 mg of succinylated nanoparticles was dispersed in 10 ml aqueous solution of EDC (75 mmol) and NHS (15 mmol). The pH of the resulting suspension was adjusted to 8 and kept in the dark for 2h. To the resulting suspension, FA-EDBE (50 mg dissolved in 5 ml DMSO) was added dropwise. The suspension was agitated overnight in the dark at 37 ° C. Finally the particles were washed thoroughly, recovered through magnetic concentration and re-dispersed in PBS. Similar procedure was adopted for the immobilization of FA nanoparticles on **1.2** using the HMDA-linker.

2.2.2.7. Syntheses of iron-oxide folate conjugate (2.3)

The first steps towards the synthesis of iron-oxide folate conjugate **2. 3** consisted of interchanging the primary amine groups of **1.1** with aldehyde (-CH=O) groups via glutaraldehyde treatment as described in earlier reports. Finally, immobilization of FA-EDBE onto the aldehyde-functionalized magnetite nanoparticles (**1. 3**) was achieved through reaction of the aldehyde groups with amine groups of FA-EDBE, followed by reductive amination with sodium cyanoborohydride. In a typical procedure, about 1 ml of 1% (w/v) glutaraldehyde solution in PBS (pH=7.4) was added to a 10 ml aqueous dispersion of the amine functionalized nanoparticles (2.12 mg/ml) and the suspension was incubated with shaking for 3 h at 20°C. Nanoparticles were washed repeatedly with PBS to remove any excess glutaraldehyde. 25 mg of FA-EDBE dissolved in 5 ml of DMSO was added to an aqueous dispersion of the glutaraldehyde-activated nanoparticles and left to overnight stirring. The resulting nanoparticles were washed thoroughly with PBS and placed in 5 ml of $NaBH_3CN$ solution [0.5% (w/v) in PBS] for 30 minutes at 18°C. Finally, the nanoparticles were thoroughly washed with distilled water, separated through magnetic decantation and resuspended in PBS. Similar procedure was adopted for the covalent attachment of FA onto the surface of **1.3** using the HMDA-linker.

2.2.3 Characterizations

2.2.3.1. Chemical structures

Chemical structure of synthesized APA and EDBE were analyzed and authenticated by Fourier Transform Infrared (FTIR) Spectroscopy (Thermo Nicolet Nexux FTIR model 870 spectrometer), proton (^{1}H) nuclear magnetic resonance (NMR) spectroscopy (Bruner, 400 MHz) and mass spectrometry (VG Autospec Mass spectrometer).

2.2.3.2 Quantification of different functional groups on the surface of nanoparticles

The determination of free amino groups on the surface of **1.1** was performed using the 2,4,6-trinitrobenzenesulfonic acid (TNBS) method according to the procedure adapted by Edwards-Levy et al [23]. This procedure consisted of the incubation of nanoparticles with an excess of TNBS and back titration of the unreacted amount of the reagent. The number of carboxyl and aldehyde groups on **1.2** and **1.3** was also quantified by determining the residual amino group concentration by TNBS assay. In a typical procedure the amine functionalized magnetofluorescent nanoparticles were washed three times with water, followed by redispersion with 4% sodium bicarbonate solution (pH 8.5). 2 ml of nanoparticle dispersion and 4.0 ml of TNBS solution (4.0 µmol/ ml in 4% sodium bicarbonate solution) were added. The reaction mixture was shaken at 400 rpm for 1 h at 40°C. Nanoparticles were isolated from the supernatant by magnetic concentration. In order to measure an unreacted TNBS, 0.9 ml of the supernatant was added to 0.1 ml of valine water solution (40 µmol/ ml) and incubated at 40°C in the dark for 1 h. Then, 5 ml of HCl (0.5 µmol/ ml) were added and the absorbance of solution was measured at 410 nm against a blank prepared as described above, but containing 0.1 ml of trichloroacetic acid (1%) instead of valine solution. The content of amino groups on the particle surface was calculated relative to a TNBS reference that was treated in the same manner as described above, using water instead of the nanoparticle dispersions.

2.2.3.3 Crystal structure

Phase analysis of the synthesized magnetite nanopowder was performed by the X-ray diffraction (XRD) data analysis using a PW 1729 X-ray diffractometer (Philips, Holland) with CoK_α radiation (λ = 0.179 nm). The XRD technique was also employed to determine the crystallite size of the synthesized nanopowder. Crystallite size was calculated using the

Scherrer's equation i. e. $D = 0.9 \lambda / \beta_{sample} \cos \theta$, where D is the average diameter in Å, β is the broadening of the diffraction line measured at half of its maximum intensity in "radian", λ is the wavelength of X-rays, and θ is the Bragg's diffraction angle. The peak width β_{sample} is calculated using the equation: $\beta_{sample}^2 = \beta_{exp}^2 - \beta_{inst}^2$, where β_{exp} is the experimentally measured full width of the peak at half of the maximum intensity and β_{inst} is the instrumental broadening contribution determined from a silicon standard.

2.4.3.4 Size and morphology

Size and morphology of the as-synthesized nanoparticles were observed through a Phillips CM 200 transmission electron microscope (TEM) with an acceleration voltage 200 kV. The TEM samples were prepared by depositing a few drops of the respective nanoparticle preparations ultrasonically dispersed in water for 2 h on separate carbon-coated copper grids.

2.4.3.5 Nanoparticle size and surface charge

The hydrodynamic (HD) size of the particle aggregates was measured by laser light scattering using a Brookhaven 90 Plus particle size analyzer. Hydrodynamic diameter measurements were performed at 20°C and 90°angle, after dilution of the sample to 150 μg/ mL iron oxide concentration either in NaCl solutions of increasing concentrations (up to 1 M), or in 0.01M phosphate buffers at various pH (ranging from 4 to 9). Each sample was analyzed six times for a total period of analysis of 20 min. The hydrodynamic sizes of the different nanoparticle preparations were also measured against time in different pH. The surface charge of the nanoparticles was investigated through ξ potential measurements (Zetasizer 4, Malvern Instruments, UK) after dilution of the samples in 0.01 M phosphate buffers at pH between 4 and 9. Smoluchowsky approximation was applied in the calculation of zeta potential.

2.4.3.6 Surface Chemistry

The functional groups present on the surface of **1.1-1.2** as also their folate-linked counterparts (**2.1-2.3**) were studied using a Thermo Nicolet Nexux FTIR model 870 spectrometer. The surface compositions of the different nanoparticle preparations were obtained by analyzing X-ray Photoelectron Spectroscopic (XPS) data using Al K_α excitation source in an ESCA-2000 Multilab apparatus (VG microtech).

2.2.3.7 Magnetic properties

All magnetization measurements were carried out at room temperature using vibration sample magnetometry (VSM). The magnetization data obtained from VSM measurements were further compared with the results of thermal analysis studied using a TG analyzer (Diamond TG-DTA, Perkin Elmer, USA) at the heating rate 15°C/ min under airflow (100 ml/min).

2.2.3.8 *In vitro* cellular uptake study

- **Cell culture:** The cells cultivated for in vitro experiments were human cervix adenocarcinoma, HeLa and human osteosarcoma, MG-63 cell lines, obtained from the National Centre for Cell Sciences (NCCS) Pune, India. All cell lines were cultured on Dulbecco Modified Eagle's Medium (DMEM) and Minimal Essential Medium (MEM) respectively with 10% fetal calf serum, 100 units ml^{-1} penicillin and 100 μg ml^{-1} streptomycin, 4 mM L-glutamine at 37° C in a 5% CO_2 and 95% air humidified atmosphere.

- **Nanoparticle mediated cytotoxicity:** 4×10^5 HeLa cells were seeded to 96 well tissue culture plates in a total volume of 180 μl of complete media and kept for 18 h, following which 20 μl of different nanoparticle preparations were added to the cells at different concentrations (50, 100 and 200 μg ml^{-1}), incubated for 4 h at 37 °C in a humidified incubator (HERA cell) maintained at 5% CO_2. After 4 h incubation, MTT (4 mg/ml) was added to each well at the strength of 10% (v/v) and incubated for further 4 h at 37°C. Subsequently, the media containing MTT was removed and 200 μl of DMSO was added to dissolve the formazan crystals. The absorbance was measured using an ELISA plate reader (Biorad, USA) at 595 nm.

- **Intracellular uptake studies:** Nanoparticle uptake by different cell lines were studied by magnetically activated cell sorting (MACS) and fluorescence/ confocal microscopic methods. The effect of surface-coating on the uptake of nanoparticles by HeLa or MG-63 cells was evaluated by culturing these cells with different nanoparticle preparations in the absence of folic acid in the culture medium. After 4 h of incubation, the cells were washed to remove free nanoparticles and cell sorting was performed with MACS. Nanoparticle uptake in the cell lines was proportional to the percentage of magnetically positive cells detected using this method. Three replicates

were measured and the results were averaged with percentage error determined through calculating the standard deviation from the mean. For fluorescence or confocal laser scanning microscopy, the cells were smeared on a clean glass slide, fixed with 3.7% formaldehyde for 15 min, permeabilized with 0.1% Triton X-100 and stained with 1 μg/ml DAPI for 5 min at 37° C. Fluoroscence images were acquired on an Olympus IX 70 fluorescence microscope while confocal images were acquired on Olympus, Fluoview 1000 confocal laser-scanning microscope using a 488 nm laser.

- Interaction of nanoparticles with macro-phages in-vitro: Macrophages were isolated from Swiss albino mice by peritoneal lavage in chilled PBS and enriched by adherence to the petriplate surface. To 5×10^5 macrophages in 2 ml complete DMEM media 200 μg of each type of nanoparticles (2.1-2.3) were added and incubated for 12 h at 37 ° C in a humidified incubator. After incubation the petriplates were washed with warm PBS and phagocytic-uptake was quantified using magnetically activated cell-sorting (MACS).

2. 3. Results and Discussions

Superparamgnetic magnetite nanoparticles were prepared by the traditional co-precipitation method, as reported previously by Bee and Massart [24], with minor modifications. Phosphonic acid derivatives that undergo facile formation of organic monolayer on the surface of nanoparticles are useful for introducing polar functional groups ($-NH_2$, $-CO_2H$, -OH) on the surface. These polar render the nanoparticles stable with respect to aggregation and keep them well-dispersed in aqueous media. In the present study, 2-Aminoethylphosphonic acid (APA) has been chosen to form an amine functionalized phosphonate monolayer onto the magnetic support. Magneto-fluorescent analogue of these aminated nanoparticles was subsequently procured by covalent immobilization of rhodamine B isothiocyanate (RITC) on the particle surface via thiourea linkage. This aminated, magneto-fluorescent base (**1.1**) is amenable to conjugation with a diverse array of small molecules through sulfhydryl, carboxyl, anhydride or imine chemistry, allowing easy manipulation of the surface-functionality. The amine groups on **1.1** were interchanged with carboxyl groups through a ring-opening linker elongation reaction with succinic anhydride whereas aldehyde functionality was introduced

by treating the as-synthesized, amine-functionalized nanoparticles with glutaraldehyde (**Scheme 2.1**).

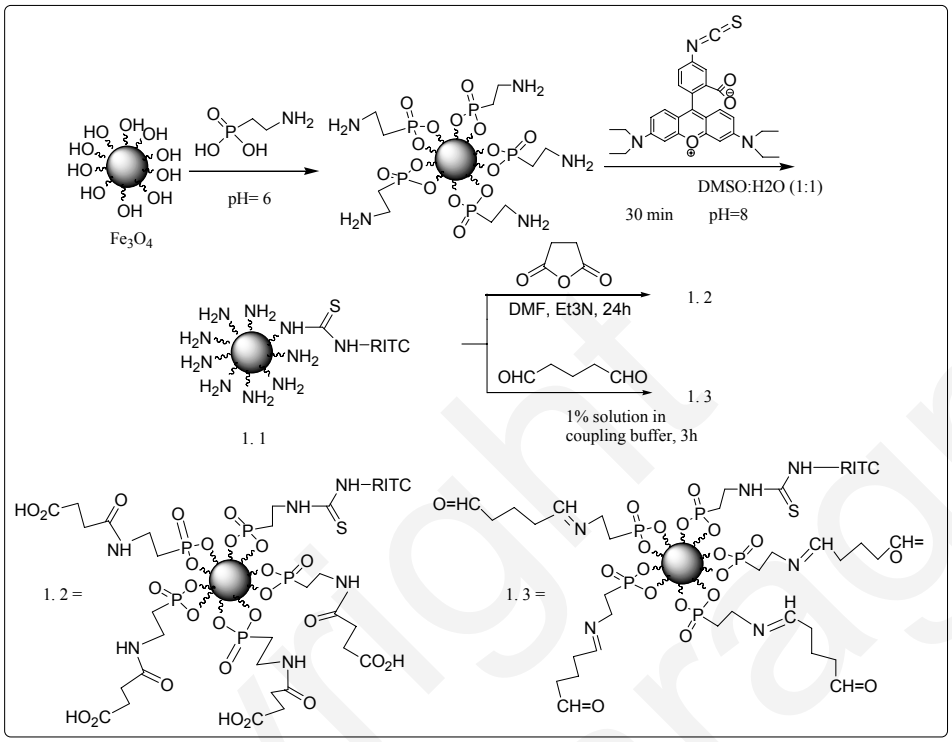

Scheme 2.1: Synthesis of amine, carboxyl and aldehyde functionalized magneto-fluorescent nanoparticles: The surface of superparamagnetic magnetite nanoparticles is first modified with 2-Aminoethyl Phosphonic acid (APA) to form an amine-functionalized phosphonate monolayer. Carboxyl and aldehyde-functionalized magnetofluorescent nanoparticles are prepared from the RITC-labeled aminated nanoparticles using anhydride and imine chemistries respectively.

The TNBS method was used to determine the number of amino groups present on the surface of APA functionalized magnetite nanoparticles, labeled with RITC. The procedure included the incubation of **1.1** with an excess of TNBS and the back titration of the unreacted amount of the TNBS. The number of carboxyl and aldehyde groups on the surface of **1.2 -1.3** were also quantified using the same method by determination of residual amine concentration on the surface of magnetite nanoparticles. The results have been summarized in **Table 2. 1**. As evident from the results of TNBS assay, the amine grafting density on the nanoparticle surface was considerably high and these amine groups were quantitatively converted into carboxyl and aldehyde groups, following reaction with succinic anhydride or glutaraldehyde.

Table 2.1: Quantification of different functional groups present on the nanoparticle surface

SPION modification	Functional end group	Surface amine density (μmol/mg)	Concentration of respective functional end-groups (μmol/mg)
Amino	$-NH_2$	6.76	6.76
Carboxylic acid	-COOH	0.23	6.53
Aldehyde	-CHO	0.34	6.42

Magnetofluorescent nanoparticles, containing reactive, surface-pendant amine, carboxyl and aldehyde functionalities were "decorated" with folic acid, utilizing diverse conjugation strategies, elaborated in Scheme **2.2**.

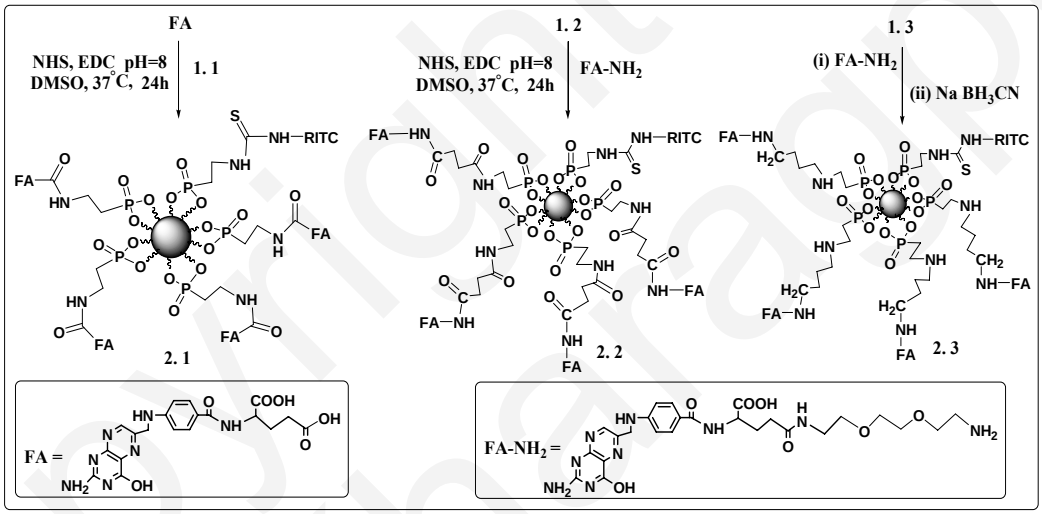

Scheme 2.2: Synthesis of iron-oxide folate conjugates **2.1-2.3** using standard bio-conjugation protocols

The active $-NH_2$ groups present on APA functionalized nanoparticle surface were covalently conjugated with FA via nonselective activation of the carboxyl groups in its glutamic acid moiety by the carbodiimide method. This method could have led to the formation of two structural isomers in which FA is linked either through the α-carboxyl or γ-carboxyl group of its glutamic acid moiety. However, the folate linked via its γ-carbonyl group is formed as the major isomer which retains a strong affinity towards its receptor, whereas its α-carbonyl derivatives are not recognized as readily [25, 26]. While folic acid is directly grafted onto the surface of amine functionalized magnetite nanoparticles via carbodiimide activation, for conjugation of the same with carboxyl or aldehyde functionalized nanoparticles, an appropriate spacer was necessary. We choose to attach the folate and carboxylic acid ($-CO_2H$) functionalized nanoparticles to distal ends of a nonpolymeric, hydrophilic spacer 2, 2-

(ethylenedioxy)-bis-ethylamine [EDBE] via standard protocol. EDBE, comprising of a mini PEG-like backbone was chosen as the linker with an aim to improve the hydrophilicity and bio-compatibility of the magnetite nanoparticle-folate-conjugate system, while increasing the range of its accessibility to receptor sites [27]. Immobilization of FA-EDBE onto the aldehyde-functionalized nanoparticles was accomplished through Schiff's base formation, followed by reductive amination with $NaBH_3CN$ to afford the iron-oxide folate conjugate **2.3**.

The high resolution X-ray diffraction pattern of unmodified magnetic nanoparticles (i.e. without phosphonic acid) has been displayed in figure **2.1**. The d values correspond to that of spinel phase magnetite [Fe_3O_4] (JCPDS card no. 77-1545). The broadening of XRD peaks is consistent with nanocrystalline nature of the synthesized magnetite nanopowder. Taking into account the broadening of each peak in X.R.D., mean crystallite size was calculated applying Scherrer's equation (experimental section can be referred for details). The mean crystallite size was found to be around 8 nm.

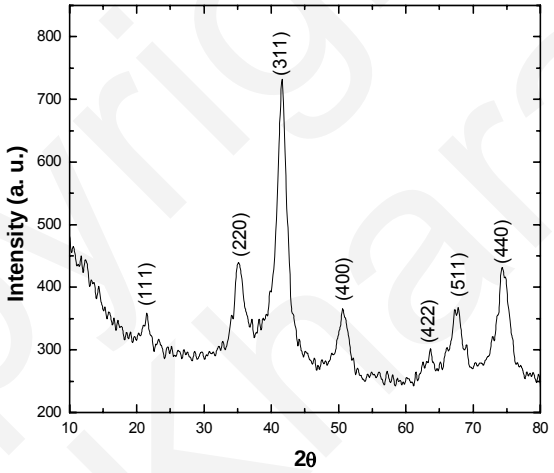

Fig. 2.1: X-Ray diffraction pattern of superparamagnetic magnetite nanopowder

Transmission Electron micrograph of bare magnetite nanoparticles, presented in Fig.**2.2 (a)** shows that particles have spherical morphology with some agglomeration, which is obvious because of magnetic dipolar interactions. TEM observation of APA functionalized magnetite nanoparticles [**Fig. 2.2 (b)**] indicates that particles are more or less uniform and presents considerable dispersancy. Immobilization of functional ligands had little or no effect on the mean diameter of particles, which implied that the additional organic groups did not significantly increase the overall volume of the nanoparticle system.

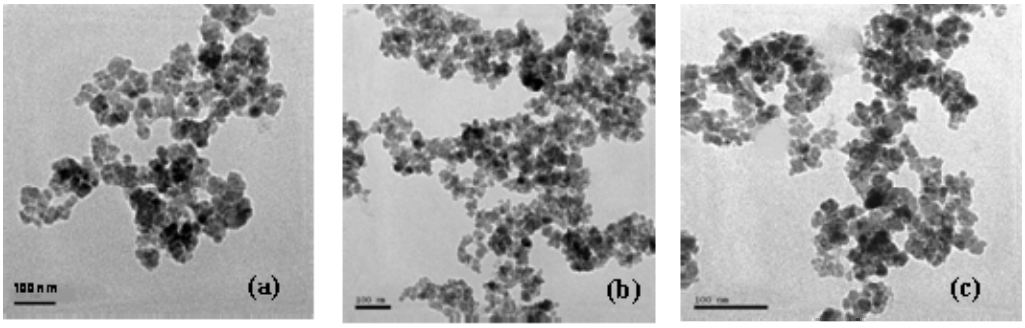

Fig. 2.2: TEM micrograph of **(a)** bare magnetite (Fe_3O_4) nanoparticles **(b)** APA funtionalized magnetite nanoparticles (Fe_3O_4-NH_2) and **(c)** Carboxyl-functionalized magnetite nanoparticles (Fe_3O_4-COOH).

The transmission infrared spectra of unmodified as well as amine functionalized magnetite nanoparticles for the range 400-4500 cm-^{1} have been depicted in **Fig. 2.3.** The unmodified iron oxide nanoparticles show a broad band around 3300 cm-^{1} indicative of the presence of -OH groups on nanoparticle surface. FTIR spectrum of bare magnetite displays a strong band around 580 cm-^{1} characteristic of the Fe-O vibration related to the magnetite core. Following APA functionalization, the peak at 580 cm-^{1} shifts towards higher wave numbers with a concomitant decrease in the intensity of the band at this position, which, however, can be attributed to the chemisorption of the phosphonic acid on magnetite surface. A broad peak around 1034 cm-^{1} accounts for Fe-O-P and P=O stretching bands superimposed on one another while the bands at 2855 and 2915 cm-^{1} presents $–CH_2$ stretching vibration of the phosphonic acid moieties, adsorbed onto metal oxide surface. In addition, the band at 1629 cm^{1}, associated with –NH bending (scissoring) vibration testify to the successful modification of magnetite surface by primary amine groups. Surface treatment of these amine-functionalized nanoparticles with succinic anhydride leads to the formation of carboxyl-terminated magnetite nanostructures. The typical vibrations of $–CO_2H$ group (1710 cm^{-1}) and the amide linkage [1637 (amide I) and 1556 cm^{-1} (amide II)] appear in the corresponding FTIR spectrum, which substantiates the successful derivatization of the surface-amino group with succinic anhydride. It should however be noted that the intensity of the $–CO_2H$ vibration at 1710 cm^{-1} is relatively weak, which is possibly a consequence of intraparticle hydrogen bonding between the surface $–CO_2H$ groups. This, however, shifts the >C=O stretching bands of carboxylic acids to a much lower wave number (~1625-1650 cm^{-1}) and superimposes with the amide I band.

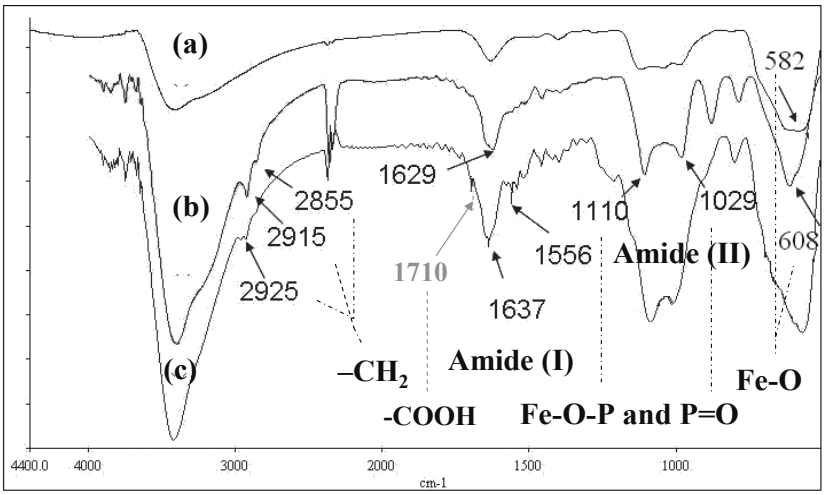

Fig. 2.3: FTIR spectra of **(a)** Bare magnetite nanoparticles **(b)** Fe_3O_4-NH_2 and **(c)** Fe_3O_4-CO_2H

FTIR spectroscopy was used to analyze the surface-chemistry of the as-prepared iron-oxide folate nanoconjugates. FA-standard presents characteristic bands of FA at 1603 and 1694 cm^{-1}. The FTIR spectra in **Fig. 2.4** show that the characteristic peaks of the functionalized nanoparticles as well as free FA appeared on the spectrum of the respective conjugates (**2.1-2.3**), indicating successful tailoring of the nanoparticle surface with FA. FTIR spectrum of **2.1** shows increased absorbance at 1635 cm^{-1} and appearance of a new band around 1555 cm^{-1}, arising from the amide bands within the FA structure as well as the amide bonding between FA and APA functionalized nanomagnetite. That this method yielded a covalent nanoparticle-FA conjugate was further established with the control reaction, conducted in the absence of cross-linking agent (EDC). The synthetic reaction carried out in the absence of EDC did not yield a stable conjugate but rather a mixture from which FA could be simply washed away. This fact along with the spectroscopic evidences established that the conjugates were chemically different. Similarly, following the immobilization of FA-EDBE on the carboxyl-terminated nanoparticles, the amide carbonyl bands at 1635 and 1556 cm^{-1} intensified**.** Although characteristic bands of FA are present in the FTIR spectrum of **2.3**, unlike **2.1** and **2.2** no absorption band could be visualized around 1550-1555 cm^{-1}; instead a medium intensity band corresponding to –C-N stretching vibration appears around 1258 cm^{-1}, testifying to the immobilization of FA-EDBE on APA-functionalized nanoparticle surface through a stable secondary amine linkage.

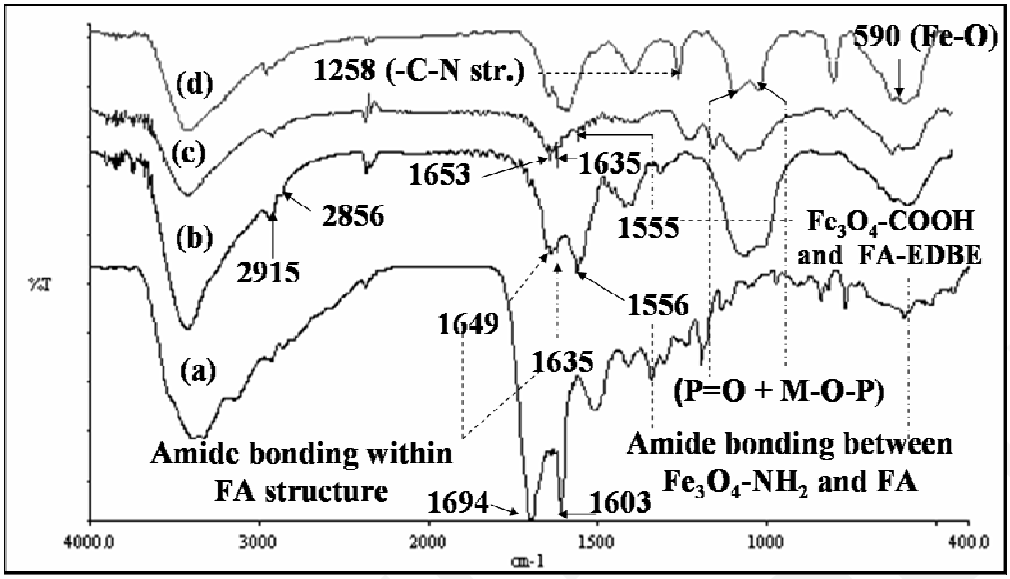

Fig. 2.4: FTIR spectra of **(a)** FA std. **(b**) Iron-oxide folate conjugate: **2.1 (c**) Iron-oxide folate conjugate: **2.2** and (**d**) Iron-oxide folate conjugate: **2. 3**

Although FTIR analyses explicitly validate the successful bio-functionalization of magnetite surface, the findings were re-authenticated using XPS analyses. The high-resolution O1s spectrum of pure magnetite (**Fig. 2.5**) displays two peaks at 531 eV and 532.1 eV, which can be attributed to oxygen in an O-H component of ferric oxohydrides and to oxygen in an Fe-O component of ferric oxides and oxohydrides respectively. Following APA modification, the broad shoulder for O1s spectrum exhibited an additional peak around 530.8 eV corresponding to oxygen in Fe-O-P suggesting the chemisorption of phosphonate head-groups on the surface of iron oxide. Correspondingly, a significant decrease in the intensity of O-H peak (532.3 eV) is also indicative of the reaction between APA and –OH groups on nanoparticle surface. The high-resolution N1s spectrum of APA functionalized nanoparticles reveals a broad shoulder at 398.6 eV corresponding to the free amino groups on the surface. At the ring opening linker elongation step, the -NH_2 peak completely disappears with concomitant appearance of a new peak at 400.6 eV, indicating the formation of amide (-NHCO) linkage between the amine groups of APA and succinic anhydride. The high resolution scans for C1s of Fe_3O_4-APA-FA shows a broad shoulder in between 280-291eV. Taking bulk C1s at 285 eV as standard, the broad shoulder can be deconvoluted into three peaks at 284.2, 286.3 and 288.6 eV, which could be attributed to –C-C-, -NH-C=O and –CO_2H groups respectively. The broad shoulders for N 1s appeared at 398.7 eV and 401.3 eV, corresponding to the free –NH_2 groups (native to the pteridine rings in FA) and amide (-NH-C=O) bonding within FA structure as also the

amide linkage between FA and nanoparticle surface. The O1s spectrum displays three peaks at 530.1, 531.9 and 532.3 eV corresponding to oxygen being present in three different environments: P-O, -C-O and Fe-O. The peak for P 2p binding energies appeared in a broad range from 130-141 eV and could be fitted into two peaks at 132.3 eV and 133.7 eV, corresponding to P $2p_{3/2}$ and $P2p_{1/2}$ respectively. The Fe2p doublet with binding energy values of 710 and 725 eV implies the presence of Fe-O bonds, typical for magnetite [28]. The unaltered Fe2p spectrum, following FA immobilization gives a clear proof that surface modification has no deleterious effect on the composition of the support material. In addition to surface chemistry analysis, investigation of the chemical composition of the nanoparticle surface was also carried out by XPS. The apparent surface compositions of functionalized nanoparticles and their folate-conjugated counterparts (reported in **Table 2.2**) shows a significant increment in nitrogen content of 2.1-2.3 as compared to their non-folate-conjugated counterparts **1.1-1.3** (without fluorescent label), corroborating to the successful functionalization of Fe_3O_4 with folic acid.

Table 2.2: Surface elemental composition determined via XPS

Nanoparticles	Surface elemental compositions (a %)				
	Fe	O	C	P	N
1.1	2.9	21.1	74.3	0.9	0.8
1.2	2.1	25.2	71.1	0.9	0.7
2.1	1.3	16.7	76.9	0.8	4.3
2.2	1.2	16.9	74.8	0.9	6.2
2.3	1.2	15.8	76.4	0.8	5.8

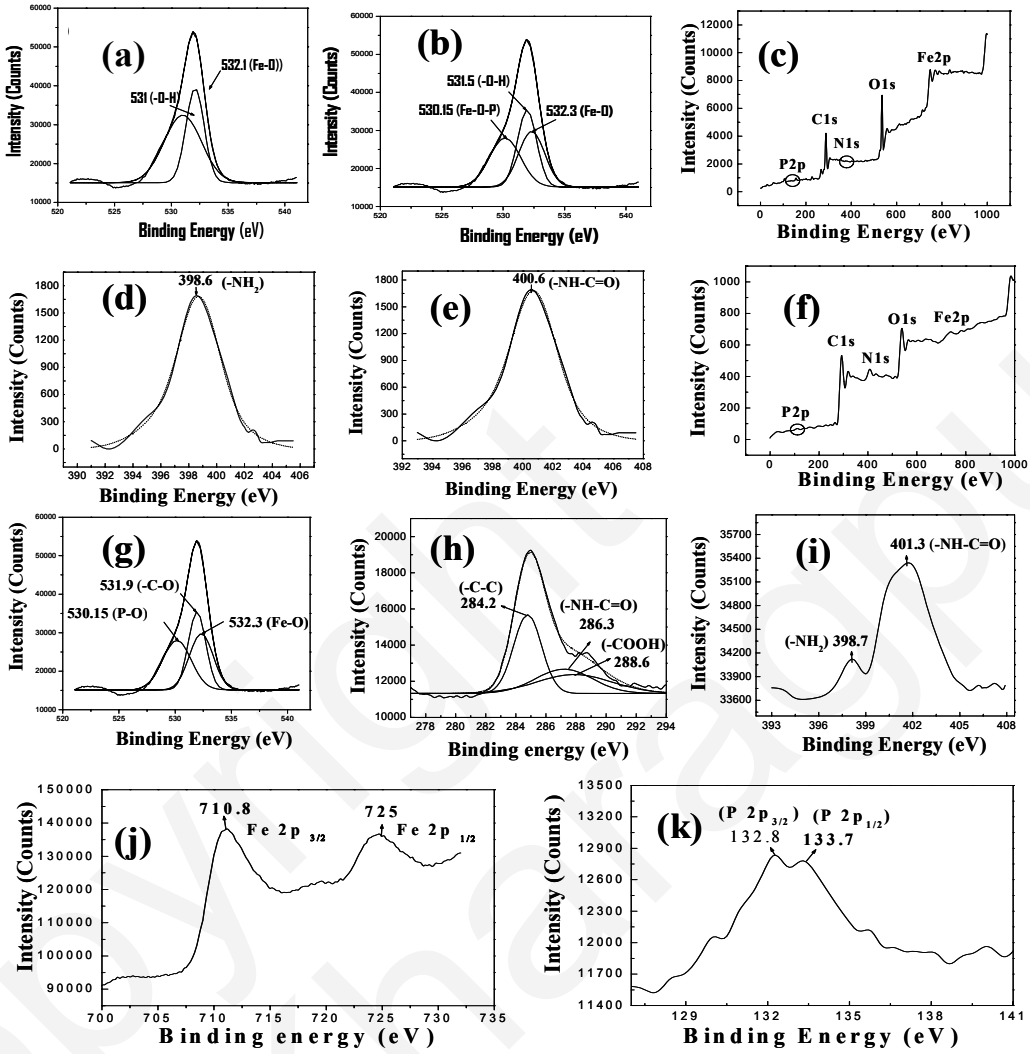

Fig. 2.5: (a) The high resolution O1s spectrum of bare magnetite nanoparticles **(b)** O 1s spectrum of Fe_3O_4-APA **(c)** Survey spectrum of Fe_3O_4-APA (**1.1**) **(d)** N 1s spectrum of Fe_3O_4-APA **(e)** N 1s spectrum after modification of **1.1** with succinic anhydride (**1.2**) **(f)** Survey scan of Fe_3O_4-APA-FA **(g)-(k)** C1s, O1s, N1s, Fe2p and P2p spectra of Fe_3O_4-APA-FA **(2.1).**

To study the influence of surface modification on the magnetic behaviour of nanoparticles, magnetization measurements were performed using vibration sample magnetometry (VSM). **Figure 2.6** presents the magnetization curve for **1.1**, which displayed no hysteresis and was completely reversible at 300 K. Neither coercivity nor remenance was observed, corroborating to the superparamagnetic nature of the as-prepared samples. The saturation magnetization (M_s) was found to be ~ 70 emu/ gm, which was lower in comparison to that of

uncoated magnetite. Following conjugation with FA, a further loss in magnetization (M_s) is observed, which can be ascribed to the introduction of a nonmagnetic mass on the surface of iron-oxide nanoparticles.

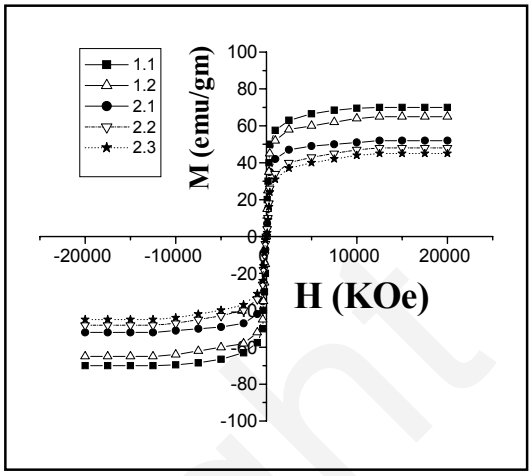

Fig. 2.6: Magnetization (**M-H**) curve of folate-functionalized and non-functionalized MNPs at 300 K

The findings of VSM were further compared with the results of thermo-gravimetric analysis (TGA). The magnetic content of iron-oxide nanoparticles composed of a magnetic core surrounded by an organic corona can be calculated from the percentage of organic coating associated with the core material. Thus, magnetic content of **1.1** was calculated to be around 78%, which supports the presence of a well-defined monolayer of ligands on the nanoparticle surface. The M_s values could also be estimated on the basis of TGA data via the following formula:

$$M_s = M_s^{Fe_3O_4}(1-\omega)$$

where M_s^{Fe3O4} is the theoretical saturation magnetization of Fe_3O_4 nanoparticles (92emu/gm) and ω is the mass loss (%), determined via TGA. The M_s values of different nanoparticle preparations calculated via TGA correlates well with those determined from VSM (Table **2. 3**). It should however be noted that the loss in magnetizations obtained for the different nanoparticle preparations are significantly lower than those obtained in case of polymeric or silane modifications. The application of a silane coating leads to a considerable decrease in magnetic content per particle; in some cases the loss is even higher than 75% due to the formation of a polymerized multilayer of silane ligands [29]. In our system, by applying a phosphonate coating, which is restricted to monolayer formation, the magnetic content of the core is always higher than 50%, ensuring better response of the nanoparticles towards an external magnetic field.

Table 2. 3: Magnetization measurements from VSM and TGA

Nanoparticles	M_s (emu/g particles) from VSM	M_s (emu/g particle) from TGA		
		Weight loss (ω %)	Magnetic content (%)	$Ms = M_s^{Fe3O4}$ (1-ω)
1.1	70.2	21.8	78.2	71.94
1.2	65.4	25.3	74.7	68.72
1.3	52.3	42.6	57.4	52.8
1.4	48.6	45.4	54.6	50.23
1.5	45.1	48.3	51.7	47.56

Bare magnetite nanoparticles are nearly devoid of charge (+ 5 mV) and flocculates in neutral biological media. Surface modification of these pristine nanoparticles was accompanied by change of surface charge, which was confirmed by zeta potential analysis and change to both particle size and polydispersity (PD) (**Table 2. 4**).

Table 2.4: Hydrodynamic ((HD) size, PDI and zeta potential of the folate-functionalized (**2.1-2.3**) and non-functionalized nanoparticles (**1.1-1.3**) at physiological pH.

Nanoparticles (before FA conjugation)	Size (nm)	PDI	Zeta Potential (mV)	Nanoparticles (after FA conjugation)	Size (nm)	PDI	Zeta Potential (mV)
1.1	32	0.169	+25.2	2.1	41	0.188	-42.3
1.2	34	0.184	-36.6	2.2	43	0.191	-49.4
1.3	42	0.218	-4.4	2.3	46	0.192	-38.7

The zeta potential of the magnetite surface changes from near neutral to positive (25.2 eV) through APA modification. The amino functions imparted high positive charge, particularly over the lower pH range due to the presence of surface-exposed NH_3^+ groups. These APA functionalized nanoparticles (**1.1**) presented a mean hydrodynamic diameter of 32 nm with a polydispersity index (PDI) less than 0.2. A little or practically no difference in HD was observed after modification of the amine terminal with succinic anhydride but the zeta potential, as anticipated, changed from positive to negative value (-36.6 mV) due to the presence of carboxylate ($-COO^-$) functions on the nanoparticle surface. Following conjugation with FA, a slight increase in HD was observed. The iron-oxide folate nano-conjugates (**2.1-2.3**) presented a mean diameter between 40-45 nm with a polydispersity index (PDI) less than 0.2. The zeta potential got increasingly negative with rising pH, which is probably because of the progressive deprotonation of the FA carboxylic groups. The variation

of hydrodynamic size, PDI and zeta potential of the iron-oxide folate conjugate **2.1** (Fe_3O_4-APA-FA) in function of pH and time has been presented in figure **2.7**. pH or ionic strength did not significantly influence the mean size or PDI of nanoparticles. Similar trend was observed for the nanoparticle designs **2.2** and **2.3** (results not shown). The nanoparticles were highly stable in aqueous dispersion under physiologically tolerable conditions; no significant deterioration in particle size was observed even after six months from their date of preparation. Fabrication of nanoparticles with long-term colloidal stability is a key step towards the design of long circulating magnetic nanoparticles.

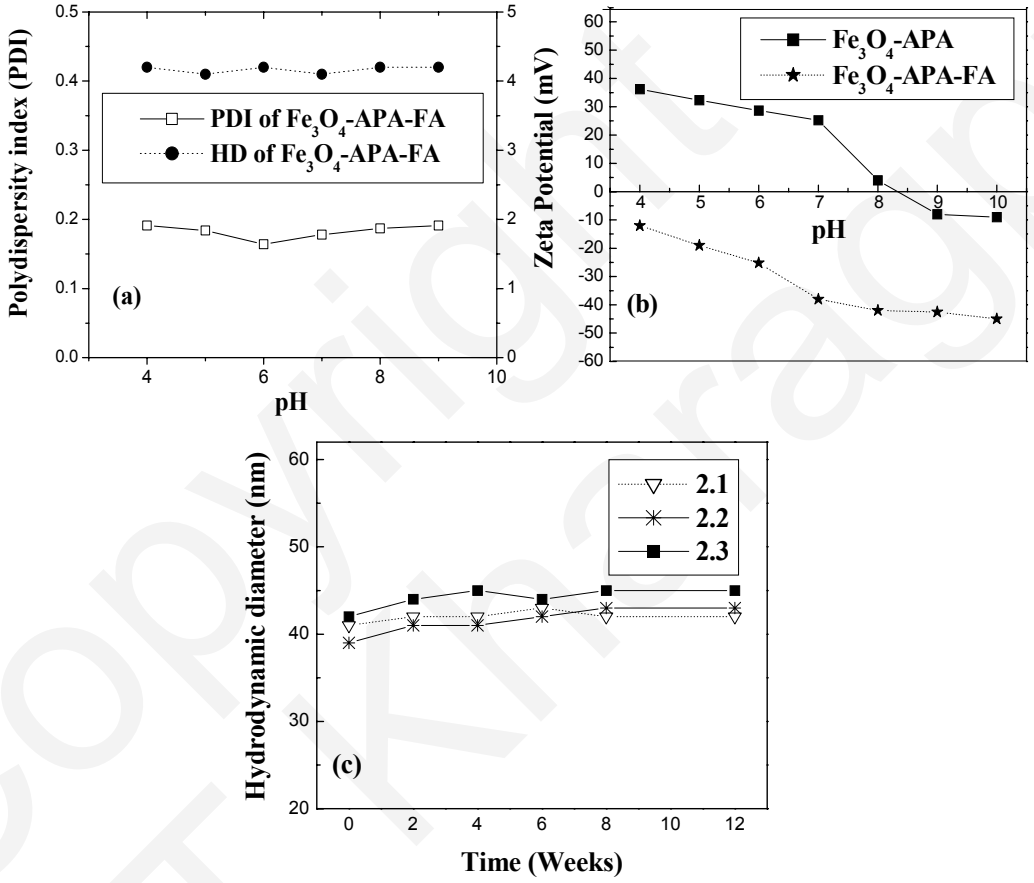

Fig. 2.7: Variation of **(a**) particle size and PDI of Fe_3O_4-APA-FA (**2.1**) against pH **(b)** zeta potential of Fe_3O_4-APA and Fe_3O_4-APA-FA against pH **(c)** particle size of **2.1-2.3** against time.

To further evaluate, whether these functional nanoparticles as well as their folate-decorated counterparts could be used as a biocompatible material for diagnostic or therapeutic applications, an MTT assay was performed on human cervical HeLa cancer cell line. Cells were incubated with various concentrations of the nanoparticles upto 200 µg/ ml of

nanoparticles. After 4 h of incubation, no significant reduction in cellular viability was observed. The survival rate was higher than 90%, even at the higher nanoparticle concentrations (**Fig. 2. 8**). Little or practically no difference was shown between the cytotoxicities of the targeted and nontargeted particles.

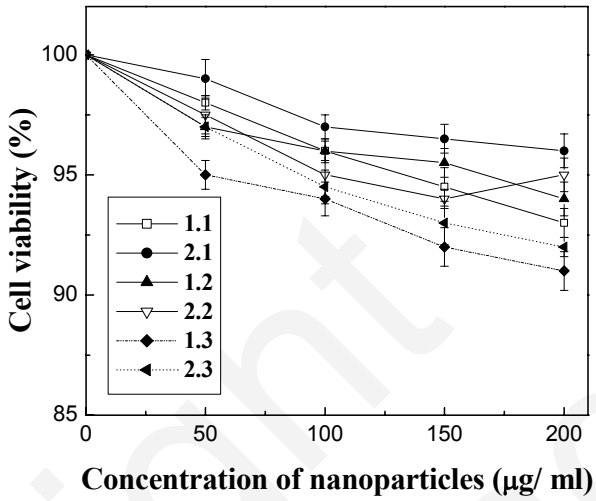

Fig. 2.8: Effect of folate-conjugated nanoparticles (**2.1-2.3**) and their non-targeted counterparts (**1.1-1.3**) on the viability of HeLa cells. Cells incubated with different nanoparticles preparations for 4 h at 37°C followed by viability assay by MTT method. No significant reduction in cellular viability was observed, the survival rate being higher than 90%, even at the highest nanoparticle concentration.

In-vitro cellular uptake experiments were performed using human cervical carcinoma HeLa cells, known to significantly over-express the folate receptor [30-31]. To investigate the role of FA as targeting agent and the effectiveness of our surface design on the internalization of iron-oxide nanoparticles by target cells, folate-receptor positive HeLa cells were incubated with both targeted as well as the non-targeted nanoparticles, serving as controls. Cell uptake behavior of the nanoparticles was studied using magnetically activated cell sorting (MACS), fluorescence microscopy and confocal laser scanning microscopy (CLSM) analysis. As evident from MACS based quantification [results displayed in **Fig. 2. 10 (a)**], the folate-linked nanoparticles (**2.1-2.3**) showed significantly higher uptake in comparison to their nontargeted counterparts (**1.1-1.3**).

Receptor-mediated internalization of nanoparticles by FAR over-expressing cancer cells was further demonstrated using fluorescence and CLSM analysis respectively. Preliminary studies using the fluorescence microscopic technique demonstrated the selective accumulation of **2.1-2.3** in FR over-expressing HeLa cells, as compared to their non-targeted control **1.1-1.3**. For a

better understanding of the intracellular distribution of the folate-functionalized nanoparticles inside the target cells, confocal image of HeLa cells incubated with **2.1-2. 2** (presented in **Fig. 2.9**) were recorded. As predicted from the cytotoxicity experiments, confocal images clearly showed that structures of MNP-internalized cells were well preserved without any visible abnormalities. The folate conjugated nanoparticles were found to be distributed within the cytoplasm, leaving a clear zone of nucleus, suggesting cellular internalization through receptor mediated endocytosis, instead of adhesion to the cell-surface. This study unequivocally establishes that all the iron-oxide folate nano-conjugates, developed in course of our research are preferentially targeted towards cancer cells and effectively internalized.

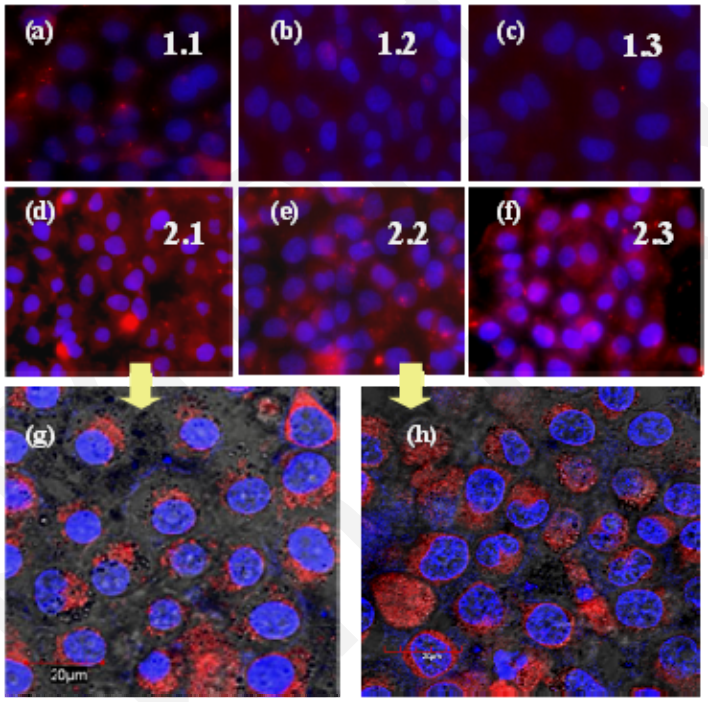

Fig. 2. 9 Nanoparticle uptake visualized by fluorescence and confocal microscopy **(a-f)** Fluorescence image of HeLa cells incubated with iron-oxide folate nanoconjugates (**2.1-2.3**) and their non-targeted counterpart as well. (**g-h**) represents the confocal image of HeLa cells incubated with **2.1** and **2.2** respectively.

To further evaluate the specificity of cellular targeting of the nanoparticle conjugates, the uptake of iron-oxide folate conjugates **2. 1-2. 3** by HeLa cells was compared with the uptake by MG-63 cells, a folate receptor negative cell-line, expressing very low levels of both α and ß forms of the folate receptor [32]. The targeting efficacy of the folate nanoparticles can be expressed in terms of specific uptake index (SUI), calculated as the ratio between the number

of folate-targeted particles taken up by the cells and the number of non-targeted particles, taken up under the same conditions (i.e. non-specific uptake). In the case of folate receptor over-expressing HeLa cells, nanoparticle uptake was much greater for the targeted particles as compared to their non-targeted counterparts with appreciably high SUI values. On the contrary, MG-63 cell uptake level of folate-targeted nanoparticles was considerably low and similar to those of the non-targeted controls [**Fig. 2.10 (b-c)**], the S.U.I being nearly equal to or slightly greater than 1.

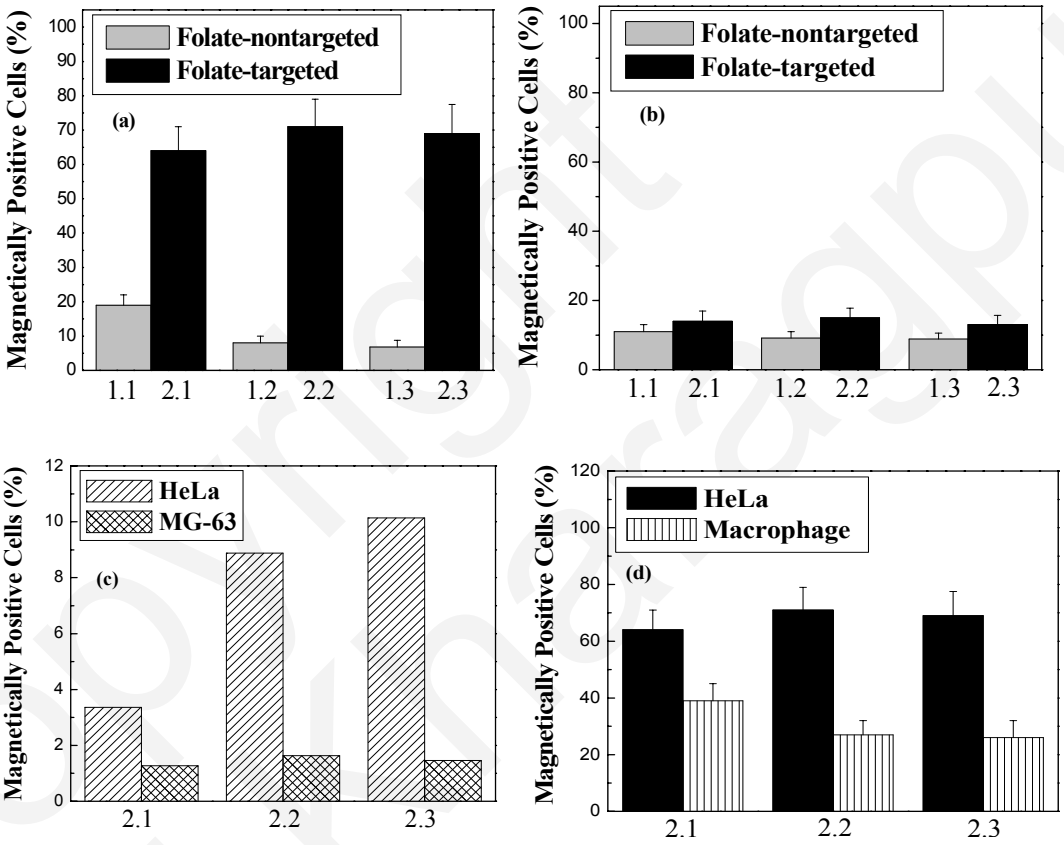

Fig 2.10 Intracellular uptake behavior of **(a)** folate-targeted vs. non-targeted particles in HeLa cells **(b)** folate-targeted vs. nontargeted particles in MG-63 cell line **(c)** Specific uptake index (S.U.I.) of 2.1-2.3 in HeLa and MG-63 cells and **(d)** phagocytosis of nanoparticles by macrophage *in vitro*.

To further ensure that our designed MNPs were stealth enough to avoid clearance by reticuloendothelial system (RES) and targeted into the desired pathological zone, the phagocytic uptake of iron-oxide folate nanoconjugates (**2.1-2.3**) by peritoneal macrophages was studied *in-vitro* and compared with the folate-receptor positive HeLa cells. It was observed that phagocytosis of the folate-targeted nanoparticles by peritoneal macrophages was appreciably low, as compared to the uptake by HeLa cells [**Fig. 2.10(d)**]. The uptake-

level was even lower in cases, where EDBE modification was used. It should however be noted that with the present size and surface-chemistry of nanoparticles, the phagocytosis by macrophages will be low as compared to folate-receptor mediated endocytosis by cancer cells. The present finding is also consistent with an earlier report on the phagocytosis of PEG modified nanoparticles [4].

To further clarify whether inclusion of EDBE as a hydrophilic spacer on the nanoparticle surface had any synergetic effect on increasing the accessibility of the attached ligands to target receptor, a model study was performed. The EDBE spacer in **2.2** as well as **2.3** was replaced by a relatively hydrophobic spacer hexamethylene diammine (HMDA), lacking the mini-PEG backbone in its structure. *In-vitro* cell-uptake of both types of conjugates (SPION-FA-EDBE vs. SPION-FA-HMDA) was studied against the HeLa cell line. Interestingly, the cell-uptake level of the conjugates, synthesized with EDBE-linker was observed to be higher in comparison to those synthesized using HMDA as linker (**Fig. 2.11**). The results are however consistent with the earlier literature reports [27].

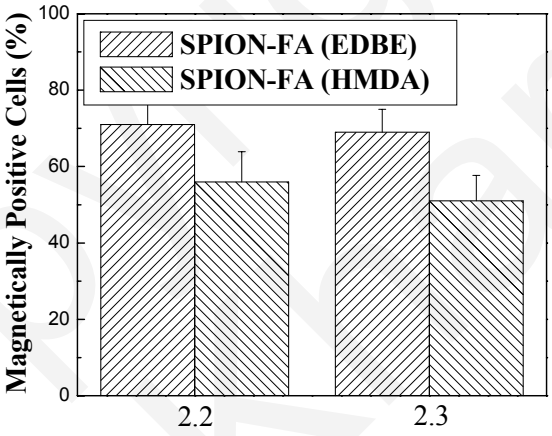

Fig. 2.11: Uptake of SPION-FA (EDBE) vs. SPION-FA (HMDA) by HeLa cells: Effect of EDBE modification on the stability and intracellular uptake of nanoparticles.

2.4 Conclusions

In conclusion, hydrophilic, biocompatible magnetite nanoparticles with surface-pendant amine and carboxyl groups have been developed using a seldom-used aminophosphonic acid as the surface coupling agent. Magnetofluorescent iron-oxide nanoparticles were synthesized

by covalent immobilization of rhodamine isothiocyanate (RITC) on the surface of 2-aminoethyl phosphonic acid. The amine functions on the surface were interchanged with carboxyl and aldehyde functions via a ring-opening linker elongation reaction of the amine-terminated nanoparticles with succinic anhydride and glutaraldehyde treatment respectively. To further demonstrate the effectiveness of ligand immobilization, folic acid (FA), a widely used targeting agent was immobilized onto the magnetofluorescent support, utilizing diverse conjugation strategies. Both folate-functionalized nanoparticles as well as their non-functionalized counterparts were extensively characterized in terms of size, charge, surface-chemistry, composition and magnetic properties. The magnetite-nanoparticle-folate conjugates showed excellent aqueous dispersion stability with reasonably good hydrodynamic size over a wide range of physiological conditions. The presence of a mini-PEG spacer between FA and magnetite nanoparticles resulted in reduced uptake of the conjugated nanoparticles by peritoneal macrophages *in vitro* as compared to folate-receptor (FR) over-expressing cancer cells. Magnetically activated cell sorting (MACS) and confocal microscopy, performed with FR positive HeLa cell line clearly established the targeting efficiencies as well as receptor-mediated internalization of these non-cytotoxic iron-oxide-folate nano-conjugates against FR over-expressing cancer cells. In a scientific panorama, in which folate–mediated tumor targeting seems to be one of the major break-through in cancer diagnosis, the unique bio-functionalization approach presented throughout the chapter supplements a new tool-box in the design and synthesis of stealth and targeted MNPs for theragnostic applications.

References:

1. Knauth, M.; Egelhof, T.; Roth, S.U.; Wirtz, C. R.; Sartor, K. Monocrystalline iron oxide nanoparticles: possible solution to the problem of surgically induced intracranial contrast enhancement in intraoperative MR imaging. *Am. J. Neuroradiol* **2001**, *22*, 99-102.

2. Lacava, L. M.; Lacava, Z. G.; Da Silva, M. F.; Silva, O.; Chaves, S. B. Azevedo, R. B.; Peregrine, F.; Gansau, C.; Buske, N.; Sabolovic, D.; Morais, P.C. Magnetic resonance of a dextran-coated magnetic fluid intravenously administered in mice. *Biophys. J.* **2001,** *80*, 2483-2486.

3. Weissleder, R.; Bogdanov, A.; Neuwelt, E. A.; Papisov, M. Long-circulating iron oxides for MR imaging *Adv. Drug Delivery Rev* **1995,** *16*, 321–334.

4. Zhang, Y.; Kohler, N.; Zhang, M. Surface modification of superparamagnetic magnetite nanoparticle and their intracellular uptake, *Biomaterials* **2002**, *23,* 1553–1561.

5. Gupta, P. K.; Hung, C. T. Minireview: Magnetically controlled targeted micro-carrier systems *Life Sci.* **1989**, *44***,** 175–186.

6. Kohler, N.; Sun, C.; Wang, J.; Zhang, M. Methotrexate-Modified Superparamagnetic Nanoparticles and Their Intracellular Uptake into Human Cancer Cells *Langmuir* **2005,** *21***,** 8858-8864.

7. Marchal, G.; Van Hecke, P.; Demaerel, P.; Decrop, E.; Kennis, C.; Baert, A.L.; van der Schueren, E. Detection of liver metastases with superparamagnetic iron oxide in 15 patients: results of MR imaging at 1.5 T *Am J Roentgen* **1989**, *152*, 771–775.

8. Lubbe, A. S, Bergemann, C.; Riess, H.; Schriever, F.; Reichardt, P.; Possinger, K.; Matthias, M.; Dorken, B.; Herrmann, F.; Gurtler, R.; Hohenberger, P.; Haas, N.; Sohr, R.; Sander, B.; Lemke, A. J.; Ohlendorf, D.; Huhnt, W.; Huhn, D. Clinical experiences with magnetic drug targeting: a phase I study with 4′-epidoxorubicin in 14 patients with advanced solid tumors *Cancer Res* **1996,** *56*, 4686–93.

9. Chouly, C.; Pouliquen, D.; Lucet, L.; Jeune, J. J.; Jallet, P. Development of superparamagnetic nanoparticles for MRI: effect of particle size, charge and surface nature on biodistribution *J. Microencapsulation* **1996**, *13***,** 245–255.

10. Stolnik, S.; Illum, L.; Davis, S. S. Long circulating microparticulate drug carriers *Adv. Drug Delivery Rev.* **1995**, *16*, 195–214.

11. Allemann, E.; Gurny, R.; Doelker, E. Drug loaded nanoparticles - Preparation methods and drug targeting issues. *Eur. J. Pharmacol. Biopharm.* **1993,** *39*, 173-191

12. Gupta, A.K.; Wells, S. Surface-modified superparamagnetic nanoparticles for drug delivery: preparation, characterization, and cytotoxicity studies *IEEE Transactions On Nanobioscience* **2004,** *3***,** 66-73

13. Zhang, M.; Ferrari, M. Hemocompatible Polyethylene Glycol Films on Silicon *Biomed. Microdev.* **1998**, *1*, 81-89

14. Golander, C. G.; Herron, J. N.; Lim, K.; Claesson, P.; Andrade, J. D.; Harris, J. M. *Biomedical Applications of Polyethylene Glycol Chemistry* (New York: Plenum) **1992**, 221-245

15. Sonvico F, Mornet S, Vasseur S, Dubernet C, Jaillard D, Degrouard J, Hoebeke J, Duguet E, Colombo P and Couvreur P Folate-Conjugated Iron Oxide Nanoparticles for Solid Tumor Targeting as Potential Specific Magnetic Hyperthermia Mediators: Synthesis, Physicochemical Characterization, and in Vitro Experiments *Bioconjug. Chem.* **2005**, *16***,** 1181

16. Strable, E.; Bulte, J. W. M.; Moskowitz, B.; Vivekanandan, K.; Allen, M.; Douglas, T.; Synthesis and Characterization of Soluble Iron Oxide−Dendrimer Composites *Chem. Mater.* **2001**, *13*, 2201-2209

17. Smaihi, M.; Gavilan, E.; Durand, J.; Valentin, P. Valtchev Colloidal functionalized calcined zeolite nanocrystals *J Mater. Chem*. **2004**, 14, 1347-1351

18. Mutin, H. P.; Guerrero, G.; Vioux, A. *Hybrid materials from organophosphorus coupling molecules J Mater. Chem*. **2005**, *15***,** 3761-3768

19. Adden, N.; Gamble, L. J.; Castner, D. G.; Hoffmann, A.; Gross, G.; Menzel, H.; Phosphonic Acid Monolayers for Binding of Bioactive Molecules to Titanium Surfaces. *Langmuir* **2006**, *22***,** 8197-8204

20. Neouze, M. A.; Schubert, U. Surface Modification and Functionalization of Metal and Metal Oxide Nanoparticles by Organic Ligands *Monatsh Chem.* **2008***, 139,* 183–195

21. Kosolapoff, G. The Synthesis of Amino-substituted Phosphonic Acids. I *J. Am. Chem. Soc***. 1947**, *69*, 2112-2113

22. Mohapatra, S.; Mallick, S. K.; Maiti, T. K.; Ghosh, S. K.; Pramanik, P. Synthesis of highly stable folic acid conjugated magnetite nanoparticles for targeting cancer cells *Nanotechnology* **2007**, *18***,** 385102

23. Levy, E. F.; Andry, M.C.; Levy M. C., Determination of free amino group content of serum albumin microcapsules using trinitrobenzenesulfonic acid: effect of variations in polycondensation pH *Int. J. Pharm.* **1993**, *96*, 85-90

24. Tourinho, F. A.; Franck, R.; Massart, R. Synthesis and magnetic properties of managanese and cobalt ferrite ferrofluids *Prog. Colloid Polym. Sci.* **1989,** *29*, 128-134

25. Wang, S.; Luo, J.; Lantrip, D. A.; Waters, D. J.; Mathias, C. J.; Green, M. A.; Fuchs, P.; Low, P. S. *Bioconjugate Chem*. **1997**, *8***,** 673-679

26. Gabizon, A.; Horowitz, A. T.; Goren, D.; Tzemach, D.; Mandelbaum-Shavit, F.; Qazen, M. M.; Zalipsky, S. Design and Synthesis of [^{111}In] DTPA−Folate for Use as a Tumor-Targeted Radiopharmaceutical, *Bioconjugate Chem*. 1999, **10,** 289

27. Schneider, R.; Schmitt, F.; Frochot, C.; Fort, Y.; Lourette, N.; Guillemin, F.; Muller, J.; Barberi-Heyob, M. Design, synthesis, and biological evaluation of folic acid targeted tetraphenylporphyrin as novel photosensitizers for selective photodynamic therapy. *Bioorg. Med. Chem.* **2005**, *13***,** 2799

28. Liana, S.; Kanga, Z.; Wanga, E.; Jianga, M.; Hua, C.; Xua, L. Convenient synthesis of single crystalline magnetic Fe_3O_4 nanorods *Solid State Commun.* **2003**, *127*, 605

29. De Palma R.; Sara, P.; Margriet, J. V. B.; Heidi, V. R.; Kristien, B.; Wim, L.; Jules, M.; Gustaaf, B.; Maes G Silane Ligand Exchange to Make Hydrophobic Superparamagnetic Nanoparticles Water-Dispersible *Chem. Mater.* **2007**, *19***,** 1821-1831

30. Zheng, X.; Kelley, K.; Elnakat, H.; Yan, W.; Dorn, T.; Ratnam, M. mRNA Instability in the Nucleus Due to a Novel Open Reading Frame Element Is a Major Determinant of the Narrow Tissue Specificity of Folate Receptor α Mol *Cell Biol.* **2003**, *23*, 2202-2212

31. Saul, J. M.; Annapragada, A.; Natarajan, J. V.; Bellamkonda, R. V. *J. Control. Release* **2003,** *92***,** 49-67

32. Ross, J. F.; Chaudhuri, P. K.; Ratnam, M. Controlled targeting of liposomal doxorubicin via the folate receptor in vitro *Cancer* **1994,** *73***,** 2432-2443

Chapter 3

Biofunctionalized, Phosphonate-grafted Ultrasmall Iron-Oxide Nanoparticles for Combined Targeted Cancer Therapy and Multimodal Imaging

3. 1. Introduction

Over the last few years, there has been a phenomenal impetus in the design and development of nanometer-sized targeted probes for cancer diagnosis and therapy [1-3]. Intelligent combinations of different nanostructured materials prop up the development of "smart" multifunctional nanoplatforms [4-6], which depending upon reticular requirements can be appropriately engineered to demonstrate a combination of eclectic properties or functions such as **(i)** longevity in blood circulation **(ii)** active or passive targeting into the desired pathological zone **(iii)** responsiveness to local physiological stimuli such as pathology associated changes in pH, temperature or ionic strength which for e.g. may lead to accelerated drug release **(iv)** an effective intracellular drug delivery and release mechanism and **(v)** ability to serve as a multimodal imaging probe for effective molecular imaging. Among the various types of functional nanostructures, which have surged interest for biomedical applications, superparamagnetic iron-oxide nanoparticles with a magnetite or maghemite core have been realized as the most popular multifunctional materials for their potential biomedical applications, which have already been discussed in **Chapter 1**. These nanoparticles can be decorated with multiple diagnostic and therapeutic entities to play the dual role of targeting contrasts and drug carriers simultaneously, allowing a real time monitoring of the tumor response to drug delivery and treatment.

Despite their strong affinity towards the iron-oxide core [7-8], organophosphorous coupling agents (OPCA) have been seldom investigated for tailoring the surface of magnetic nanoparticles with functional ligands. In the previous chapter, it has been shown that the use of bifunctional phosphonic acids with polar end groups such as amine or carboxyl not only render the MNPs hydrophilic and stable with respect to aggregation, but also imparts functionality on the surface to provide facile access to bioconjugates. In addition, the P-C bond system in phosphonic acids have low toxicity, appreciable thermostability and are highly resistant to enzymatic cleavage [9]. Hence, surface bio-engineering of nanomaterials involving phosphonic acid coupling agents appears to be highly promising and motivates us to re-exploit this strategy to design and fabricate multifunctional nanoplatforms for theragnostic applications.

In this chapter, we attempt to synthesize a new type of multifunctional, theragnostic iron-oxide nanoformulation for combined cancer targeted magnetic resonance/ optical imaging and therapy, using N-phosphonomethyl iminodicaetic acid (PMIDA) modified ultrasmall superparamagnetic magnetite nanoparticles as the bio-conjugating precursor. This platform is composed of four components. Firstly, the PMIDA coated magnetite nanoparticles (USPIO-PMIDA, **1**) served as the core material to allow magnetically guided drug delivery as well as T_2 weighted MR contrast enhancement. Secondly, a fluorescent dye, rhodamine B isothiocyanate (RITC), was coupled to the amine-derivated USPIO-PMIDA support (**3.1**) to facilitate optical imaging capabilities. Thirdly, cancer–targeting folate (FA) was conjugated to **3.1** to target the folate receptor (FR) over-expressed cancer cells. Finally, the folate antagonist methotrexate (MTX) was coupled to the nanoparticle surface through a pH-labile ester linkage to abet drug release inside the acidic tumor endosomes and initiate apoptosis. To the best of our knowledge, no previous reports have embarked on such systematic development of a biocompatible, multimodal and theragnostic functional iron-oxide nanoformulation, using phosphonate grafted USPIONs as the precursor. The simple, water-based synthesis process is cost-effective, amenable to scale up and contributes a new tool-box for the non-polymer based bio-functionalization of inorganic nanoparticles, circumventing a large number of problems associated with polymer-based modifications that has already been discussed in the previous chapters.

3. 2. Materials and Methods

3.2.1 Materials

$FeCl_3$ and $FeSO_4$ were obtained from Merck, Germany, as already mentioned in **Chapter 2.** N-phosphonomethyl iminodiacetic acid, Folic acid (FA), dicyclohexyl carbodiimide (DCC), *N*-hydroxysuccinimide (NHS), 1-[3-(Dimethylamino) propyl]-3-ethylcarbodiimide hydrochloride (EDC), 2,2-(ethylenedioxy)-bis-(ethylamine) (EDBE), glycidol, rhodamine isothiocyanate (RITC), MTT [3-(4,5-dimethylthiazol-2-yl)-2,5-diphenyltetrazolium], Propidium iodide, (PI) RNase A, Trypsin, 4′,6-diamidino-2-phenylindole dihydrochloride (DAPI), agarose were purchased from Sigma Chemical Co. (St. Louis, MO, USA). Methotrexate was obtained as a gift from Ranbaxy pharmaceuticals. Commercially available dimethyl sulphoxide (DMSO) and ethanol (C_2H_5OH) were distilled prior to use.

3.2.2 Synthesis Methodology

3.2.2.1 Synthesis of USPIO-PMIDA (3.1)

Ultrasmall, superparamagnetic magnetite nanoparticles with surface-pendant carboxyl groups were prepared by alkali-mediated chemical co-precipitation of Fe^{2+} and Fe^{3+} (to be taken in 1:2 ratio) in the presence of N-phosphonomethyl iminodiacetic acid. In a typical experiment, $FeCl_2.4H_2O$ (1 mmol) and $FeCl_3$ (2 mmol) were dissolved in 10 ml of de-ionized, de-oxygenated water. After addition of 0.5 mmol of PMIDA to the resultant mixture, the solution was vigorously stirred and heated to 35-40 $^{\circ}$C under an argon atmosphere. Subsequently about 5 ml of 32% ammonia solution was injected into the flask and stirring was continued for another 20 min to allow the growth of the nanoparticles. The solution was then cooled to room temperature and the resulting particles were isolated as usual through magnetic decantation followed by repeated washing.

3.2.2.2 Synthesis of USPIO-PMIDA-EDBE (3.1.1)

To interchange the carboxyl functions on USPIOs with amine functions, an aqueous colloidal suspension of USPIO-PMIDA was activated with EDC. The pH of the resultant mixture was adjusted to 8 by the addition of 0.1(M) NaOH, 0.5 ml of 2, 2-(ethylenedioxy)-bis-(ethylamine) (EDBE) was added to the resulting suspension, which was then subjected to overnight stirring. The aminated product USPIO-PMIDA-EDBE was finally recovered through magnetic concentration, followed by repeated washing with de-ionized water, as usual.

3.2.2.3 Synthesis of USPIO-PMIDA-EDBE-RITC (3.1.2)

1 mg of rhodamine isothiocyanate (RITC) was dissolved in 1ml of DMSO-H_2O mixture and added dropwise to an aqueous suspension of 25 mg of **3.1.1** at pH ~ 8. The resulting suspension was sonicated in the dark for an hour. Particles were recovered by magnetic concentration and washed thoroughly with de-ionized water.

3.2.2.4 Synthesis of USPIO-PMIDA-EDBE-RITC (3.1.3)

To conjugate USPIO-PMIDA-EDBE-RITC with folic acid, FA (0.05 mmol) was dissolved in ~10 ml of DMSO. The resulting solution was then mixed with an aqueous solution of 1-ethyl-3-(3-dimethylamino)-propyl) carbodiimide (EDC) (75 mmol) and *N*-hydroxy succinimide (NHS) (15 mmol). The pH of the reaction medium was adjusted to 8 by dropwise addition of 0.01 (M) NaOH solution, following which, an aqueous dispersion of around 20 mg of the aminated MNPs was added and the reaction mixture was allowed to stir overnight at 37°C in the dark. Following FA conjugation, the modified particles were again isolated with a rare earth magnet, washed 5 times with de-ionized water and re-dispersed in PBS.

3.2.2.5 Synthesis of USPIO-PMIDA-EDBE-RITC-FA-OH (3.1.4)

The conjugation of glycidol to **3.1.3** was a necessary precursory step in order to attach MTX to the nanoparticle surface via a pH-labile ester linkage. An ethanolic solution of glycidol (10 ml, 1% v/v) was added dropwise to an ultrasonicated colloidal suspension of **3.1.3** (15 mg dispersed in ~10 ml of ethanol) and stirred for 24 h. Nanoparticle isolation was done, as described earlier.

3.2.2.6 Synthesis of USPIO-PMIDA-EDBE-RITC-FA-OH-MTX (3.1.5)

To conjugate USPIO-PMIDA-EDBE-RITC-FA-OH with methotrexate (MTX), MTX (0.025 mmol) was dissolved in minimum amount of DMSO and diluted with 10 ml of water. The resulting solution was then mixed with an aqueous solution of 1-ethyl-3-(3-dimethylamino)-propyl) carbodiimide (EDC) (75 mmol) and *N*-hydroxy succinimide (NHS) (15 mmol). The pH of the solution was adjusted to around 8 by dropwise addition of NaOH. An aqueous dispersion of the glycidylated nanoparticles (10 mg dispersed in about 10 ml of water) was added to it and the reaction mixture was stirred overnight at 37°C in the dark. MTX conjugated nanoparticles were isolated, as described earlier.

3.2.3. Characterizations

The phase analysis of the synthesized magnetite nanopowder was performed on an PW 1729 X-ray diffractometer (Philips, Holland). High-resolution transmission electron microscopy performed with a Phillips CM 200 transmission electron microscope was employed to characterize the microstructure of the as-prepared USPIONs. The hydrodynamic (HD) size of the particle aggregates was measured by laser light scattering using a Brookhaven 90 Plus particle size analyzer after dilution of the sample to 150 µg/ mL iron oxide concentration. The surface charge of the nanoparticles was investigated through zeta potential measurements (Zetasizer 4, Malvern Instruments, UK), according to the procedure described in the previous chapter. Surface chemistry of the nanoparticles was studied using a Thermo Nicolet Nexux FTIR model 870 spectrometer. The surface compositions of the different nanoparticle preparations were obtained by analyzing X-ray Photoelectron Spectroscopic (XPS) data using Al K_α excitation source in an ESCA-2000 Multilab apparatus (VG microtech). Magnetic measurements were performed using a vibration sample magnetometer. Samples for magnetorelaxometric studies were prepared by mixing 1 ml of aqueous dispersions of various concentrations (0-100 µmol Fe) of the as-prepared USPIONs with 0.5 ml of low melting 1% agarose gel.

3.2.4. Total iron determination and quantification of different functional molecules immobilized on USPIOs

3.2.4.1. Spectrophotometric determination of iron content in nanoparticles

For total iron determination, the iron present in the nanoparticles was completely extracted by dissolving the nanoparticles (10 mg in 10 ml of 30% v/v HCl) for 2 h at 50–60°C. To the resultant mixture, a total of 1.0 mg of ammonium persulphate was added to oxidise the ferrous ions present in the above solution to ferric ions. 1 ml of potassium thiocyanate (0.1 mol) was added to this solution to initiate the formation of the blood red iron-thiocyante complex.

$$Fe_{(aq)}^{3+} + 6\,SCN_{(aq)}^{-} \rightarrow [Fe(SCN)_6]_{(aq)}^{3-}. \qquad \textbf{Eq. 3.1}$$

Iron concentration was determined spectrophotometrically by recording the absorbance at 478 nm, using a Shimadzu UV-1700 spectrophotometer.

3.2.4.2. Quantification of amine density on the nanoparticle surface using TNBS assay

The determination of amino groups on the surface of **3.1.1** was performed using the 2,4,6-trinitrobenzenesulfonic acid (TNBS) method according to the procedure already discussed in **Chapter 2, Section 2.4.3.2.** From this analysis, the amine density on the surface was detected to be around 28.8 nm/ mg.

3.2.4.3 Determination of RITC, FA and MTX content

The concentration of RITC on nanoparticle surface was obtained by measuring the optical density of an aqueous suspension of the nano-bicomposite **3.1.2** at 540 nm (ε =106,000 $M^{-1}cm^{1}$). Free RITC was used as the reference. The number of RITC bound per particle was also calculated by determining the residual amine concentration by TNBS assay. From this analysis, the amount of RITC immobilized per unit mass of the particle was detected to be 1.6 nmol/ mg.

To further determine the extent of folate conjugation on **3.1.1**, nanoparticles were digested with trypsin for 12 h at 37°C with continuous agitation. Following tryptic hydrolysis of folate-conjugated USPIONs, the folate density on nanoparticle surface was determined by spectrophotometric analysis at the absorbance of 358 nm (folic acid ε = 8643.5 M^{-1} cm^{-1}) and also cross-checked by determination of residual amine concentration via the TNBS assay. From this analysis, folate density on the nanoparticle surface was detected to be around 29.78 nmol/ mg, which is pretty consistent with an equivalent amine loss (31.67 nmol/ mg) on the surface.

For quantifying the extent of drug immobilization on nanoparticle surface, a suspension of the **3.1.5** in PBS (pH=8) was stirred for 24 h in presence of porcine liver esterase in order to ensure complete detachment of MTX from the nanoparticle surface via hydrolysis of the ester bond. Following magnetic separation of the nanoparticles, the average number of MTX immobilized per particle was determined spectrophotometrically by recording the absorbance of the hydrolysis solution at 302 nm.

Since it is known that the mean diameter of the magnetite nanoparticles is 5 nm, the number of Fe atoms in every Fe_3O_4 particle can be calculated by means of the following formula,

$$N_{Fe} = 4/3\ \pi r^3 N_A / V_M\ (Fe_3O_4) \qquad \textbf{Eq. 3.2}$$

where V_M (Fe_3O_4) refers to the molar volume of bulk Fe_3O_4, r is the mean radius of Fe_3O_4 nanoparticles, N_A is Avogadro's number. The number of RITC, FA and MTX immobilized per particle was calculated assuming 2646 Fe atoms per particle calculated using the above formula.

3.2.4.5 Optimization of RITC, FA and MTX content on the nanoparticle surface

To obtain an optimal concentration of the fluorophore, targeting agent and drug on the nanoparticle surface, control conjugates were synthesized according to the procedure already described in Section **4.2**, keeping the concentration of the aminated nanoparticles **3.1.1** constant and varying the molar concentration of RITC (0.5-5 mg), FA (0.01-0.1 mmol) and MTX (0.01-0.05 mmol) in the subsequent steps. Uptake profile of these control conjugates, synthesized with different molar ratio of the functional molecules were studied against folate-receptor positive human cervical HeLa cell line and the one which gave the optimal results were used for detailed investigations.

3.2.5 Drug release study

To mimic the intracellular lysosomal conditions, **3.1.5** (0.5 mg/ml) was suspended in a solution of crude protease (0.1 mg/ml) from bovine pancreas in phosphate buffered saline (PBS) solution (5 ml) at 37°C under constant stirring. The solution was divided into five parts and pH of the individual sets was adjusted by titration with 0.1 (M) NaOH or 0.1 (M) HCl to achieve the different pH values of 2, 3, 4, 5.6 and 7.44 respectively. Following incubation for 8, 16, 24 and 48 h, the nanoparticle suspensions were isolated by magnetic decantation to free the nanoparticles from cleaved MTX, protease and PBS. MTX cleaved from nanoaparticles was then quantified with UV spectroscopy at wavelength of 302 nm.

3.2.6 *In-vitro* studies

- **Cell culture:** The cells cultivated for *in vitro* experiments were human cervix adenocarcinoma, HeLa and human osteosarcoma, MG-63 cell lines, obtained from the National Centre for Cell Sciences (NCCS) Pune, India. All cell lines were

cultured on folate free Dulbecco Modified Eagle's Medium (FFDMEM) and Minimal Essential Medium (MEM) respectively with 10% fetal calf serum, 100 units ml^{-1} penicillin and 100 μg ml^{-1} streptomycin, 4 mM L-glutamine at 37°C in a 5% CO_2 and 95% air humidified atmosphere.

- **Intracellular uptake studies: Preliminary quantification was nanoparticle uptake** by different cell lines was performed using magnetically activated cell sorting (MACS) and fluorescence microscopy following the protocol, already discussed in **Chapter-2**, **Section-2.4.3.8.** For fluorescence microscopy, cells were treated with different nanoparticle preparations (1 mg/ ml) and the incubation time was 24 h

- ***In-vitro* cellular MR imaging:** Samples for MR phantom imaging were prepared by suspending 10^6 cells in 50 µL low-melting 1% agarose gel. Cell suspensions cultured with different nanoparticle concentrations (0.01-0.1 mg/ml) were loaded into 1.5 ml eppendorf tubes and allowed to solidify at 4° C. Samples were then sealed with additional agarose to avoid air susceptibility artifacts. MR imaging was performed with a 0.3 T clinical MRI scanner (HITACHI, AIRIS), using a fabricated sample holder. A spin-echo multisection pulse sequence was selected from the Hitatchi Medical System (Version- 7.0) to acquire MR phantom images. Repetition time (TR) of 2100 ms and variable echo times (TE) of 95-150 ms were used. The spatial resolution parameters were set as follows: an acquisition matrix of 256×256, field of view of 240 ×240 mm^2, section thickness of 8 mm and 2 averages. The MRI signal intensity (SI) was measured using the in-built software. T_2 values were obtained by plotting the SI of each sample over a range of TE values. T_2 relaxation times were then calculated by fitting a first-order exponential decay curve to the plot. The fitting equation can be expressed as $SI = A.\ e^{(-TE/T_2)} + B$, where SI is the signal intensity, TE is the echo time, A is the amplitude, and B is the offset. The relaxivity, the R_2 value, was also calculated as the inverse of T_2.

- **Nanoparticle mediated cytotoxicity:** 4×10^5 HeLa cells were seeded to 96 well tissue culture plates in a total volume of 180 μl of complete media and kept for 18 h. After that 20 μl of different nanoparticle preparations (taken at different concentrations) were added to the cells and incubated for different time periods (4-48 h) at 37° C in a humidified incubator (HERA cell) maintained at 5% CO_2, and the cell viability was

assessed by the 3-(4,5-dimethylthiazol)-2-diphenyltertrazolium bromide (MTT) test, as described in the previous chapter.

- **Quantitative evaluation of nanoparticle induced apoptosis and cell cycle analysis:** For cell-cycle analysis, HeLa cells were treated with 0.05 mg/ml of both USPIO-PMIDA-EDBE-FA-OH (used as control) and USPIO-PMIDA-EDBE-FA-OH-MTX for 0.5 hour, washed thoroughly with PBS to remove the non-internalized particles and incubated at 37° C for 4 and 24 h respectively. Following incubation, the cells were washed with ice cold PBS (10 mmol, pH 7.4) and resuspended in 200 µl of PBS followed by incubation with 20 µl DNase free RNase (10 mg/ml) and 20 µl of DNA intercalating dye propidium iodide (PI) (1 mg/ml) at 37° C for 1 h in dark. Apoptotic cells were determined by their hypochromic sub-diploid staining profiles. The distribution of cells in the different cell-cycle phases was analyzed from the DNA histogram using Becton-Dickinson FACS Caliber flow cytometer and Modfit software.

3. 3. Results and Discussions

It is well documented that an aminated base facilitates conjugation with a diverse array of functional molecules through sulfhydryl, carboxyl, anhydride or imine chemistry, allowing easy manipulation of surface functionality. In the previous chapter, we proceeded directly with an amine functionalized nanomagnetite precursor, synthesized through the covalent grafting of 2-aminoethylphosphonic acid on magnetite nanoparticles. While α, β or γ-aminophosphonates are commercially available, they remain expensive and the synthetic methods involved are quite complicated, low-yielding and difficult to scale up. In order to circumvent these problems, ultrasmall superparamagnetic magnetite nanoparticles with surface-pendant amine groups were synthesized via a two step-procedure. The first step involved the synthesis of ultrasmall superparamagnetic magnetite nanoparticles **(3.1)** by alkali-mediated chemical co-precipitation of Fe^{3+} and Fe^{2+} in the presence of N-phosphonomethyl iminodiacetic acid while the second step involved subsequent activation of **3.1** with 1-ethyl-3-(dimethylaminopropyl) carbodiimide (EDC) and *N*-hydroxysuccinimide (NHS), followed by reaction with an excess of 2, 2′-(ethylenedioxy)-bis-ethylamine (EDBE). This led to the formation of an amine functionalized nanomagnetite support USPIO-PMIDA-EDBE (**3.1.1**), which in the later course of the reaction served as the bio-conjugating precursor (**Scheme 3.1**).

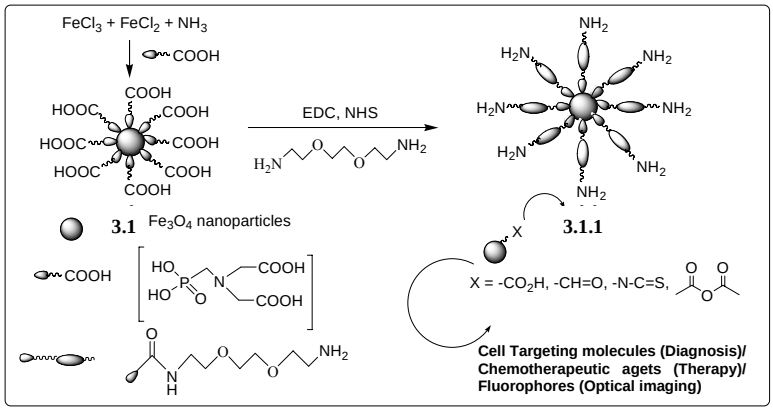

Scheme 3.1: Synthesis of USPIO-PMIDA-EDBE (**3.1.1**)

Magneto-fluorescent analogue of **3.1.1** was developed as depicted in **Scheme 3.2.** The active $-NH_2$ groups present on **3.1.2** were covalently conjugated with FA via nonselective carbodiimide activation of the carboxyl groups in its glutamic acid moiety. The conjugation of glycidol to USPIO-PMIDA-EDBE-RITC-FA (**3.1.3**) was a necessary precursory step in order to attach MTX via a pH-labile ester linkage. Glycidylation of **1.3** converted all the remaining primary amino groups to alcohol groups, producing USPIO-PMIDA-EDBE-RITC-FA-OH (**3.1.4**). The conjugation of MTX to **1.4** using standard EDC chemistry afforded the desired trifunctional conjugate USPIO-PMIDA-EDBE-RITC-FA-OH-MTX (**3.1.5**).

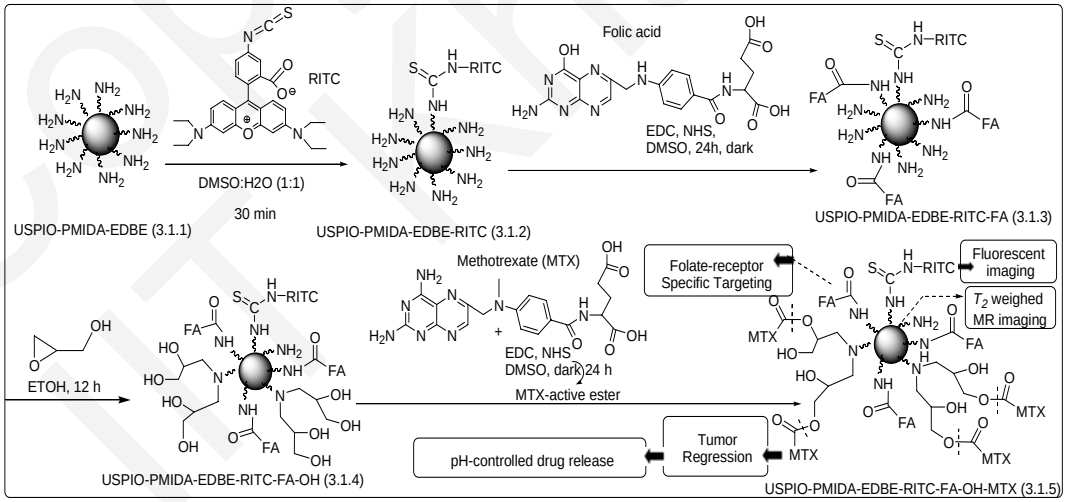

Scheme 3.2: Synthesis of USPIO-PMIDA-EDBE-RITC-FA-OH-MTX (**3.1.5)**

Amine density on **3.1.1** as well as the number of RITC, FA and MTX immobilized on each nanoparticle was quantified using UV visible absorbance data as described in the earlier reports [10, 11] with minor modifications. Iron content in the nanoparticles was determined spectrophotometrically and the average number of each functional molecule immobilized on the nanoparticle surface was quantified assuming 2646 Fe atoms per particle, theoretically calculated using the reported literature procedure. From this analysis, the average numbers of RITC, FA and MTX on each nanoparticle with an average diameter of 5 nm were determined to be 4.48, 46.01 and 89.79 respectively (**Table 3.1**). The values were however consistent with the systematic reduction in the number of surface amine groups, as quantified by determination of residual amine concentration by TNBS assay.

Table 3.1: Quantification of amine density and functional molecules on **USPIO 3.1.1-3.1.5**

Nanoparticles	$-NH_2$	RITC	FA	-OH	MTX
3.1.1	80.68	-	-	-	-
3.1.2	76.39	4.48	-	-	-
3.1.3	29.78	4.48	46.01	-	-
3.1.4	2.82	4.48	46.01	ND	-
3.1.5	2.83	4.48	46.01	ND	89.79

Figure 3.1 presents the high resolution X-ray diffraction pattern of **3.1**. The d values correspond to those of inverse spinel magnetite [Fe_3O_4] (JCPDS card no. 85-1436). The broadening of peaks indicates nanocrystalline nature of the synthesized powder, which translates into an average core size of about 4 nm using the Debye–Scherrer formula for spherical particles.

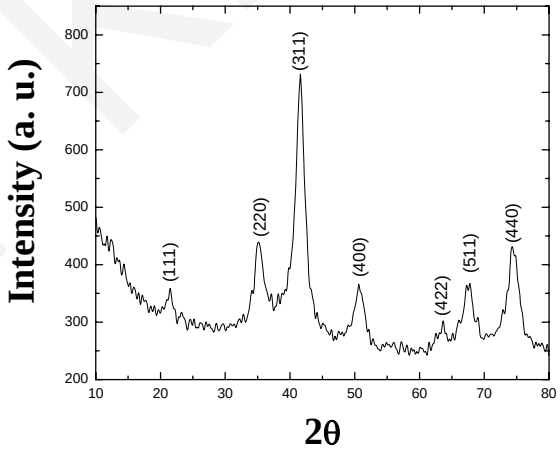

Fig. 1: X-ray diffraction pattern of **3.1**

Transmission electron micrograph (TEM) of **3.1,** displayed in **Fig. 3.2,** shows that thousands of ultra-fine particles with nearly spherical morphology organize themselves to form nano-aggregates, which is probably a consequence of the removal of dispersing phase during sample preparation and is not representative of the real state of nanoparticles in suspension. In aqueous suspension, these functional nanoparticles exhibited considerable dispersancy. From TEM analysis, the average diameter of the particles was calculated to be 5 ± 0.5 nm. Size distribution was significantly narrow (2-8 nm). The high-resolution TEM image presents lattice imaging of the (220) plane, d = 2.93 Å. The selected-area electron diffraction (SAED) pattern indicates the polycrystalline nature of the embedded magnetite particles. The individual planes identified from the SAED pattern correlates well with that of the XRD pattern.

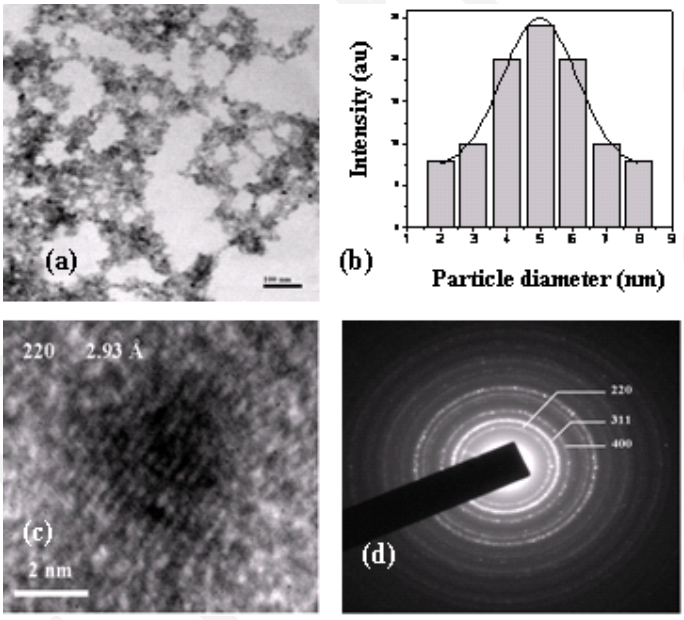

Fig. 3.2: (a) High resolution transmission electron micrograph (HRTEM) of **3.1 (b)** Particle size distribution histogram **(c)** Single particle HRTEM and **(d)** corresponding SAED pattern.

Dynamic light scattering (DLS) studies of **3.1** further confirmed the presence of stable, non-aggregated particles with a mean hydrodynamic diameter (HD) of 30 ± 3 nm and polydispersity index (PDI) less than 0.2. The final conjugate (**3.1.5)** presented a mean HD of 62 ± 4 nm (PDI = 0.191) and surface charge of -43.4 ± 2 mV at neutral pH. These functional nanoaparticles showed excellent stability in aqueous medium as their HD, PDI, zeta potential and T_2 relaxivity remained unaffected over a long period of time (**Table 3.2**)..

Table 3. 2: Stability analysis of **3.1.5**

Time (months)	1	2	3	4	5	6	7
HD (nm)	62	58	59	63	68	66	68
PDI	0.191	0.186	0.188	0.193	0.204	0.193	0.197
ξ-potential (mV)	-42.4	-43.6	-41.9	-39.7	-37.6	-39.6	-37.6
r_2 ($s^{-1}mM^{-1}$)	294	287	288	286	291	2 96	297

The FTIR spectrum of USPIO-PMIDA functionalized nanoparticles, presented in **Fig. 3.3** exhibits a strong band around 598 cm^{-1}, characteristic of the Fe-O vibration related to the magnetite core. As compared to unbound PMIDA, the peak associated with >C=O stretching bands of carboxylic acids shifted from 1736 cm^{-1} to a much lower wave number (~1624 cm^{-1}) in **3.1,** possibly due to the formation of intraparticle hydrogen bonding between the surface – CO_2H groups.

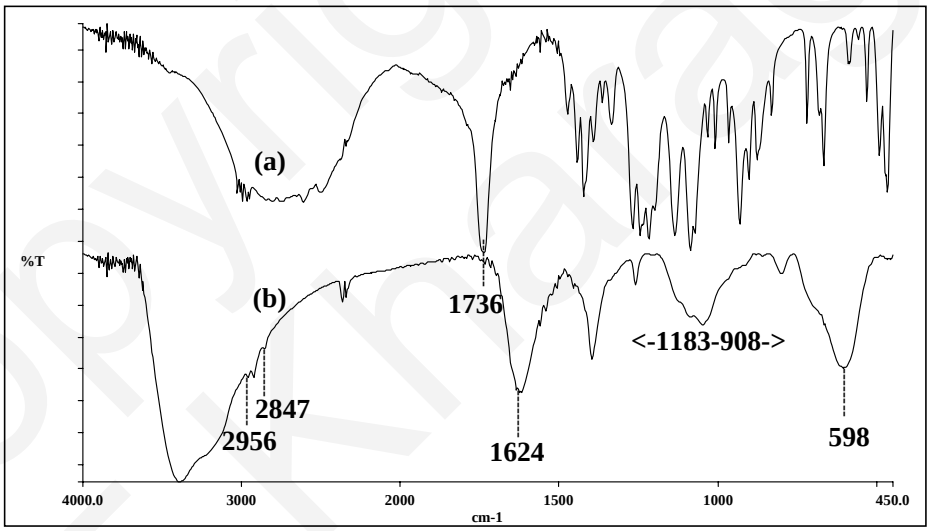

Fig. 3.3: FTIR spectra of **(a)** PMIDA (unbound) and **(b)** USPIO-PMIDA (**3.1**)

The FTIR spectrum of **3.1** (**Fig. 3.4**) exhibits a broad band in the range of 1472-1685 cm^{-1}, ascribed to the overlapping of free $–NH_2$/–NH bending (scissoring) vibration (amide-II) and –C=O absorption (amide-I). Following FA immobilization, the amide carbonyl bands **3.1.1** at 1635 and 1556 cm^{-1} as also the $–CH_2$ stretching vibrations at 2856 and 2926 cm^{-1} intensified. FA standard shows characteristic bands at 1603 cm^{-1}, which shifted to 1617 cm^{-1} in the

conjugated sample. Because of the structural similarity between FA and MTX, considerable similarity was evident between the spectral pattern of FA and MTX grafted nanoparticles. Characteristic bands of MTX appeared at 1559, 1620 and 1649 cm^{-1}, which were almost close to FA standard. Additionally, a weak but distinct signal appeared at 1735 cm^{-1}, which, however is attributed to the covalent attachment of MTX on **3.1.4** via ester linkage. Precise characterization of small molecules linked to the surface of MNPs often becomes difficult because these are solid phase samples and are coated with only a small amount of these small molecules [12]. Further in case of multifunctional nanoparticles, the surface is shared by multiple functional molecules and relative fraction of individual functional entities, associated with the nanoparticle surface may be lower than the detection limit of the available spectroscopic techniques. Hence, to revalidate the successful immobilization of MTX on USPIO surface via ester linkage, we relied on an alternative strategy, which consisted of detachment of MTX from the USPIONs through a base-catalyzed ester hydrolytic cleavage and subsequent analysis of the hydrolysis solution for free MTX using UV visible techniques. In addition to qualitative detection, this method even allowed for the quantification of the number of MTX molecules, associated with each nanoparticle.

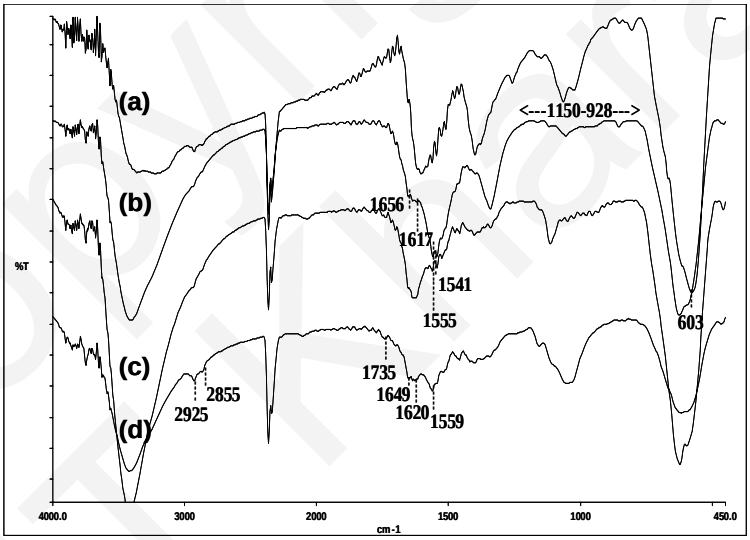

Fig. 3.4: FTIR spectra of (**a**) USPIO-PMIDA-EDBE (**b**) USPIO-PMIDA-EDBE-FA (**c**) USPIO-PMIDA-EDBE-FA-OH and **(d)** USPIO-PMIDA-EDBE-FA-OH-MTX**.**

XPS analysis was further used to validate the successful coating of PMIDA on magnetite surface. The high-resolution O1s spectrum of PMIDA (**Fig. 3.5**) coated magnetite displayed three peaks at 530.1, 531.1, 531.9 and 532.4, corresponding to oxygen being present in four

different environments as P-O, C-O, Fe-O and O-H. The P2p spectrum exhibited two peaks at 132.3 eV and 133.7 eV, corresponding to $P2p_{3/2}$ and $P2p_{1/2}$ respectively. The Fe 2p doublet with binding energy values of 710 and 725 eV implied the presence of Fe-O bonds, typical for magnetite. In **3.1**, the N1s appeared at 406.08 eV, which is very close to the N1s binding energy of tertiary nitrogen in PMIDA, whereas in **3.1.5**, the N1s spectrum displays two additional peaks at 398.6 eV and 401.3 eV respectively, corresponding to the free $–NH_2$ groups, native to the pteridine rings in FA/ MTX and amide (-NH-C=O) bonding within FA structure as also the amide linkage between (i) **1** and EDBE and (ii) FA and EDBE as well.

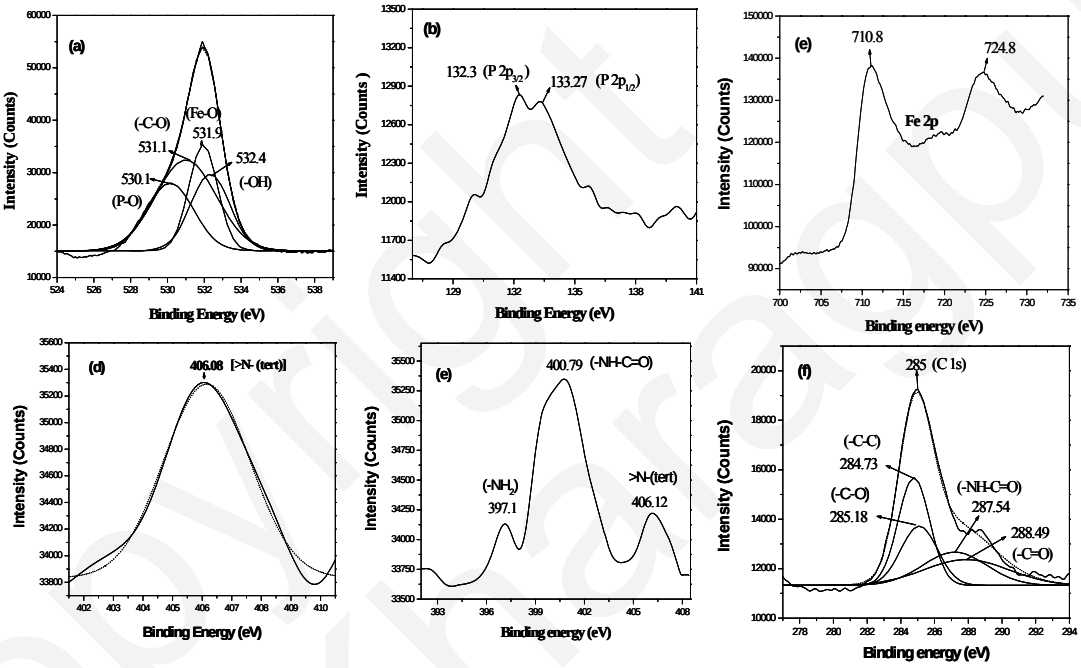

Fig. 3.5: The high resolution (**a-d**) O1s, P2p, Fe2p and N1s XPS spectrum of USPIO-PMIDA (**e-f**) N 1s and C1s spectrum of USPIO-PMIDA-EDBE-FA-OH-MTX.

The chemical percentages (a %) of Fe, O, C, P and N in **1** were 2.8, 21.4, 74.3, 0.9 and 0.6 respectively, while those of **3.1. 5** were 1.2, 17.6, 74.1, 0.9 and 6.2 respectively. As compared to **3.1** the nitrogen content of **3.1.5** significantly increased, indicative of the successful incorporation of EDBE, FA and MTX on the nanoparticle surface. Furthermore, the high resolution C1s spectrum displayed four peaks at 284.2, 285.7, 286.9 and 288.6, attributed to –C-C, -C-O, -NH-C=O and –C=O (typical of ester/carboxylic acid consistent with the attachment of MTX to USPIO s via ester linkage). The unaltered Fe 2p spectrum in both samples clearly indicates that surface modification has no deleterious effect on the support material. This was further corroborated by magnetization measurements of **3.1.5**, which

established that even after modification with multiple functional entities, superparamagnetism of the final conjugate remained unaltered, as indicated by an anhysteric magnetization (M-H) curve, lacking coercivity and remenance (**Fig. 3.6**).

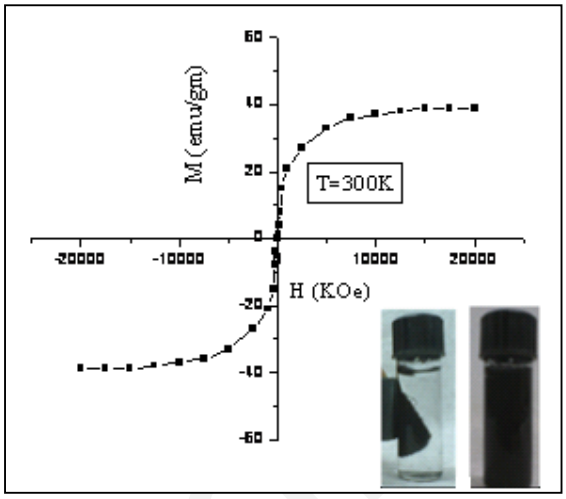

Fig. 3.6: Magnetization (M-H) curve of **3.1.5** at 300 K

In order to demonstrate the cancer targeting ability of USPIO-PMIDA-EDBE-FA-OH-MTX (**3.1.5**), *in vitro* cellular uptake experiments were conducted using the folate-receptor (FR) positive human cervical carcinoma HeLa cells as our target cell-line. Magnetically activated cell sorting (MACS) was employed for preliminary quantification of the nanoparticle uptake inside the target cells. Cellular uptake of the conjugates containing FA as the targeting molecule was significantly high as compared to their non-targeted control, demonstrating active targeting of magnetite nanoparticles through the interaction between the folate groups on nanoparticle surface and receptors of HeLa cells (**Fig. 3.7**).

To further confirm the receptor-specificity for the conjugate, the uptake of **3.1.5** by HeLa cells was also compared with the uptake by folate-receptor negative human osteosarcoma, MG-63 cell-line, expressing very low levels of both α and ß forms of the folate receptor. In the case of FR over-expressing HeLa cells, nanoparticle uptake was much greater for the targeted particles as compared to their non-targeted counterparts. Conversely, MG-63 cell uptake level of folate-targeted nanoparticles was considerably low and similar to those of the non-targeted controls.

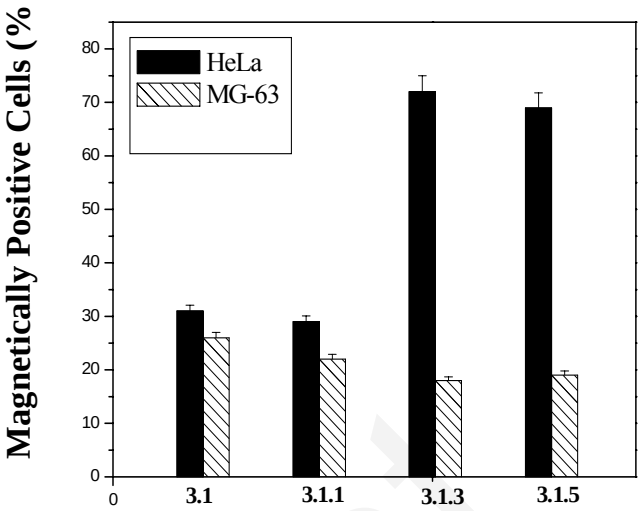

Fig. 3.7: Quantification of USPIO uptake by FR positive HeLa and FR negative MG-63 cell lines via magnetically active cell-sorting (MACS) analysis. Cellular uptake of the conjugates containing FA as the targeting molecule has been significantly enhanced in comparison to their non-targeted control. The uptake of folate-targeted nanoparticles in MG-63 cell line is considerably low and similar to those of the non-targeted controls.

Magnetic resonance phantom imaging was further used as a tool for evaluating the detectibility of the as-prepared formulations by MRI and to additionally confirm their association with FR-over-expressing HeLa cells [12], in addition to the MACS based quantification described above. MR phantom samples were prepared by suspending HeLa cells incubated with nanoparticle designs **3.1.2-3.1.5** for two hours in agarose. The T_2 weighed phantom image of cells, incubated with folate-targeted USPIOs showed a significant negative contrast enhancement in comparison to its non-targeted control, suggesting effective nanoparticle internalization inside the target cells (**Fig. 3.8**). Slight loses in signal intensity were however observed for cells incubated with USPIO-PMIDA-EDBE, when compared to blank cells cultured without nanoparticles. This is due to some non-specific internalization of these ultrasmall nanoparticles through enhanced permeation and retention (EPR) effect.

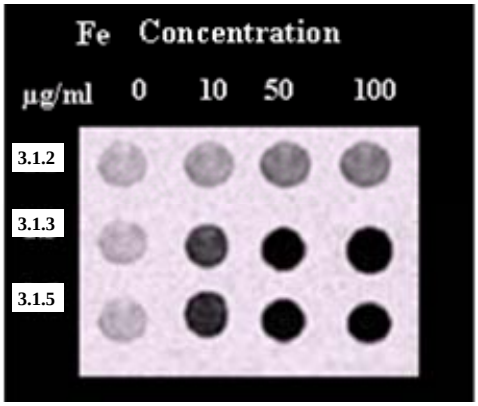

Fig. 3.8: T_2-weighted spin-echo MR phantom images of HeLa cells incubated with 0-100 µg/ml of **3.1.2, 3.1.3** and **3.1.5** for 2 h.

The relative relaxation times of **3.1.2 - 3.1.5** were quantified through T_2 weighted spin-echo MR images. **Fig. 3.9** shows that T_2 relaxation time varies as a function of **USPIO** concentration in cell-culture media. HeLa cells cultured with **3.1.3** and **3.1.5** had a shorter T_2 relaxation time (higher relaxivity) than their non-functionalized counterpart **3.1.2** attributed to enhanced magnetism resulting from the higher uptake of the former by HeLa cells in comparison to the latter. All these results unambiguously established the potential of our as-prepared nanoformulation as a cancer-targeted, MR imaging probe.

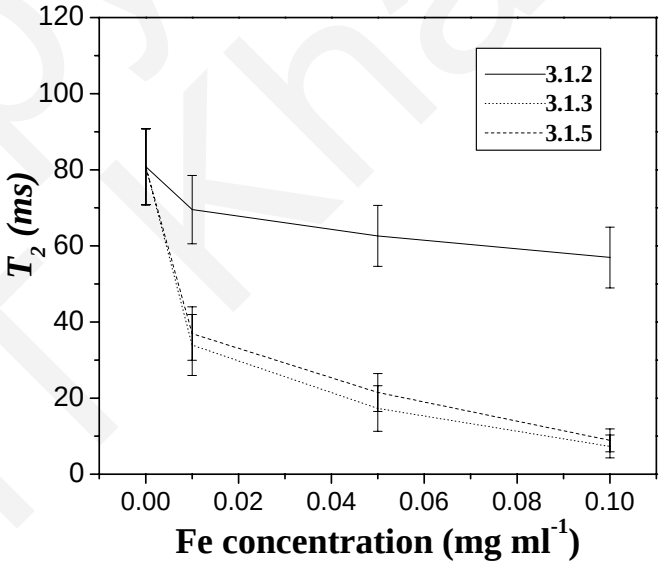

Fig. 3.9: T_2 relaxation analysis of HeLa cell suspensions magnetically labeled with **3.1.2, 3.1.3** and **3.1.5**

In vitro drug release experiments, conducted with **3.1.5** under different pH conditions (pH 2.0-7.4) showed a typical release profile i.e. an initial burst release, followed by a sustained release pattern (**Fig. 3.10**).

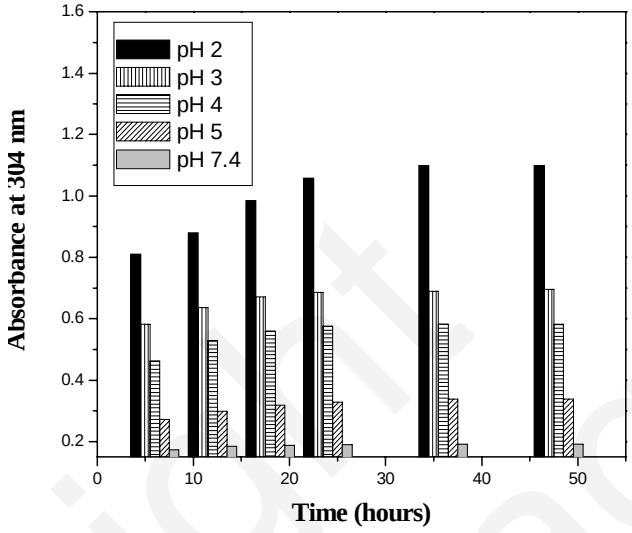

Fig. 3.10: pH-dependant drug-release behavior of **3.1.5** under typical lysosomal conditions. Highest absorbance is observed at pH 2 whereas drug release at physiological pH is negligible. This pH-dependant release behavior suggests that MTX will be released more in acidic tumor sites than in the normal tissues.

The overall release rate was much higher in the lower pH range (pH 2-5) and negligible drug release was observed at physiological pH. This pH-dependant release behavior suggested that MTX is more prone to release in acidic tumor sites than in the normal tissues. Once the particles are internalized inside the cells through FR mediated endocytosis, the decreased pH values may induce further accelerated release inside the acidic endosomes of tumor cells through cleavage of the ester bond.

To further test the efficacy of MTX cleavage inside the target cells, HeLa cells were cultured with **3.1.2 - 3.1.5** and free MTX in a FA deficient medium. Nanoparticle-induced cytotoxicity was determined by the MTT assay. While nanoparticles deprived of MTX were shown to be non-cytotoxic even at high concentrations (upto 0.5 mg/ml) [**Fig. 3.11 (a)**], both **3.1.5** and soluble MTX reduced the cellular viability in a time and dose-dependant fashion [**Fig. 3.11 (b)**], establishing the ability of the cells to cleave MTX inside the acidic lysosomes.

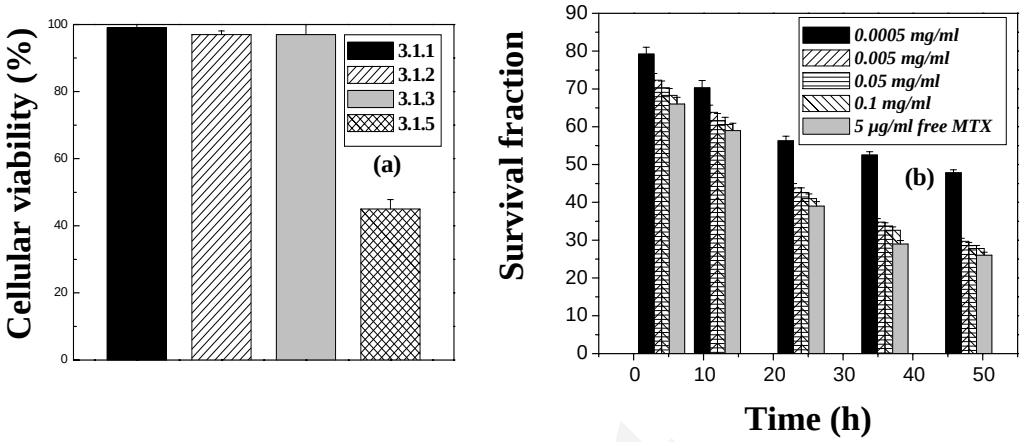

Fig. 3.11 (a) Cytotoxicity profile of HeLa cells incubated with functional nanoparticles **3.1.1**-**3.1.5** at a concentration of 0.5 mg/ml for 12h. Nanoparticles deprived of MTX were shown to be highly bio-compatible whereas a significant reduction in cellular viability was observed for the MTX modified nanoparticles**. (b)** Reduction in viability of HeLa cells as a function of time and nanoparticle concentration in culture medium

Following 24 h in culture, cells exposed to drug modified nanoparticles demonstrated a significant reduction in cellular viability. It was further observed that for concentrations of MTX grafted nanoparticles at or higher than 0.01 mg/ml, the cells showed a statistically equivalent reduction in cellular viability.

In order to verify whether **3.1.5** could induce cell-death through the initiation of apoptosis, HeLa cells were cultured with 1.0 mg/ml of **3.1.2, 3.1.3** and **3.1.5** for 0.5 h, washed to remove the non-internalized nanoparticles, incubated at 37°C for 24 h and visualized using fluorescence microscopy (**Fig. 3.11**). As expected, the non-targeted control **3.1.2** showed little or practically no internalization. On the other hand, intense red fluorescence could be detected in the cytoplasm of cells treated with the folate targeted USPIOs, demonstrating their cellular internalization through receptor mediated endocytosis. To further examine the nuclear morphology and visualize cell-death, cell-nuclei were further stained with 4'-6-Diamidino-2-phenylindole (DAPI), a nuclear staining dye known to exhibit strong blue fluorescence, when bound to DNA. Consistent with the earlier prediction from cytotoxicity experiments, fluorescence images of HeLa cells, incubated with control nanoparticles (**3.1.2**-**3.1.3**) displayed well preserved nuclear structure without any visible abnormalities. On the contrary, cells treated with **3.1.5** displayed typical apoptotic morphology, which included condensed nuclei, membrane blebbling and formation of apoptotic bodies.

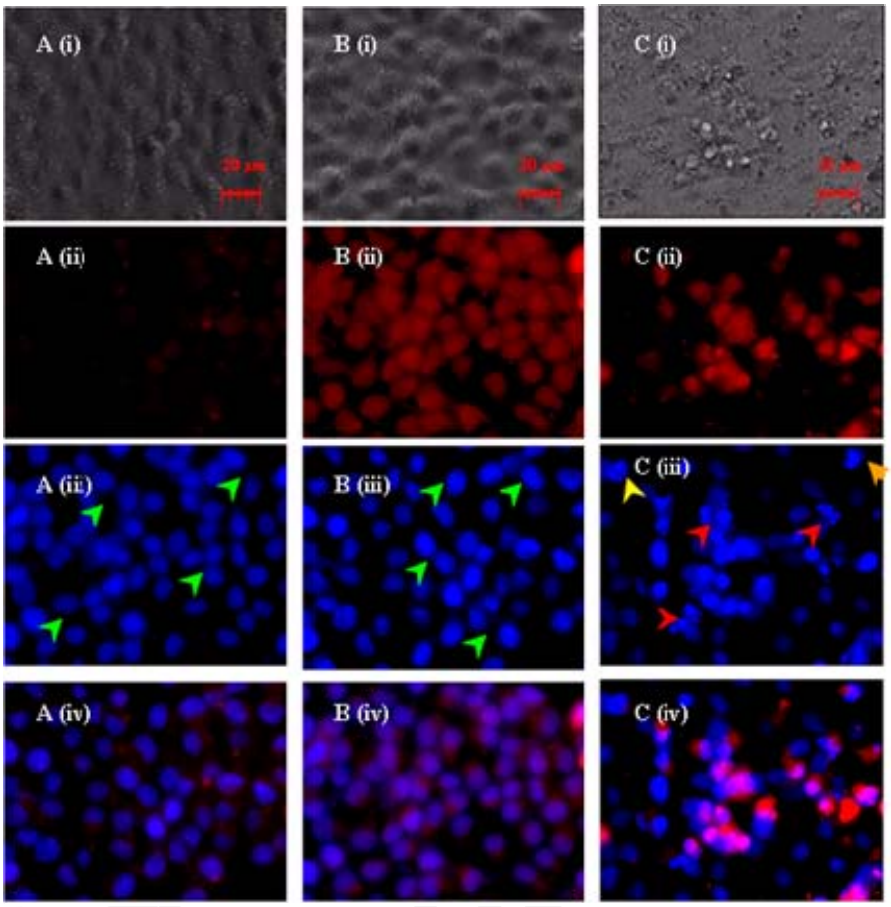

Fig. 3.12 Fluorescence image of HeLa cells incubated with **(A)** USPIO-PMIDA-EDBE-RITC **(3.1.2) (B)** USPIO-PMIDA-EDBE-RITC-FA **(3.1.3)** and **(C)** USPIO-PMIDA-EDBE-RITC-FA-OH-MTX **(3.1.5).** The top to bottom panels of each incubation type represents **(i)** phase contrast **(ii)** RITC fluorescence **(iii)** DAPI fluorescence and **(iv)** merged RITC + DAPI fluorescence images respectively. The green arrows represent healthy nuclei whereas yellow, orange and red arrows represent some typical features of nanoparticle induced apoptosis, which include apoptotic initiation, nuclear condensation and nuclear fragmentation leading to the formation of apoptotic bodies.

In addition to these qualitative evaluations, USPIO induced apoptosis was also quantitatively appraised through cell-cycle analysis, using the standard propidium iodide (PI) flow cytometric assay. Results showed that DNA fragmentation was almost negligible in case of untreated cells as well as cells treated with **3.1.3** even after 24 h of incubation. However, significant DNA fragmentation was envisaged in cells treated with drug-modified nanoparticles under similar experimental conditions, evidenced as a "sub-G1" peak in the DNA fluorescence histogram (**Fig. 3. 12**). Cell cycle analysis further demonstrated that both G_0/G_1 and G2/M phases decreased in function of time with concomitant elevation of the sub-

G1 or apoptotic phase. The cell cycle was arrested in the S phase, which was well-consistent with the mode of action of MTX. This mitotic arrest was responsible for the dramatic cellular morphological changes, as visualized by fluorescence microscopy and ultimately led to cell-death.

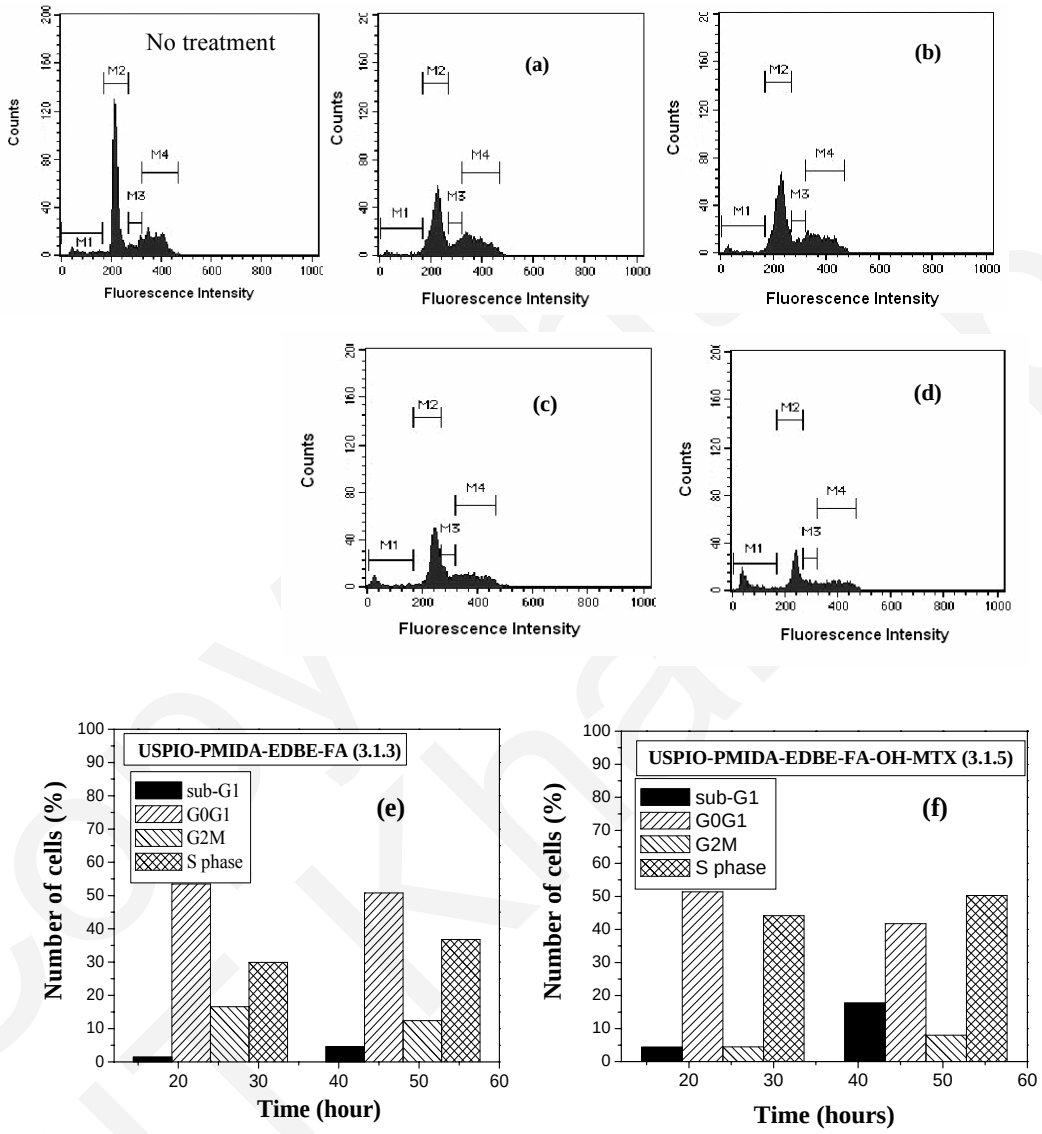

Fig. 3. 13 Apoptosis study and cell-cycle analysis using propidium iodide (PI) flow cytometric assay **(a-b)** DNA fluorescence histogram of USPIO-PMIDA-EDBE-FA (**3.1.3**) at 4 and 24 h respectively (**c-d**) DNA fluorescence histogram of USPIO-PMIDA-EDBE-FA-OH-MTX (**3.1.5**) at 4 and 24 h respectively [M1, M2, M3 and M4 represents the sub-G1, G0-G1, G 2M and S phase of the cell-cycle respectively. (**e-f**) Cell cycle analysis of **3.1.3** and **3.1.5** against time.

3. 4. Conclusions

In conclusion, a novel, phosphonic acid mediated bio-functionalization approach has been adopted to synthesize a multimodal and theragnostic nano-agent, which combines magnetic as well as receptor-specific targeting, magnetic resonance cum optical imaging and pH-sensitive drug release property into one system. These functional nanoparticles are stable in aqueous buffered solutions, possess good cellular targeting ability, and their simple synthesis process is amenable to scale-up. The effectiveness of our surface-design has been well-established by *in-vitro* cell-uptake, MR imaging and apoptosis studies. Moreover, the drug-immobilized USPIONs, when conjugated with folic acid can selectively target and kill cancer cells which overexpress the folate receptor, while sparing the FR deplete normal cells. In addition, the dual optical and magnetic properties of the synthesized nanoparticles may be exploited for the dual fluorescence and MR-based imaging and real-time monitoring of tumor regression in response to drug treatment. All these positive attributes make these functional nanoparticles a promising system for further *in vivo* evaluation.

References

1. Zhang, X. J.; Lewis, P. J.; Chu, C. C. Fabrication and characterization of a smart drug delivery system: microsphere in hydrogel. *Biomaterials* **2005**, *26*, 3299–3309

2. Majoros, J.; Thomas, T P.; Mehta, C B.; Baker, J. R. Poly (amidoamine) dendrimer-based multifunctional engineered nanodevice for cancer therapy, *J. Med. Chem.* 2005, *48,*5892-5899

3. Yigit, M. V.; Mazumdar, D.; Kim, H. K.; Lee, J. H.; Odintsov, B.; Lu, Y. Smart "turn-on" magnetic resonance contrast agents based on Aptamer-functionalized superparamagnetic iron oxide nanoparticles, *ChemBioChem* **2007**, *8*, 1675–1678

4. Kim, J.; Lee, J. E.; Lee, S. H.; Yu, J. H.; Lee, J. H.; Park T. G.; Hyeon, T. Designed Fabrication of a Multifunctional Polymer Nanomedical Platform for Simultaneous Cancer-Targeted Imaging and Magnetically Guided Drug Delivery, *Adv. Mater.* **2008**, *20*, 478–483

5. Shi, X.; Wang, S. H.; Swanson, S. D.; Ge, S.; Cao, Z.; Antwerp, M. E.; Landmark, K. J.; and Baker, J.R. Multifunctional Dendrimer-Modified Multiwalled Carbon Nanotubes: Synthesis, Characterization, and In Vitro Cancer Cell Targeting and Imaging, *Adv. Mater*. **2008**, *20*, 1671–1678

6. Yu, M. K.; Jeong,Y. Y.; Park, J.; Park, S.; Kim, J. W.; Min, J. J.; Kim K.; and Jon, S. Drug-loaded superparamagnetic iron oxide nanoparticles for combined cancer imaging and therapy in vivo, *Angew. Chem. Int. Ed.* **2008**, *47*, 5362 –5365

7. Adden, N.; Gamble, L. J.; Castner, D.G.; Hoffmann, A.; Gross, G.; Menzel, H. Phosphonic Acid Monolayers for Binding of Bioactive Molecules to Titanium Surfaces *Langmuir* **2006,** *22* 8197

8. Yee, C.; Kataby, G.; Ulman, A.; Prozorov, T.; White, H.; King, A.; Rafailovich, M.; Sokolov, J.; Gedanken, A. Self-Assembled Monolayers of Alkanesulfonic and -phosphonic Acids on Amorphous Iron Oxide Nanoparticles, *Langmuir* **1999,** *15,* 7111-7115

9. Lalatonne, Y.; Paris, C.; Serfaty, J. M.; Weinmann, P.; Lecouvey, M.; Motte, L.Y. Bis-phosphonates-ultra small superparamagnetic iron oxide nanoparticles: a platform towards diagnosis and therapy, *Chem. Commun*. **2008**, 2553–2555

10. (a) Koch, A. M.; Reynolds, F.; Kircher, M. F.; Merkle, H. P.; Weissleder, R.; Josephson, L.; Uptake and metabolism of a dual fluorochrome tat-nanoparticle in HeLa cells, *Bioconjugate Chem*. **2003**, *14*, 1115-1121 (b) Shen, T.; Weissleder, R.; Papisov, M.; Bogdanov, A.; Brady, T. J. Jr.; Monocrystalline iron oxide nanocompounds (MION): physicochemical properties. *Magn. Reson. Med*. **1993**, *29*, 599–604

11. Zhang, L.; Hou, S.; Mao, S.; Wei, D.; Song, X.; Lu, Y. Uptake of folate-conjugated albumin nanoparticles to the SKOV3 cells, *International Journal of Pharmaceutics* **2004,** *287***,** 155-162

12 (a) Zhang, B.; Bing, Y. Analytical strategies for characterizing the surface chemistry of nanoparticles. *Anal. Bioanal. Chem.* **2009**, DOI 10.1007/s00216-009-2996-1 (b) Zhou, H.Y.; Du, F. F.; Li, X., Zhang, B.;W. Li.; Yan B. Characterization of Organic Molecules Attached

to Gold Nanoparticle Surface Using High Resolution Magic Angle Spinning ^{1}H NMR *J. Phys. Chem. C*, 2008, 112, 19360–19366

Chapter 4

Biofunctionalization of Magnetite Nanoparticles Using a Chemoselective Approach: From a Tailored Bifunctional Surface to a "Smart" Theragnostic Nanomedicine

4. 1. Introduction

In the last few years, research towards the fabrication of high quality, superparamagnetic nanohybrids have gained a phenomenal impetus for their eclectic *in vitro* and *in vivo* applications, which include magnetic resonance imaging (MRI) contrast enhancement, magnetically controlled drug and gene delivery, heating mediators for cancer thermotherapy and selective separation and detection of bio-molecules [1-3]. The synthesis of tailored magnetic nanoparticles (MNPs) with bio-active surfaces rely on two major approaches: **(i)** non-covalent approaches, such as the biotin-streptavidin technology or substrate passive adsorption [4-5] and **(ii)** covalent approaches, based on the formation of more stable, covalent connections between hydroxyl groups on the nanoparticle surface and a suitable anchoring agent present in a specific position of the target molecule [6-7]. Although the specificity of the latter approach improves the quality of hybrid nanoparticles, it suffers from the necessity to affect a great deal of complicated and hard-working surface modifications, which is often impracticable with complex bio-molecules such as proteins, carbohydrates, antibodies or cell-targeting agents. In many areas of pharmaceutical research such as drug delivery and nanomedicine, targeting moieties, drugs and imaging agents need to be integrated to nanoscale delivery vehicles for the convenience of detection and evaluation. These are very tedious tasks as there are many constraints on performing a successful bio-conjugation. Such reactions preferably require water-based solvents and mild conditions so that biologicals and other fragile structures present will not be denatured. In addition, protections and deprotections need to be considered in order to avoid any unwanted side-reactions and non-specific targeting within the biological system under consideration. The selectivity of a bio-conjugation process can be considerably improved by attaching a ligand to the nanoparticle, where the ligand includes a functional portion that is capable of forming an irreversible bond with an object at a site, complementary and chemoselective to the functional portion.

As already discussed in **Chapter 1**, the "click chemistry" concept, introduced by Dr. Barry Sharpless in 1999 refers to a group of reactions that are fast, environment-friendly, simple to use, easy to purify, versatile, regiospecific, and give high product yields [8]. While there are a number of reactions that fulfill the aforementioned criteria, the Cu (I) catalyzed Hüisgen 1, 3-dipolar cycloaddition of azides and terminal alkynes (CuAAc reaction) has emerged as the frontrunner. Structural modification of biologicals with azide and alkyne groups is quite simple; no protection-deprotection chemistry is involved in this reaction. With a fast,

complete conversion and almost 100% selectivity for the 1, 4-disubstituted 1, 2, 3-triazole, structural uncertainties do not exist, rendering purification unnecessary. It should however be remembered that click chemistry with its unique features (viz. chemical orthogonality, aqueous efficiency and applicability for diverse substrates) does not replace the existing bio-conjugation strategies but rather it complements and extends them. An intelligent combination of "click chemistry" with classical bio-functionalization approaches can effectively cut short the time-consuming, multi-step reactions, commonly involved in the preparation of multifunctional nano-bio-hybrids and simultaneously improve the selectivity of bio-conjugation.

Although click-reactions have become a burgeoning strategy to generate functionalized polymers, engineered surfaces and nanoparticles, application of the same to the development of multifunctional, theragnostic MNPs is still in the age of infancy. Chemoselective synthesis of folic acid (FA) decorated magnetite (Fe_3O_4) nanoparticles (NPs) via click reaction between azide-functionalized Fe_3O_4-NPs and alkyne bound folate has been reported by Hayashi et al [9]. However, azide functionalization of MNP surface, starting from an iron (III) allylacetylacetonate (IAA) precursor was accomplished through multistep reactions, which involved reductive hydrazinolysis of IAA, followed by sequential N-bromosuccinimide (NBS) mediated transformation of the terminal double bond to a bromohydrin intermediate and nucleohilic substitution of the bromo (-Br) function by an azide ($-N_3$) function. The reagents and reaction conditions chosen lead to a number of side products including α-bromo ketones and dibromo derivatives and therefore, has to compromise with the yield and selectivity of the final product formation. Similar problems arise, while synthesizing the alkyne functionalized folate intermediate using a Stouten Baumann reaction between the primary amine groups of FA and 2, 3-dibromopropionyl chloride (DBPC), followed by alkali mediated dehydrohalogenation. The low nucleophilicity of the primary amine group on the pteridine ring does not ensure very quantitative transformation of the FA precursor to its corresponding amide derivative; moreover in presence of a strong base like KOH, both γ or α carboxyl groups of the glutamic acid moiety in FA is susceptible to deprotonation and can actively participate in a Schotten Bauman reaction with DBPC, thus leading to the formation of mixed anhydrides as undesired side products. More recently, Santra et al. have synthesized multimodal, folate-decorated iron-oxide nanoparticles (IONPs) by clicking an azido-functionalized folate onto the surface of propargyl derivatized poly-acrylic acid (PAA) coated IONPs. By co-encapsulating a lipophilic near infrared (NIR) dye and an anticancer drug (Paclitaxel) within hydrophobic pockets in the polymeric matrix of FA-functionalized PAA-

IONPs, the authors have come up with a theragnostic, nanoformulation for combined optical/magnetic resonance imaging and cancer-targeted therapy [10]. Although the system shows a very good response in vitro, in order to ensure maximal efficiency in-vivo, covalent bonding of drugs on nanoparticles is preferred rather than their physical encapsulation within the polymeric matrices. To incorporate stimuli-responsive drug release characteristics, pH-sensitive amide, ester or hydrazone linkages are usually chosen so that while the bond strength makes the NP-drug conjugates highly stable under normal physiological conditions, the drug is susceptible to facile cleavage from the NP surface under harsh environments inside the lysosomes. The motivation of the present work thus stems in from the need to develop "smart", tailored MNPs with mixed surface functional groups, amenable to chemoselective conjugation with multiple diagnostic and therapeutic entities.

Herein, we describe a novel approach towards the synthesis of a multifunctional, theragnostic nanoplatform for combined cancer-targeted therapy and multimodality imaging, combining a unique collage of classical bio-conjugation strategies with surface diazo transfer and "click chemistry". The target multifunctional nanohybrid comprises of four key components, which include: **(i)** a nanomagnetic core, modified with a biocompatible coating of 2 aminoethyl-phosphonic acid (APA) to allow magnetically guided drug delivery as well as T_2 weighted MR contrast enhancement **(ii)** a fluorescent dye viz. rhodamine B isothicyanate (RITC) to allow optical imaging **(iii)** a cancer targeting molecule viz. folic acid (FA) to target the folate-receptor (FR) over-expressed cancer cells and **(iv)** a chemotherapeutic drug viz. Paclitaxel (PTX) to act as a mitotic inhibitor. Designed fabrication of magneto-fluorescent nanohybrids, surface-functionalized with mixed azide and carboxyl groups was undertaken to simultaneously allow **(i)** "click" immobilization of alkyne-derivatized bio-molecules on the surface through hydrophilic and biocompatible triazole formation and **(ii)** covalent immobilization of amine or alcohol-containing bio-molecules through carbodiimide promoted amide or ester formation, on a common platform. Such a unique surface design allows a fast but highly controlled, chemoselective functionalization of the superparamagnetic nanocore with multiple diagnostic and therapeutic entities. For the first time, a biocompatible, multimodal and theragnostic formulation has been developed using magnetofluorescent, mixed azide and carboxyl terminated, heterobifunctional magnetite nanoparticles as a synthon. The mild, water-based synthesis process is simple, amenable to scale up and contributes a new toolbox for the chemoselective bio-functionalization of inorganic nanoparticles, efficiently addressing the lacuna, associated with the preparation of hybrid nanoparticles with tailored, bioactive surfaces.

4. 2. Materials and Methods

4.2.1. Materials

$FeCl_3$ and $FeSO_4$ were obtained from Merck, Germany as already mentioned in the previous chapters. Folic acid (FA), Dicyclohexyl carbodiimide (DCC), *N*-hydroxysuccinimide (NHS), 1-[3-(Dimethylamino) propyl]-3-ethylcarbodiimide hydrochloride (EDC), Propargyl amine, Triflic anhydride (Tf_2O), sodium azide (NaN_3), Copper sulphate pentahydrate ($CuSO_4.5H_2O$), Sodium ascorbate, Rhodamine (B) isothiocyanate (RITC), Paclitaxel, MTT [3-(4,5-dimethylthiazol-2-yl)-2,5-diphenyltetrazolium], Propidium iodide (PI), RNase A, Trypsin, 4′,6-diamidino-2-phenylindole dihydrochloride (DAPI) and agarose were purchased from Sigma Chemical Co. (St. Louis, MO, USA). Commercially available dimethyl sulphoxide (DMSO) and triethyl amine (Et_3N) were distilled prior to use. The cells cultivated for *in vitro* experiments were human cervix adenocarcinoma, HeLa and human osteosarcoma, MG-63 cell lines, obtained from the National Centre for Cell Sciences (NCCS) Pune, India.

4.2.2. Synthesis Methodology

4.2.2.1. Synthesis of triflic azide from triflic anhydride

Triflic azide was synthesized from triflic anhydride according to a reported protocol [11] with minor modifications. In brief, toluene (2 ml) was added to an aqueous solution (2 ml) of sodium azide (545 mg, 8.38 mmol) and the resultant mixture was cooled to 0°C under vigorous stirring. Following the dropwise addition of triflic anhydride (896 µL, 4.19 mmol) and further vigorous stirring for 30 min at 0°C, the temperature was raised to 10°C and the biphasic mixture was stirred for 2 h. A saturated aqueous solution of sodium hydrogen carbonate was added dropwise until gas evolution had ceased. The two phases were separated and the aqueous layer was extracted with toluene (2 × 2 mL). The combined organic layers were used in the subsequent diazo transfer reactions.

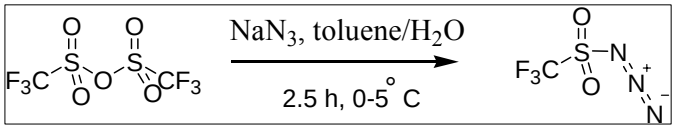

Scheme 5.1: Synthesis of triflic azide from triflic anhydride

4.2.2.2. Synthesis of folic acid alkyne derivative

Alkyne derivative of folic acid was prepared according to previously reported literature procedures [12] with minor modifications. Although folic acid has two –COOH groups at α and γ positions, which can act as handles for covalent attachment, it has already been verified that in folic acid γ -COOH is more prone to this reaction due to its higher reactivity.

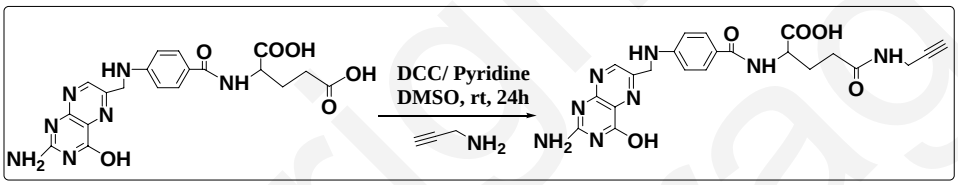

Scheme 5. 2: Synthesis of propargyl folate

Folic acid (1 mmol) was reacted with DCC (1.5 mmol) in presence of pyridine and DMSO under inert atmosphere. Following carbodiimide activation, propargyl amine (1.5 mmol) was added dropwise to the reaction mixture and left to overnight stirring. The precipitated dicyclohexyl urea (DCU) was removed by filtration. The filtrate was added dropwise to ice-cold diethyl ether (Et_2O) at 0°C to precipitate out the desired propargyl-folate derivative as a yellow-orange solid product (91% yield). ^{1}H NMR (DMSO-d_6, δ ppm) 8.62 (s, PtC_7 H, 1H), 8.2-8.35 (d, PtC6-CH_2NH-Ph 1H, J=5.3 Hz), 7.95-8.1(d,-CONHCHCOOH, 1H, J=7.6 Hz), 7.6-7.65 (d, PhC_2H and Ph-C_6H, 2H, J=8.2 Hz), 6.91(br s, NH_2, 2H), 6.63-6.61(d, Ph-C_3H and Ph-C_5H, 2H, J=8.4 Hz), 4.49–4.48 (d, PtC_6-CH_2NH-Ph, 2H, J=5.6 Hz), 4.32-4.45(d, PtC_6-CH_2NH-Ph), 3.8 (m,-CONH-CH_2CCH, 2H) 3.8 (m,-CONH-CH_2CCH, 2H), 3.1 (t, -CONH-CH_2CCH, 1Hz, J=2.6 Hz), 2.5 (s,-CONH-CH_2CCH, 1H), 2.52 (br s, -OH,1H), 2.3(m, $-CH_2CO_2H$, 2H), 2.07 (m, $-CHCH_2CH_2$, 1H)1.7 (m, $-CHCH_2CH_2$, 1H). FTIR (KBr, cm^{-1}): 2369 (CC), 1718 (C=O), 1607 (CONH), 1508 (C=C), 1298, 1191 (C−O−C), 1127, 840, 626 (C−C). Mass (ES+) 479 (MH+).

4.2.2.3. Synthesis of MNP 1

MNP 1 was synthesized according to the procedure adopted in **Chapter 2** for the synthesis of 2-aminoethyl phosphonic acid (APA) grafted magnetite nanoparticles. Although this material is chemically identical with the bio-conjugating precursor used in our earlier work, typically optimized for the generation of hybrid surface proposed at the beginning of this chapter, a different ratio of iron-oxide (1 mmol) to phosphonic acid (0.25 mmol) was used. The amine grafting density, achieved with the present iron-oxide to phosphonic acid concentration ratio was high enough to ensure an optimal concentration of carboxyl and azide groups on the nanoparticle surface amenable to chemoselective ligation with an optimal concentration of the functional ligands required to attain the desired chemotherapeutic/diagnostic effect *in vitro.* The protocol adopted for RITC labeling is same as described in the earlier chapters.

4.2.2.4. Synthesis of MNP 2

The transformation of **MNP 1**-**MNP 2** was executed via dessymetrization of the primary amine functions on RITC-labeled **MNP 1** to mixed carboxyl and azide functionalities through a sequence of **(i)** controlled, ring-opening linker elongation reaction with succinic anhydride and **(ii)** high yielding Cu (II) catalyzed diazo transfer reactions with triflic azide. In brief, succinic anhydride (0.2 mmol) was added to an ultrasonicated suspension of **MNP 1** (200 mg, surface amine density ~1.56 μmol/mg) in anhydrous, distilled DMSO. The pH of the reaction mixture was adjusted to 8 by adding a few drops of succinic anhydride and left to stirring for 24 h. Hybrid MNPs containing both amine and carboxyl groups were thoroughly washed with distilled water and finally isolated through magnetic decantation. An aqueous suspension (20 ml) of partially succinylated MNP 1 (100 mg) was added to a freshly prepared solution of triflic azide, pre-activated with $CuSO_4$ (catalytic amount) and triethyl amine (0.5 mmol). Methanol (2 ml) was added to the reaction mixture and the suspension was left to stirring at room temperature. After 12 h, the reaction mixture was divided into two parts: a part was separated through magnetic concentration, washed thoroughly with de-ionized water and freeze-dried for surface characterizations while the other part was used in the subsequent steps without further isolation.

4.2.2.5. Synthesis of MNP 3

The click reaction was performed in the same pot as the Cu (II) catalyzed diazo transfer. Cu (II), which is used as catalyst in the previous step can also catalyze the click reaction through generation of Cu (I) in presence of sodium ascorbate. In brief, sodium ascorbate (catalytic amount) was added to the suspension of **MNP 2**. Alkyne derivative of folic acid (0. 25 mmol) was dissolved in DMSO-H_2O mixture (1:1) and the reaction mixture was stirred for 8 h. The "clicked" MNPs (**MNP 2**) were thoroughly washed with a 40% solution of ammonia, followed by repeated washing with distilled water to completely free the nanoparticles from Cu (II). The nanoparticles were finally washed with acetone, separated via magnetic decantation, freeze-dried and used for subsequent conjugation with Paclitaxel (PTX).

4.2.2.6. Synthesis of MNP 4

Paclitaxel was conjugated with **MNP 3** via carbodiimide promoted esterification between the hydroxyl groups of PTX and surface-pendant carboxyl groups. In brief, an ultrasonicated suspension of **MNP 3** (5 mg, surface carboxyl density ~1.63 μmol/mg) in DMSO (5 ml) was activated with EDC (0.0075 mmol). A few drops of Et_3N were added to maintain the solution pH at around 8. A solution of PTX (0.005 mmol) in DMSO (1ml) was added to the resultant mixture and left to overnight stirring at room temperature to afford the target construct. The resulting conjugate (**MNP 4)** was thoroughly washed with distilled water, acetone and finally isolated using a rare earth magnet.

4.2.3. Characterizations

As-prepared MNPs were extensively characterized in terms of size, charge, surface-chemistry, magnetization and magnetorelaxometry according to the procedure as described in the earlier chapters. For a detailed structure-resolved analysis of the surface-bound ligands high resolution magic angle spinning (HR-MAS) nuclear magnetic resonance (NMR) experiments were pursued. Samples for MAS experiments were prepared by suspending 10 mg of each nanoparticle preparation in a 1:1 mixture of DMSO-d_6: D_2O (500 μL). HRMAS–NMR analysis was carried out with a 400 MHz FT-NMR spectrometer (Avance 400), equipped with a 5 mm HRMAS probe. For authentication of PTX immobilization on the surface of **MNP 4**, the as-prepared conjugate (~50 mg) was incubated with porcine liver

esterase (PLE) at pH 8 for 48 h to ensure complete detachment of the drug molecules from NP surface. The hydrolysis solution was partitioned between chloroform and water, following which the organic layer was dried over sodium sulphate, concentrated in vacuum and finally subjected to FTIR and NMR analysis. The data was authenticated by comparison against standard FTIR and NMR data for pure paclitaxel.

4.2.4. Total iron determination and quantification of functional molecules on NPs

Iron concentration in the as-prepared formulations was determined spectrophotometrically as described in the **Chapter 3.** The determination of amino groups on the surface of **MNP 1** was performed using the 2,4,6-trinitrobenzenesulfonic acid (TNBS) method according to the procedure already discussed in **Chapter 2, Section 2.4.3.2.** The transformation of **MNP 1** to **MNP 2** was tracked by monitoring the systematic reduction in amine density on the surface of nanoparticles, determined via the TNBS assy. The average number of RITC, FA and PTX molecules immobilized per particle was determined spectrophotometrically as described in the earlier chapter. For quantifying the amount of PTX immobilized on the surface of MNPs, absorbance was recorded at 227 nm. From this analysis, the amount of RITC, FA and PTX immobilized per unit mass of MNPs was calculated to be around 0.0369, 0.259 and 0.127 μmol/ mg respectively. Since each particle contains magnetite (d = 5.214 g cm^{-3}) with an average radius of 4.5 nm, the average volume and mass of Fe_3O_4 particles are 3.8151×10^{-25} gm/ m^{-3} and 1.987×10^{-18} respectively. Hence, 1 mg of Fe_3O_4 contains 5.032×10^{14} particles. From these values, the average number of RITC, FA and PTX immobilized per particle was determined to be around 43.16, 310.56 and 152.01 respectively.

4.2.5. Drug release study

To mimic the intracellular lysosomal conditions, **MNP 4** (1 mg/ml) was suspended in a solution of crude protease (0.1 mg/ml) from bovine pancreas in phosphate buffered saline (PBS) solution (10 ml) at 37°C under constant stirring. The solution was divided into three sets and pH of the individual sets was adjusted by titration with 0.1 (M) NaOH or 0.1 (M) HCl to achieve the different pH values of 4, 5.6 and 7.44 respectively. Following incubation for 8, 16, 24 and 48 h, the nanoparticle suspensions were isolated by magnetic decantation to free the nanoparticles from cleaved PTX, protease and PBS. PTX cleaved from nanoaparticles was then quantified with UV spectroscopy at wavelength of 227 nm.

4.2.6. *In-vitro* studies

As-prepared MNPs were investigated in terms of their cell-uptake behavior, MR detectibility, cytotoxicity and apoptotic effect against folate-receptor over-expressing cancer cells according to the protocol already described in **Chapter 3.**

4. 3. Results and Discussions

The retrosynthesis of our target, presented in Scheme **4.1,** shows two important reactions: formation of a pH-labile ester bond between hydroxyl groups of PTX and carboxyl functions on the nanoparticle surface and formation of a stable, biocompatible triazole linkage between alkyne functionalized folic acid and azide-terminated nanoparticles. While the former is executable through the classical carbodiimide promoted esterification reaction, the latter, in principle, can be achieved through highly chemoselective CuAAc reaction. Further retrosynthetic analysis suggests the involvement of a mixed carboxyl and azide-terminated, bifunctional MNP intermediate, which can be synthesized from an amine functionalized nanomagnetite precursor through partial interchange of these amino functions with carboxyl functions, followed by a diazo transfer onto the remaining surface amino groups.

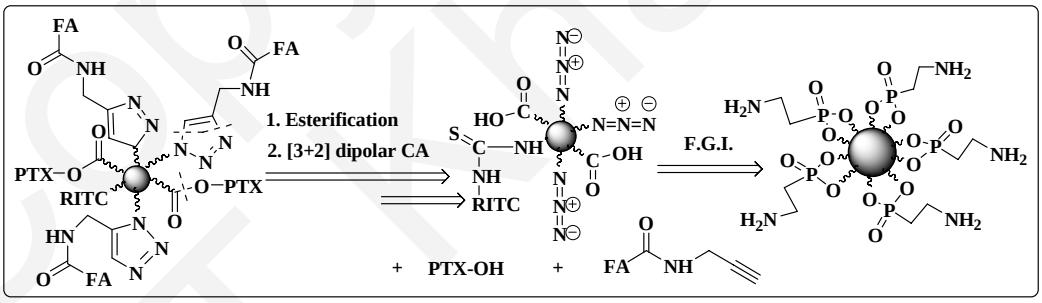

Scheme 4.1: Retrosynthesis of the target multifunctional nanohybrid

As a first step towards the synthesis of our target multifunctional nanohybrid, **MNP 1** was prepared by the post-synthetic grafting of 2-aminoethylphosphonic acid (APA) on the surface of superparamagnetic magnetite nanoparticles with average diameter around 9 nm**.** Our work was further motivated by the findings of a recent report in which Polito et al. explored the

possibility to tether bio-molecules onto azide terminated magnetic nanoparticles via triazole formation without recovering the intermediate azido derivatives [11]. We considered this strategy and applied it successfully to our **MNP 1** with necessary modifications. Magnetofluorescent analogue of **MNP 1** was synthesized as described in **Chapter 2**. The primary amine functions on RITC-labeled **MNP 1** were desymmetrized to mixed carboxyl and azide functionalities through a sequence of **(i)** controlled, ring-opening linker elongation reaction with succinic anhydride and **(ii)** high yielding Cu (II) catalyzed diazo transfer reactions with triflic azide (**Scheme 2**). Starting from **MNP 2**, we reached to our target nano-construct **MNP 4** through **MNP 3** by simply clicking propargyl folate onto the surface azido groups, followed by carbodiimide-promoted coupling of the hydroxyl (-OH) groups of PTX with surface-pendant carboxyl groups.

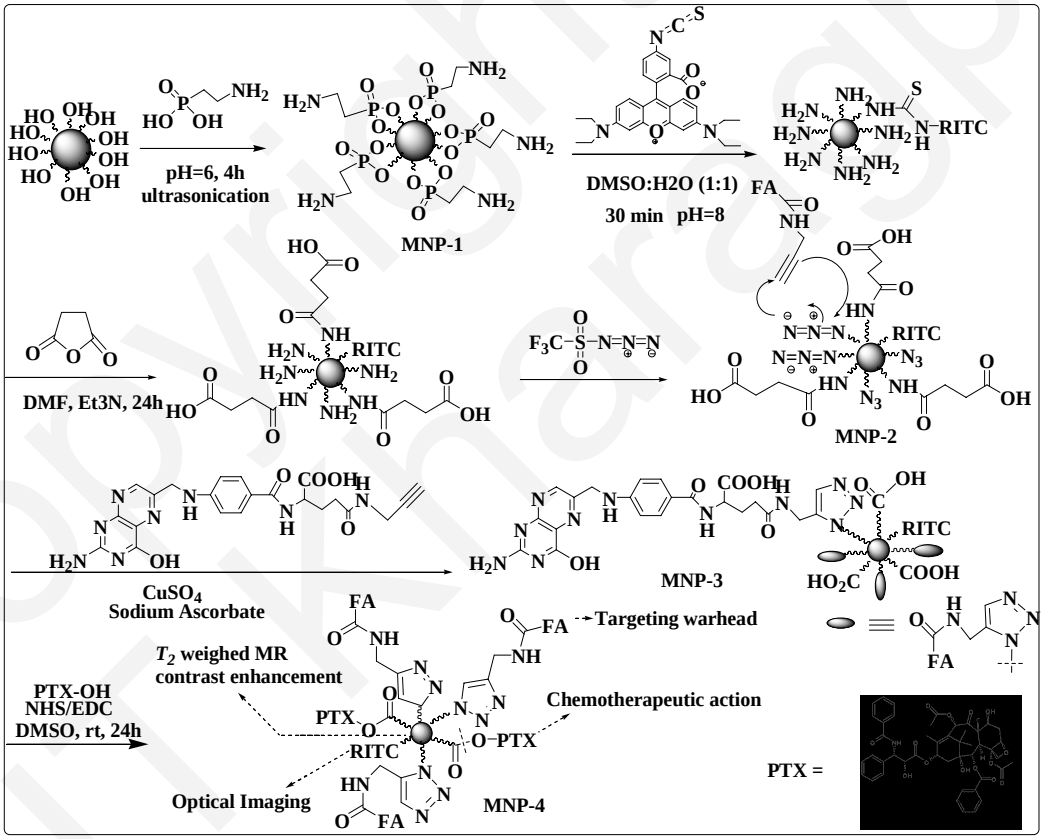

Scheme 4.2: Synthesis of the target nanoconstruct **MNP 4** via a chemoselective protocol

An extensive literature survey reveals that 2′- and 7-hydroxyl groups in PTX are the most suitable positions for structural modification. Usually, the 2′-hydroxyl, being less sterically hindered, presents higher reactivity than the 7-hydroxyl so that PTX conjugation occurs

preferentially at the 2′-hydroxyl position [14]. It is also interesting to note that the Cu (I) species, required for the Hüisgen cycloaddition reaction is generated in situ, deriving it directly from Cu (II) salts necessary for diazo transfer. In fact, the addition of sodium ascorbate after diazo transfer completion causes the reduction of Cu (II) to Cu (I), which, once formed, becomes immediately available to promote the subsequent cross-reaction with the complementary alkyne, so that, the transformation of **MNP 1-3** proceeds smoothly in a single pot, without recovering the intermediates. The extent of RITC, FA and MTX conjugation on **MNP 4** was quantified using UV visible absorbance data, as described in the earlier chapters. Assuming 5.032×10^{14} Fe_3O_4 units to be present per mg of the synthesized conjugate, the average number of RITC, FA and MTX immobilized per particle was detected to be around 43.16, 310.56 and 152.01 respectively. This concentration, however, was optimal for attaining a high targeting and chemotherapeutic efficiency *in vitro.*

Dynamic light scattering (DLS) studies of **MNP 1** confirmed the presence of stable, non-aggregated particles with a mean hydrodynamic diameter (HD) of 33±2 nm and polydispersity index (PDI) less than 0.2. The ferrofluid imparted a continuous positive charge over the entire lower pH range due to the presence of surface-exposed NH_3^+ groups. The zeta potential vs. pH curves for **MNP 2** before and after succinylation has been presented in figure **4.1.**

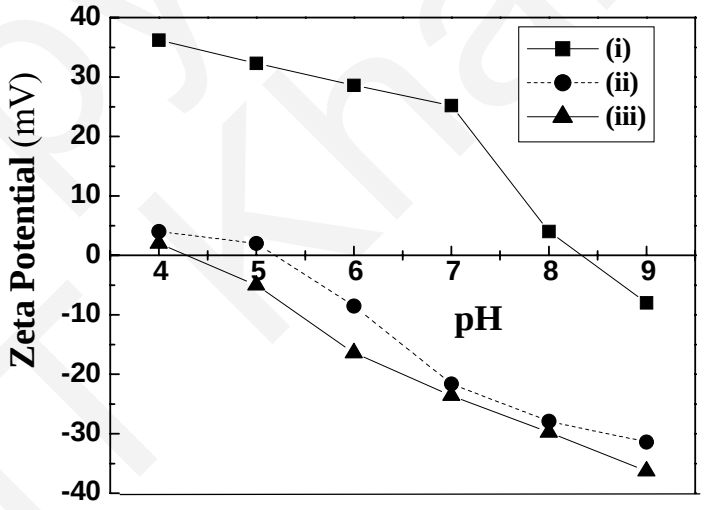

Fig. 4.1: Variation of zeta potential of **(i) MNP 1 (ii**) partially succinylated **MNP 1** and **(iii) MNP 2** (after diazo transfer) against pH

The isoelectric point (IEP) dropped markedly from 8.34 to 5.17 after succinylation, which is much higher than that expected for a quantitative conversion of amino groups to carboxyl groups upon succinylation, as the intrinsic pK_a of succinic acid is 4.26. This further implies that the amine groups on **MNP 2** were only partially succinylated. Following azido transfer, the isoelectric point further dropped from 5.85 to 4.36, attributed to the quantitative conversion of positively charged surface amine to neutral azide functions. The final conjugate, **MNP 4**, presented a mean HD of 91±4 nm (PDI = 0.191) with a surface charge of -43.4 ±2 mV at neutral pH. These functional nanoaparticles were highly stable in aqueous medium as their HD, PDI, zeta potential and T_2 relaxivity remained unaffected over a long period of time (**Table 4.1**).

Table 4.1: Stability analysis of **MNP 4**

Time (weeks)	**1**	**2**	**3**	**4**	**6**	**8**	**12**
HD (nm)	91.6	89.7	93.2	92.9	94.1	93	95
PDI	0.197	0.184	0.193	0.191	0.204	0.216	0.198
Zeta-potential (mV)	-43.4	-43.8	-41.9	-40.7	-38.6	-39.3	-37.6
r_2 ($s^{-1}mM^{-1}$)	70.79	70.96	69.74	67.35	65.66	66.79	65.8

The X-ray diffraction pattern of **MNP 1** has been shown in **Fig. 4.2.** The d values corresponded to that of inverse spinel magnetite [Fe_3O_4] (JCPDS card no. 85-1436). The broadening of peaks indicates nanocrystalline nature of **MNP 1**, which is translated into an average core size of about 9.84 nm using the Debye–Scherrer formula for spherical particles.

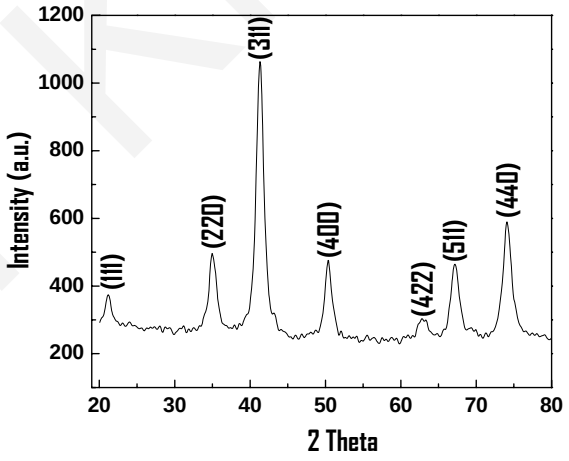

Fig. 4.2: X-ray diffraction pattern of **MNP 1**

Transmission electron microscopy (TEM) studies revealed that the as-synthesized magnetite nanoparticles were close to spherical with an average diameter of 9 ± 0.5 nm (**Fig. 4.3**)**.** The selected-area diffraction (SAED) pattern (inset image) indicated the polycrystalline nature of the embedded magnetite particles. The individual planes identified from the SAED pattern correlated well with that of the XRD pattern. Representative TEM images of **MNP 3-4** indicated the presence of nearly spherical particles, each constituting a black central core, surrounded by a light grey-corona, probably arising from the organic functionalization, associated with each particles. The overall particle diameter was between 10-20 nm, while the embedded nanocrystals were between 5-10 nm. The "clicked" MNPs displayed much better dispersancy, as compared to their amine-functionalized precursor (**MNP-1**), probably due to the presence of highly hydrophilic triazole moiety and the deprotonated carboxyl and hydroxyl groups of FA and PTX respectively, at neutral pH and physiological salinity.

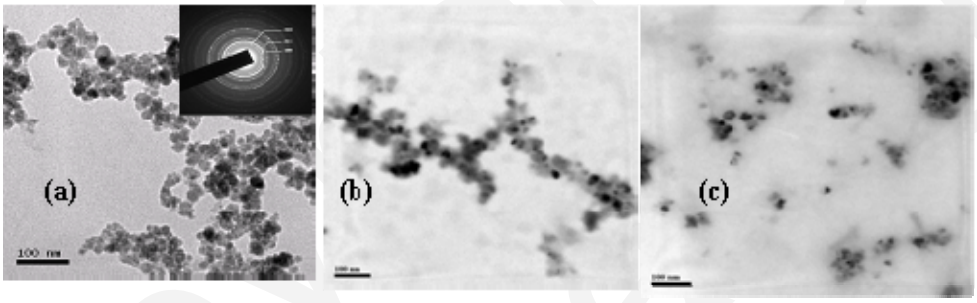

Fig. 4.3: Transmission micrograph of **(a) MNP 1** (SAED pattern shown as inset) **(b) MNP 3** and **(c) MNP 4**

The FTIR spectrum of **MNP 1** (**Fig. 4.4**) displays a strong band around 594 cm^{-1} attributed to the Fe-O vibration related to the magnetite core. The observed red-shift, as compared to bare magnetite is due to the chemisorption of APA on the nanomagnetite surface. As compared to unbound APA, large changes are observed in the P=O stretching region between 1200-900 cm^{1} present. A broad band, associated with the overlapping of Fe-O-P and P=O stretching appears between 1160-928 cm^{-1}, which unambiguously suggests that a strong interaction between the phosphonate head-group and Fe_3O_4 surface is present. The band at 1633 cm^{1}, associated with –NH bending (scissoring) vibration however testifies to the successful modification of magnetite surface by primary amine groups. Chemical treatment of these surface amine groups with succinic anhydride (approximately in 3:1 molar ratio) led to the partial interchange of these amine functions with carboxyl functions. The typical vibrations of

–CO_2H group (1704 cm^{-1}) and the amide linkage [1637 cm^{-1} (amide I) and 1556 cm^{-1} (amide II)] appeared in the corresponding FTIR spectrum, which evidences the successful derivatization of the surface-amino group with succinic anhydride. It should however be noted that the intensity of the –CO_2H vibration at 1710 cm^{-1} is relatively weak, which is possibly a consequence of intraparticle hydrogen bonding between the surface –CO_2H groups. This however shifts the >C=O stretching bands of carboxylic acids to a much lower wave number (~1625-1650 cm^{-1}) and superimposes with the amide I band. As a consequence of diazo transfer, an extra band appears in the FTIR spectrum of **MNP 2** at the range of 2041 cm^{-1} due to the asymmetric stretching of the N=N=N bond of the azide group. The successful immobilization of FA on **MNP 2** is indicated by the disappearance of 2041 cm^{-1} band and concomitant appearance of the characteristic bands of FA at 1603 and 1656 cm^{-1}. After PTX conjugation, the only distinguishable change in the spectrum was the appearance of a weak but distinct band at the range of 1736 cm^{-1}, possibly associated with C=O stretching vibrations arising out of the covalent attachment of PTX to the carrier surface via an ester linkage. As already discussed in **Chapter 3**, the relatively weak intensity of the ester stretching frequency might be a consequence of multiple ligand attachment on the nanoparticle surface. In such cases precise characterization becomes difficult because the analysis is being carried over solid phase samples, which are coated with only a small amount of these small molecules [15]. The surface of MNPs being shared by multiple functional molecules, relative fraction of individual functional entities associated with the nanoparticle surface may be lower than the detection limit of the available spectroscopic techniques.

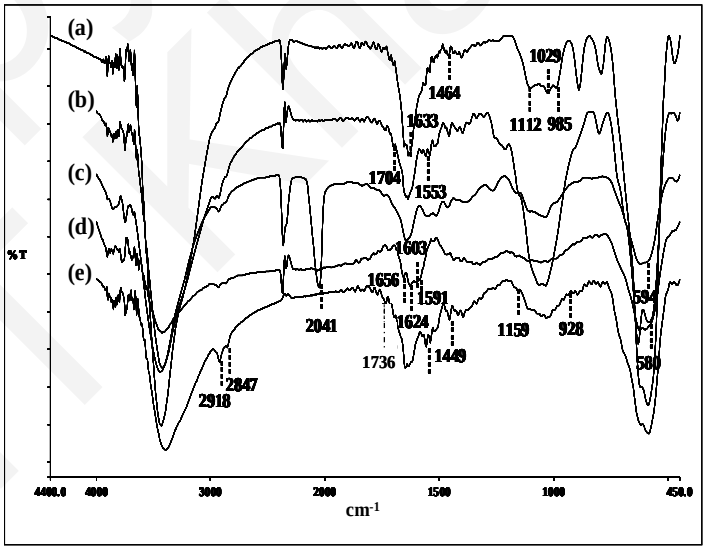

Fig. 4.4: FTIR spectra of **(a) MNP 1 (b)** partially succinylated **MNP 1 (c) MNP 2 (d) MNP 3** and **(e) MNP 4**

The successful transformations of **MNP 1** to **MNP 3** via partial succinylation, surface diazo transfer and CuAAc reactions were also studied using XPS analysis. The high-resolution N1s spectrum of APA functionalized nanoparticles (**Fig. 4.5**) reveals a broad shoulder at 398.6 eV corresponding to the free amino groups on the surface. At the ring opening linker elongation step, the intensity of the -NH_2 peak gradually diminishes with concomitant appearance of a new peak at 400.6 eV, indicating the formation of amide (-NHCO) linkage between the amine groups of APA and succinic anhydride. A high-resolution spectrum of the nitrogen 1s binding energies of **MNP 2** reveals two distinct peaks one centered at around 400 eV and another at 405 eV, with approximately 2:1 ratio of the peak areas. The relatively lower intense, higher energy, 405 eV peak is unusual for organic nitrogen, and this peak can be assigned to the central, electron-deficient nitrogen in the azide group.

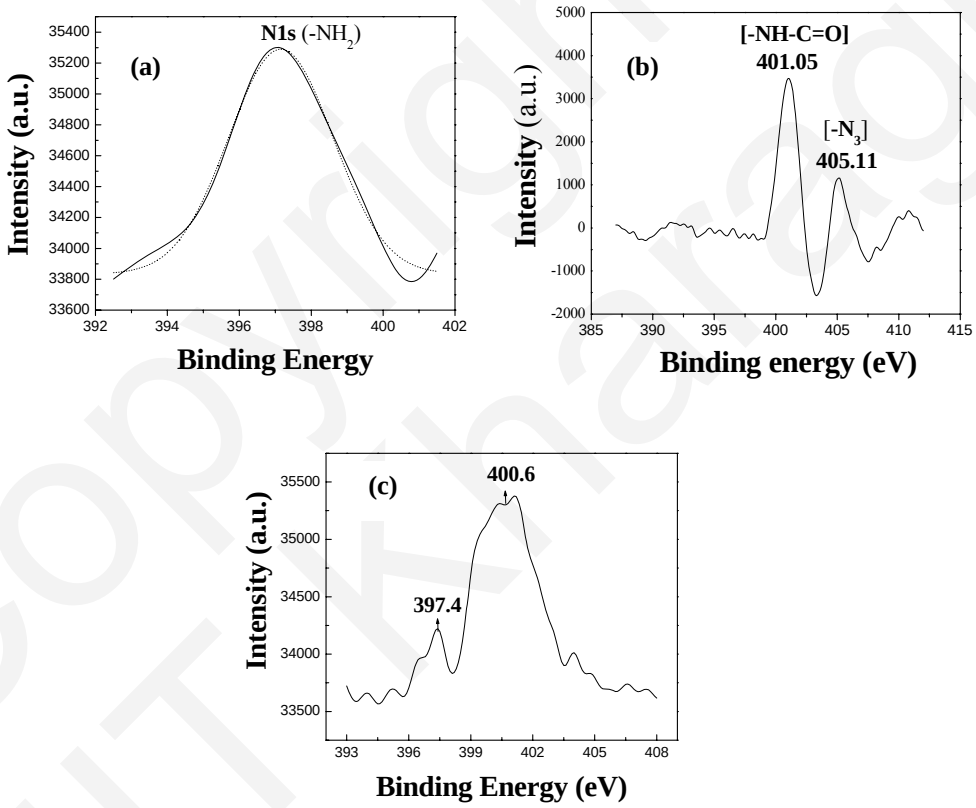

Fig. 4.5: High resolution N1s spectra of **(a) MNP 1 (b) MNP 2** and **(c) MNP 3**

Reaction of **MNP 2** with the propargyl folate, linked via the click reaction, reduced the 405 eV peak to the level of noise. The nitrogen 1s signal at 400 eV broadens, indicating the presence of chemically distinct nitrogen atoms corresponding to the nitrogen atoms of the

triazole linkage and amide bonding inside FA structure and partially succinylated surface amine functions as well. Assuming that the azide disappearance is correlated only to product formation, this provides additional evidence that the transformation is nearly quantitative [16].

In general, ^{1}H NMR spectroscopy of ligands, bound to paramagnetic nanocrystals are difficult to perform because of large broadening effects, caused by paramagnetic features. Recently, Polito et al. have explored the possibility of using the high resolution magic angle-spinning (HRMAS) technique for the fine-structure-resolved characterization of even complex organic molecules bound to paramagnetic nanocrystals, such as nanosized iron oxides, while minimizing the effect of paramagnetic broadening. In line with Polito's approach, we tried to apply the HRMAS technique for further detailed structure-resolved analysis of the organic layer, associated with our multifunctional nanoconjugate. A comparison of the ^{1}H NMR of **MNP 1**, **MNP 2** and **MNP 3** unambiguously confirmed the presence of FA on **MNP 3**, as indicated by characteristic signals from pteridine ring proton (δ 9.2 ppm) and aromatic protons of the PABA moiety of FA (δ 8.1-7.9 ppm and 7.3-6.9 ppm), which, however were absent in **MNP 2** (**Fig. 4.6**). The presence of a prominent peak at 8.2 ppm in the NMR spectrum of **MNP 3** due to the triazole proton further testified to the successful end-functionalization of **MNP 2** via 1, 3 dipolar cycloaddition.

Careful inspection of these ^{1}H HRMAS NMR spectra revealed that the spectral intensity of a proton was directly proportional to its distance from the nanoparticle surface i.e. longer the distance stronger is the intensity. For example, the intensity of the triazole proton as well as aromatic protons of FA was disproportionally higher than the methylene protons of FA and phosphonic acid, lying in close proximity with the NP surface. The observation, however, is in close accordance with some of the earlier reports [15, 17] and is attributed to **(i)** the restricted motion for protons closer to the MNP surface **(ii)** heterogeneity caused by MNP surface features (terraces, edges or vertices) of various sizes or facets and **(iii)** spin-spin relaxation (T_2) broadening effect, which also depends on NP sizes. In case of **MNP 4**, overlapping of aromatic protons of FA and PTX caused an inherent broadness in the spectrum between δ 9.8-7.3 ppm and also in the lower aliphatic range. Consistent with the findings of FTIR, spectral intensity of some of the key peaks of FA as well as PTX were too low to make a definitive structural assignment. To confirm the successful immobilization of PTX on MNP surface, we relied on an alternative strategy, which consisted of detachment of PTX from the surface of **MNP 4** through a base-catalyzed ester hydrolytic cleavage, followed by a mini work up and subsequent characterization of the organic layer by FTIR and NMR analysis.

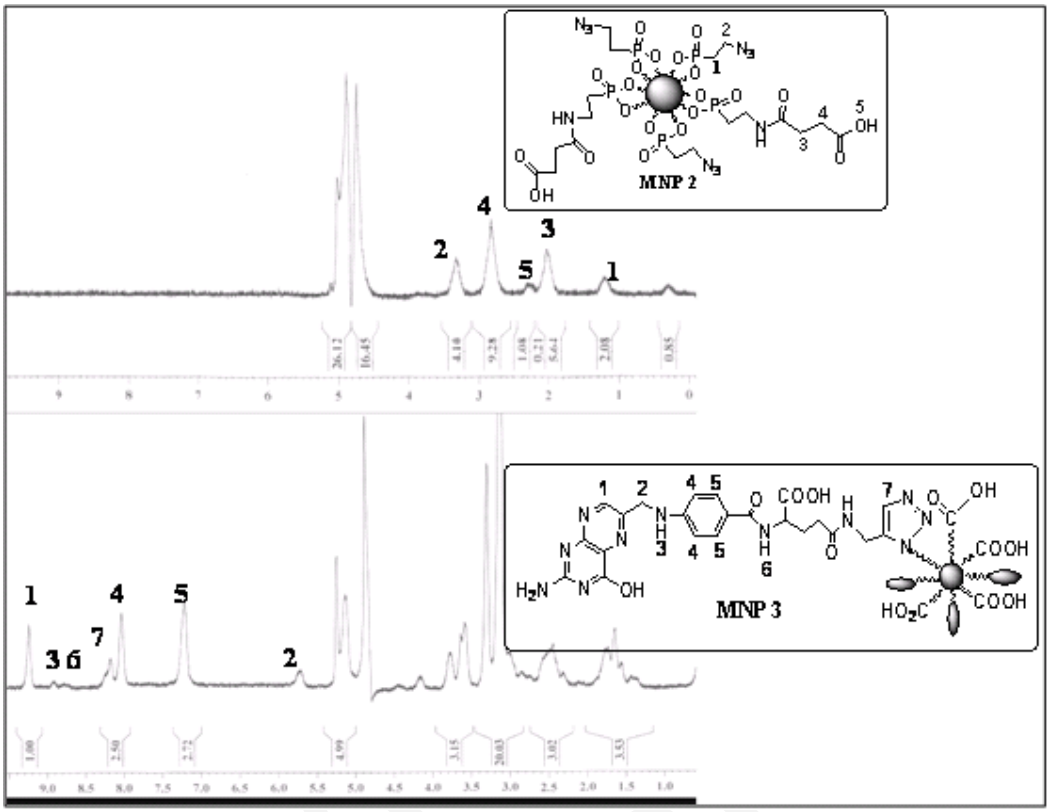

Fig. 4.6: Structure-resolved analysis of "clicked" MNPs using HRMAS-NMR spectroscopy

To further demonstrate the potential biomedical applications of the synthesized functional **MNP 4**, we evaluated the selective uptake of **MNP 1-4** against folate-receptor over-expressing human cervical carcinoma HeLa cells. Preliminary studies using magnetically activated cell sorting (MACS) indicated that cellular uptake of the conjugates containing FA as the targeting molecule was significantly enhanced in comparison to their non-targeted control (**Fig. 4.7**). The observations demonstrate active targeting of magnetite nanoparticles through the interaction between the folate groups on nanoparticle surface and receptors of HeLa cells. With an aim to confirm the receptor-specificity for the conjugate, the uptake of **MNP 1-4** by HeLa cells was compared with the uptake by **(i)** folate-receptor negative human osteosarcoma, MG-63 cell-line and **(ii)** HeLa cells, preincubated with free folate. As internalization of the folate functionalized NPs was nominal in both cases, we corroborated the receptor mediated internalization of our folate decorated MNPs.

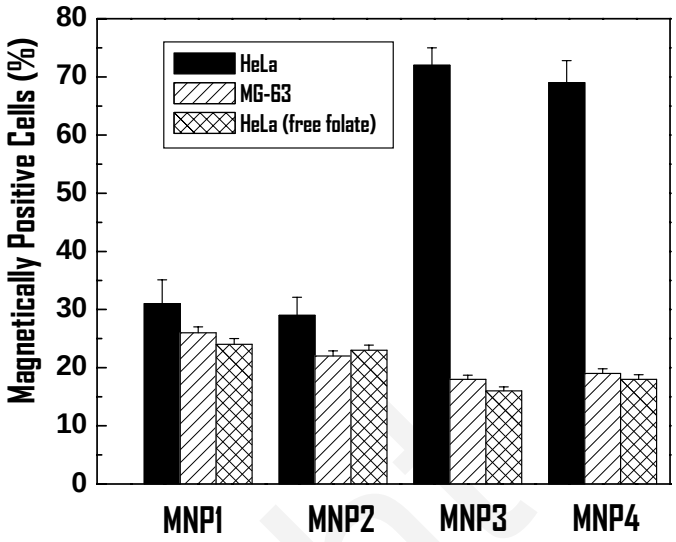

Fig. 4.7: Quantification of **MNP** uptake by FR positive HeLa, FR negative MG-63 cell lines and HeLa cells incubated with free folate via magnetically active cell-sorting (MACS) analysis.

To further evaluate the detectibility of **MNP** internalized cells by MRI and confirm their association with FR-over-expressing HeLa cells, MR phantom samples were prepared by suspending HeLa cells incubated with MNP **1-4** for two hours in agarose. The T_2 weighed phantom image of cells, incubated with MNP **3-4** showed a significant negative contrast enhancement in comparison to their non-targeted control **MNP 1**, suggesting effective nanoparticle internalization inside the target cells [**Fig. 4.8].**

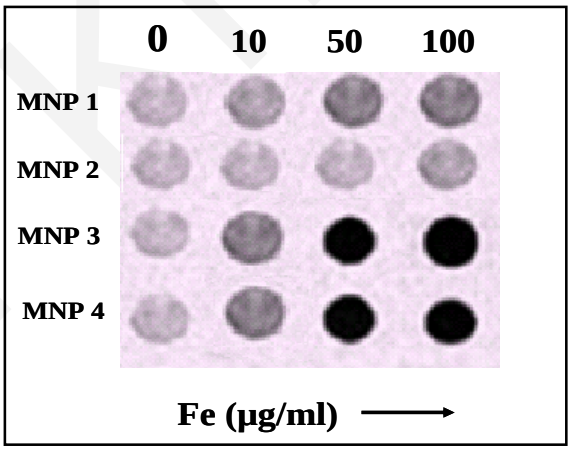

Fig. 4.8: T_2-weighted spin-echo MR phantom images of HeLa cells incubated with 0-100 µg/ml of **MNP 1-4** for 2h.

Slight loses in signal intensity were however observed for HeLa cells incubated with **MNP 1**, when compared to blank cells cultured without nanoparticles, attributed to some non-specific internalization of these nanometer-sized particles inside the target cells. The relative relaxation times of **MNP 1-4** were quantified through T_2 weighted spin-echo MR images. **Fig. 4.9** shows the T_2 relaxation time as a function of particle concentration in cell-culture media. HeLa cells cultured with **MNP 3-4** had a shorter T_2 relaxation time (higher relaxivity) than **MNP 1-2**, due to enhanced magnetism, which resulted from higher uptake of the former by HeLa cells in comparison to the latter. All these results unequivocally establish the potential of our as-prepared nanoformulation as a cancer-targeted, MR imaging probe.

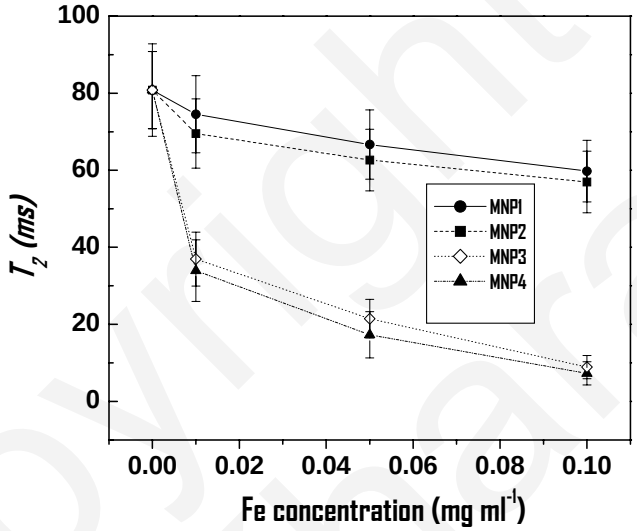

Fig. 4.9: T_2 relaxation analysis of HeLa cell suspensions magnetically labeled with **MNP 1-4**

In vitro drug release experiments, conducted with **MNP-4** under different pH conditions (pH 2.0-7.4) showed a typical release profile i.e. a rapid release rate in the beginning, followed by a sustained release pattern (**Fig. 4.10**). The overall release rate was much higher in the lower pH range (pH 4-5) and negligible drug release was observed at physiological pH. This pH-dependant release behavior suggests that PTX will be released more in acidic tumor sites than in the normal tissues. When the particles are internalized inside the cells through FR mediated endocytosis, the decreased pH values may induce further accelerated release inside the acidic endosomes of tumor cells.

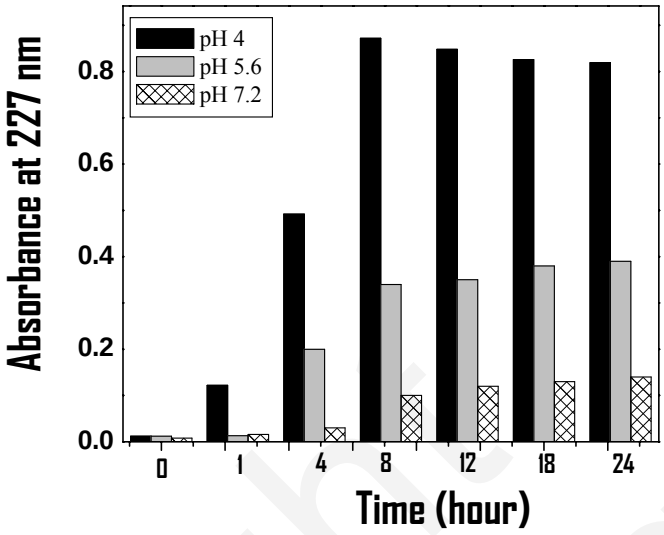

Fig. 4.10: pH-dependant drug-release behavior of **MNP 4** under typical lysosomal conditions. Highest absorbance is observed at pH 4 whereas drug release at physiological pH is negligible. This pH-dependant release behavior suggests that PTX will be released more in acidic tumor sites than in the normal tissues.

To test the efficacy of PTX cleavage inside the target cells, HeLa cells were cultured with **MNP 1-4** and free PTX in a FA deficient medium. Nanoparticle-induced cytotoxicity was determined by the MTT assay. While nanoparticles deprived of PTX were shown to be non-cytotoxic, both **MNP 4** and soluble PTX reduced the cellular viability in a time and dose-dependant fashion, establishing the ability of the cells to cleave PTX inside the acidic tumor endosomes (**Fig. 4.11**). Cells exposed to drug modified NPs demonstrated a notable downward trend in viability, following 8 h in culture. It was further observed that for concentrations of PTX grafted nanoparticles at or higher than 0.005 mg/ ml, the cells showed a statistically equivalent reduction in cellular viability. The ability of these drug modified nanoparticles to induce significant cytotoxicity in such low concentrations promises desired chemotherapeutic effect into the target site in very low dosages.

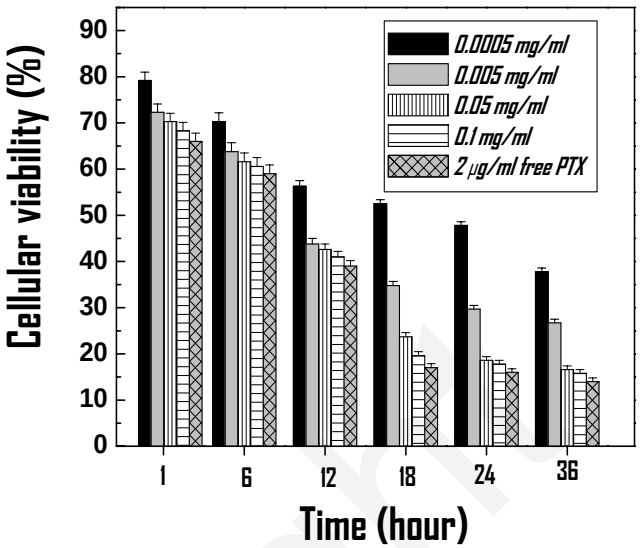

Fig. 4.11: Reduction in viability of HeLa cells as a function of time and nanoparticle concentration in culture medium.

To verify whether **MNP-4** could induce cell-death through the initiation of apoptosis, HeLa cells were exposed to 1.0 mg/ml of **MNP 1-4** for 0.5 h, washed to remove the non-internalized nanoparticles, incubated at 37°C for 24 h and subsequently visualized using fluorescence microscopy. Results showed little or practically no internalization of the non-targeted controls **MNP 1-2**, as expected. On the contrary, intense red fluorescence was detected in the cytoplasm of cells treated with the folate targeted nanoparticles, demonstrating cellular internalization through receptor mediated endocytosis [**Fig. 4.12 (a-c)].**

With an aim to examine the nuclear morphology and identify cell-death, cell-nuclei were further stained with 4'-6-Diamidino-2-phenylindole (DAPI), a nuclear staining dye known to exhibit strong blue fluorescence, when bound to DNA. As predicted from the cytotoxicity experiments, fluorescence images of HeLa cells, incubated with **MNP 1** and **MNP 3** for 12 h showed well preserved nuclear structures without any visible abnormalities. On the contrary, following hallmark features of apoptosis such as nuclear condensation, membrane blebbling and formation of apoptotic bodies were visualized in **MNP 4** incubated HeLa cells by as early as 12 h.

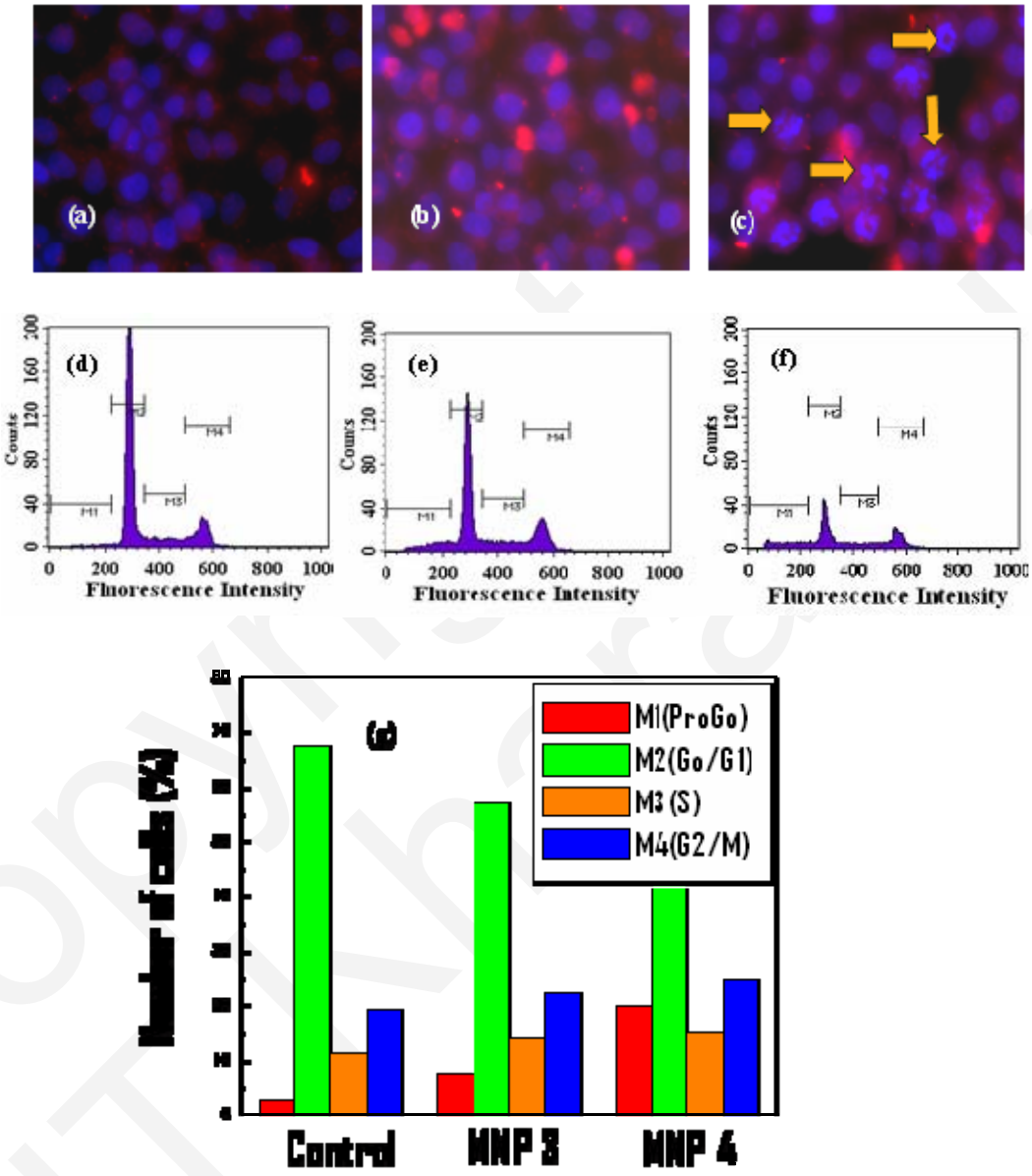

Fig. 4.12: Assessment of cellular uptake and MNP induced apoptosis in HeLa cells. **(a-c)** represents the fluorescence and T_2 weighted MR images (inset) of HeLa cells incubated with 150 μg/ml of **MNP-1**, **3** and **4** respectively for 12 h while **(d-f)** represents the corresponding DNA fluorescence histogram. The arrows in **Fig. 2(c)** denote nuclei with typical apoptotic features and **Fig. 2 (g)** represents the cell-cycle analysis using the standard PI flow cytometric assay.

A quantitative evaluation of nanoparticle induced apoptosis, using the standard propidium iodide (PI) flow cytometric assay showed that DNA fragmentation was almost negligible in case of untreated cells as well as cells treated with control **MNP 1** and **MNP 3,** within 12 h of incubation. Considerable DNA fragmentation was however envisaged in cells, treated with **MNP 4** under similar experimental conditions, evidenced as a "sub-G1" peak in the DNA fluorescence histogram [**Fig. 4.12 (d-g)].** Cell cycle analysis further established that the G_0/G_1 phase steadily decreased in function of time with concomitant elevation of the G_2/M and sub-G1 or apoptotic phase. Mitotic arrest was observed, which was responsible for the dramatic cellular morphological changes, as visualized by fluorescence microscopy and ultimately led to cell-death.

4.4 Conclusion

In conclusion, a biocompatible, theragnostic iron-oxide nanoformulation for combined cancer-targeted therapy and multimodal imaging has been designed and successfully synthesized using a chemoselective protocol. Magnetite nanoparticles with hybrid surface containing both carboxyl and azide groups were used as the bio-conjugating precursor. Such a bifunctional surface was executable through a sequence of highly controlled, partial succinylation, followed by Cu (II) catalyzed diazo transfer on APA functionalized magnetite nanoparticles. Chemoselective conjugation of cancer-targeting FA and chemotherapeutic PTX on the hybrid MNP surface was accomplished via CuAAc reactions and carbodiimide promoted esterification respectively. The feasibility of chemoselective ligation on these bifunctional MNPs was demonstrated with extensive FTIR, XPS and HRMAS-NMR analysis. *In-vitro* cell uptake, MR imaging and apoptosis studies established the feasibility of this multifunctional conjugate as a novel platform for "smart" cancer diagnosis, imaging and therapy.

References

1. Sosnovik, D. E.; Weissleder, R. Emerging concepts in molecular MRI *Curr. Opin. Biotechnol.*, **2007**, *18*, 4–10.

2. Mornet, S.; Vasseur, S.; Grasset, F.; Duguet, E. Magnetic nanoparticle design for medical diagnosis and therapy *J. Mater. Chem.*, **2004**, *14*, 2161–2175.

3. Chorny, M.; Polyak, B.; Alferiev, I. S.; Walsh, K.; Friedman, G.; Levy, R. J. Magnetically driven plasmid DNA delivery with biodegradable polymeric nanoparticles *FASEB J.*, **2007**, *21*, 2510–2519.

4. Gu, H.; Xu, K.; Xu, C.; Xu, B. Biofunctional magnetic nanoparticles for protein separation and pathogen detection. *Chem. Commun.*, **2006**, 941–949.

5. Nishimura, K.; Hasegawa, M.; Ogura, Y.; Nishi, T.; Kataoka, K.; Handa, H.; Abe, M. 4°C preparation of ferrite nanoparticles having protein molecules immobilized on their surfaces. *J. Appl. Phys.* **2002**, *91*, 8555–8556

6. Kell, J.; Simard, B. Vancomycin architecture dependence on the capture efficiency of antibody-modified microbeads by magnetic nanoparticles *Chem. Commun.*, **2007**, 1227–1229.

7. Carlesso, L. N.; Tung, C.H.; Tang, X.W.; Cory, D.; Scadden, D. T.; Weissleder, R. Tat peptide-derivatized magnetic nanoparticles allow in vivo tracking and recovery of progenitor cells *Nat. Biotechnol.*, **2000**, *18*, 410–414.

8. (a) Yoo, E. J.; Ahlquist, M.; Kim, S. H.; Bae, I.; Fokin, V. V.; Sharpless, K. B.; Chang, S. Copper-Catalyzed Synthesis of *N*-Sulfonyl-1,2,3-Triazoles: Controlling Selectivity. *Angew. Chem., Int. Ed.* **2007**, *46*, 1730-1733. (b) Rostovtsev, V. V.; Green, L. G.; Fokin, V. V.; Sharpless, K. B., A stepwise Huisgen cycloaddition process: copper(I)-catalyzed regioselective "ligation" of azides and terminal alkynes. *Angew. Chem., Int. Ed.* **2002**, *41*, (14), 2596-2599

9. Hayashi, K.; Moriya, M.; Sakamoto, W.; Yogo, T. Chemoselective Synthesis of Folic Acid-Functionalized Magnetite Nanoparticles via Click Chemistry for Magnetic Hyperthermia *Chem. Mater.*, **2009**, 21, 1318–1325.

10. Santra, S.; Kaittanis, C.; Grimm, J.; Perez, J. M. Drug/Dye-Loaded, Multifunctional Iron Oxide Nanoparticles for Combined Targeted Cancer Therapy and Dual Optical/Magnetic Resonance Imaging, *Small* **2009**, *5*, 1862-1868.

11. Titz, A.; Radic, Z.; Schwardt, O.; Ernst, B. A safe and convenient method for the preparation of triflyl azide, and its use in diazo transfer reactions to primary amines. *Tetrahedron Lett.* **2006**, 47, 2383-2385.

12. Mishra, A. K.; Chopra, M.; Jain, V. Convenient Route for Synthesis of Bifunctional Chelating Agent: 1-(*p*-aminobenzyl) ethylenediaminetetramethylphosphonic acid–Folate Conjugate (Am-Bz-EDTMP–Folate) *Chem. Lett.*, **2005,** 1098-1099.

13. Polito, L.; Monti, D.; Canava, E.; Delnevo, E.; Russo, G.: Prosperi, D. One-step bioengineering of magnetic nanoparticles *via* a surface diazo transfer/azide–alkyne click reaction sequence *Chem. Commun.*, **2008**, 621-623.

14. Deutsch, H.M.; Glinski, J.A.; Hermandez, M.; Haugwitz, R.D.; Narayanan, L.V.; Suffness, M.; Zalkow, L.H. Synthesis of congeners and prodrugs. 3. Water-soluble prodrugs of taxol with potent anti-tumor activity, *J Med Chem* **1989**, *32***,** 788–792.

15. Zhou, H.Y.; Du, F. F.; Li, X., Zhang, B.;W. Li.; Yan B. Characterization of Organic Molecules Attached to Gold Nanoparticle Surface Using High Resolution Magic Angle Spinning ^{1}H NMR *J. Phys. Chem. C*, 2008, 112, 19360–19366.

16. Collman, J. P.; Devaraj, N. K.; Eberspacher, T. P. A.; Chidsey, C. E. D. Mixed Azide-Terminated Monolayers: A Platform for Modifying Electrode Surfaces. *Langmuir* **2006**, *22*, 2457–2464.

17. Polito, L.; Colombo, M.; Monti, D.; Melato, S.; Caneva, E.; Prosperi, D. Resolving the structure of ligands bound to the surface of superparamagnetic iron oxide nanoparticles by high-resolution magic-angle spinning NMR spectroscopy. *J Am Chem Soc.* **2008**,*130*, 12712-24.

Chapter 5

Highly Water-Dispersible Amine Functionalized Magnetite Nanoparticles Prepared Using a Low Temperature, Air-assisted Polyol Process: A new Platform for Diagnostic Imaging

5. 1. Introduction

Magnetite nanoparticles are currently one of the most intensively investigated magnetic materials for their eclectic industrial and bio-medical applications such as multi-tera-bit storage devices [1-3], catalysis [4-5], sensors [6], high performance magnetic resonance imaging (MRI), targeted drug delivery, cell-separation, immunoassay, and hyperthermic treatment of malignant cells [7-10]. A variety of chemical routes have been successfully utilized to prepare well-dispersed Fe_3O_4 nanoparticles (NPs), including coprecipitation [11-12], organic colloid method [13-16], reverse micelle method [17-18], ultrasound irradiation [19], hydrothermal or solvothermal method [20-21] and spray pyrolysis techniques [22]. As already mentioned in **Chapter-I**, coprecipitation of iron salts in alkaline solution in the presence of stabilizers is the most common route for the large-scale preparation of Fe_3O_4-NPs. Although the simplicity of the co-precipitation technique makes it the most frequently adopted solution phase route towards the synthesis of most SPIO or USPIO based nanomedical formulations, a too-fast reaction rate often leads to the formation of magnetite nanoparticles (MNPs) with broad size distribution, irregular crystallite shape, and poor crystallization. The recently developed organic colloid method based on the high temperature organic phase decomposition of organometallic iron precursors in presence of high-boiling nonpolar solvents provides an effective approach to synthesize monodispersed Fe_3O_4 –NPs with controlled size and shape. For example, Sun et al. reported highly uniform magnetite nanoparticles through Fe-acetylacetonate decomposition in phenyl ether [13]. Park *et al.* has accomplished the large-scale synthesis of Fe_3O_4 through Fe-oleate precursor decomposition at 320°C in high-boiling-point octadecene [15]. However, the produced nanocrystals lack aqueous dispersibility due to the capped, hydrophobic surface ligands. This, however, restricts the applicability of the as-prepared MNPs in the biomedical field unless a complicated surface modification is employed. Recently, a modified synthetic approach in highly polar solvent has been proposed by Gao et al. that render particles water-soluble as compared to the previously mentioned thermal decomposition methods, which require further surface modification to pull organic-soluble particles into water resulting in lower yield and poor dispersion stability [23].

The motivation of the present work stems in from the need to develop a facile synthetic strategy for the gram-scale preparation of biologically safe, water-dispersible MNPs with a reactive functional handle using relatively low-grade, non-toxic reagents and green

conditions. In course of extensive literature survey and our continuous efforts to design new targeted nanoparticles for theragnostic applications, we came across a number of interesting observations, which has been considered in the present work while planning the synthesis of our target nanoprobe. It is well documented that amine and carboxyl groups are the most desired targets for any bio-conjugation reaction. In fact, all bio-functionalized Fe_3O_4-NPs developed in course of the present dissertation have used either amine or carboxyl functionalized magnetite nanoparticles as the bio-conjugating precursor. For bio-conjugation purpose, functionalization of nanoparticles with a pendant amine group is more preferable because aminated bases are amenable to conjugation with a diverse array of small molecules through sulfhydryl, carboxyl, anhydride or imine chemistry, allowing easy manipulation of the surface-functionality. In addition, introduction of a cationic amine layer on the top of magnetic nanoparticles (MNPs) may facilitate enhanced nanoparticle uptake inside the target cells through electrostatic interaction between these non-targeted, positively charged particles and negatively charged cell membrane. Furthermore, appropriate tuning of nanoparticle size and surface chemistry can transform these non-targeted nanoparticles into targeted ones, thereby facilitating their preferential accumulation inside the cancer cells via size or charge induced passive targeting.

In this chapter, we attempt to synthesize highly water-dispersible, amine functionalized magnetite nanoparticles with tunable size using a low-temperature, air-assisted polyol process. Optimized for biomedical purposes, 6 nm amine functionalized MNPs have been synthesized and characterized in terms of size, stability, surface-chemistry, magnetization and magnetorelaxometry. The synthetic method consists of reducing the single iron-source $FeCl_3.6H_2O$ with an excess of the polyol ethylene glycol (EG) in the presence of **(i)** sodium acetate as an alkali source and **(ii)** 2'2'-(ethylenedioxy)-bis-(ethylamine) [EDBE] as an electrostatic stabilizer cum amine-functionalizing agent. The excess EG supplements the dual role of solvent and reductant. The "mini-PEG" EDBE was chosen because of its excellent hydrophilicity and bio-compatibility. Despite the success of polyol approach in the generation of metal or metal-oxide nanostructures with controllable size and morphology, disadvantages are that it needs a long time (at least 7-8 h), high temperature (>200°C) and most of the reports embarking on the polyol synthesis of magnetite nanoparticles to date cannot proceed without the introduction of inert Ar or N_2 in the reaction mixture. Recently, a modified polyol approach was undertaken by Liu et al. to synthesize highly water-dispersible, uniform-sized magnetite particles, using citrate as the stabilizer [24]. However, this method too required prolonged, high temperature ageing of the metal precursor in an autoclave for several hours so

that immediately after formation, the produced nanocrystals with average size of 5-10 nm ripened into large clusters of average diameter ~250 nm. In our case, by using simple aerobic condition and EDBE in conjunction with EG, both reaction temperature and time were dramatically reduced to 120°C and 40 minutes respectively, producing ultrasmall, amine functionalized magnetite NPs with tunable size. Even in comparison to the amine functionalized magnetite nanoparticles (NPs) and hollow nanospheres, reported by Wang *et al*. [25], the NPs developed in course of our research have smaller size, which enables them to act as stealth particles and enhances their uptake inside malignant cells through enhanced permeation and retention (EPR) effect. To further corroborate the existence of free amino groups on the NP surface, the Fe_3O_4-EDBE-NPs were bio-conjugated with goat immunoglobulin antigens (IgG-Ag) and used in the magnetic separation of fluorescein isothiocyanate (FITC)-labeled rabbit antigoat IgG antibody (FITC-Ab1) [**Scheme 5.1**]. *In vitro* cell-uptake, MR imaging and biocompatibility studies were performed against both cancer and normal cell lines with an aim to explore the suitability of these ultrasmall, positively charged particles as a platform for diagnostic imaging.

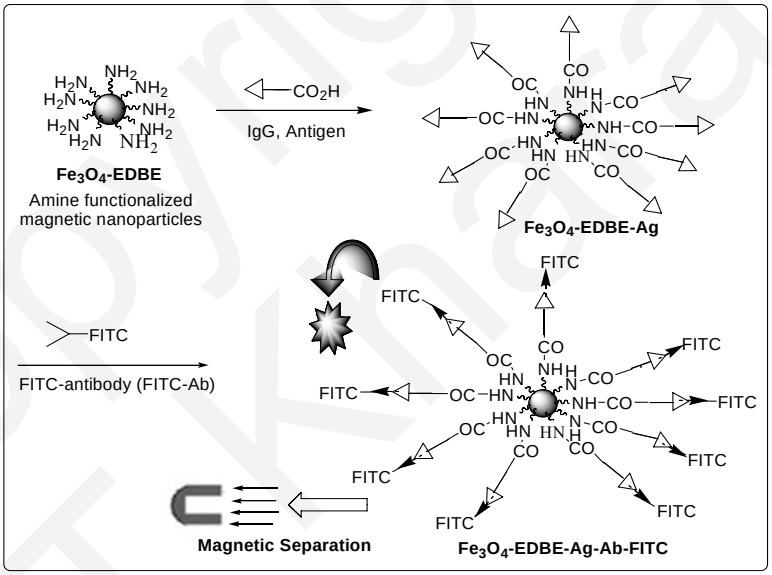

Scheme 5.1: Bioconjugation of Fe_3O_4-EDBE-NPs with goat IgG-Ag and magnetic separation of target antibody

5. 2. Materials and Methods

5.2.1. Materials

As already mentioned in the previous chapters, $FeCl_3.6H_2O$, Ethylene glycol (EG) and Sodium acetate (NaOAc) were obtained from Merck, Germany. 2,2′-(ethylenedioxy)-bis-(ethylamine) (EDBE) was obtained from Aldrich Chemicals, USA. The cells cultivated for *in vitro* experiments viz. human cervix adenocarcinoma, HeLa and MCF-7 breast cancer cell lines were obtained from the National Centre for Cell Sciences (NCCS) Pune, India. Macrophages were isolated from Swiss albino mice by peritoneal lavage in chilled PBS and enriched by adherence to the petriplate surface.

5.2.2. Synthesis methodologies

5.2.2.1. Synthesis of amine functionalized magnetite (Fe_3O_4-EDBE) nanoparticles

In a 500 ml beaker, a mixture of $FeCl_3.6H_2O$ (10 mmol), sodium acetate (10 mmol) and ethylene glycol (30 ml) was stirred vigorously at 50° C to give a transparent solution. To the resultant solution, various concentrations of EDBE, ranging from 10-50 mmol was added and the temperature of the reaction mixture was raised to 120°C by placing the beaker over a hot plate thermostated at the aforesaid temperature. The reaction mixture was continuously stirred with a glass rod. Heating was continued for additional 30-35 minutes until the brown suspension transformed into a black colloid. This black colloidal suspension was cooled to room temperature and the resulting particles were subjected to magnetic decantation, followed by repeated washing with distilled water, ethanol and acetone. Finally these nanoparticles were freeze-dried and preserved for further physicochemical and biological studies.

5.2.2.1. Bio-conjugation of Fe_3O_4-EDBE-NPs with goat IgG-Ag and magnetic separation of target antibody

The method for the goat IgG-Ag bio-conjugation to the magnetite nanoparticles was similar to that of the reported protocols [25]. In brief, IgG-Ag (0.01 mmol) was dissolved in phosphate-buffered saline. The pH of the resulting solution was adjusted to 8 by adding a drop of 0.01

mmol of NaOH solution, followed by activation with 1-ethyl-3-(3-dimethlyaminopropyl) carbodiimide (EDC; 0.01 mmol) and N-hydroxysuccinimide (NHS; 0.02 mmol). After 2 h, an aqueous dispersion of the as-prepared 6 nm amine-functionalized MNPs in PBS was added to the activated solution of IgG-Ag and left to stirring at room temperature under argon atmosphere for additional 3 h. Excess IgG-Ag, EDC and NHS were removed by magnetic field separation and rinsed with PBS solution (three times). The Ag modified magnetic nanoparticles (Fe_3O_4-EDBE-Ag) were redispersed in PBS (5.0 mL) and used in the magnetic separation and concentration of the target fluorescein isothiocyanate (FITC)-labeled rabbit antigoat IgG antibody (FITC-Ab1). In a typical experiment, a solution of Fe_3O_4-EDBE-Ag in PBS (100 µL, 1 mg mL^{-1}) was added to a solution of FITC-Ab1 in water (200 µL, 2 mg mL^{-1}) with stirring and the mixture was incubated at room temperature for 2 h. The mixture was then thoroughly mixed and the fluorescence of the mixed solution was recorded immediately before magnetic separation. The Fe_3O_4-EDBE-Ag–Ab1-FITC composite was separated by magnetic-field separation technology and washed with PBS buffer solution (3 times). The fluorescence of the nanocomposite solution and the supernatant were measured. The selectivity of this magnetic separation method was accomplished by the control experiment with FITC-Ab2, following the same protocol, described in the target experiment.

5.2.3. Characterization

As-prepared MNPs were extensively characterized in terms of size, charge, surface-chemistry, magnetization and magnetorelaxometry according to the procedure as described in the previous chapters. Surface morphology of the nanoparticles was studied with a field emission scanning electron microscope (JEOLJSM5800). Bio-conjugation of Fe_3O_4-EDBE-NPs with goat IgG-Ag and magnetic separation of target antibody was probed via fluorescence measurements using an F-4500 fluorescence spectrophotometer (Hitachi, Japan).

5.2.4. *In-vitro* studies

Nanoparticle uptake by different cell lines were studied by magnetically activated cell sorting (MACS) and *in-vitro* cellular imaging studies. Nanoparticle mediated cytotoxicity was evaluated by the MTT assay, according to the protocol described in the earlier chapters.

5. 3. Results and discussions

The X-ray diffraction (XRD) pattern of the as-prepared MNPs (**Fig. 5. 1**), matched well with that of inverse spinel magnetite (JCPDS card no. 85-1436).

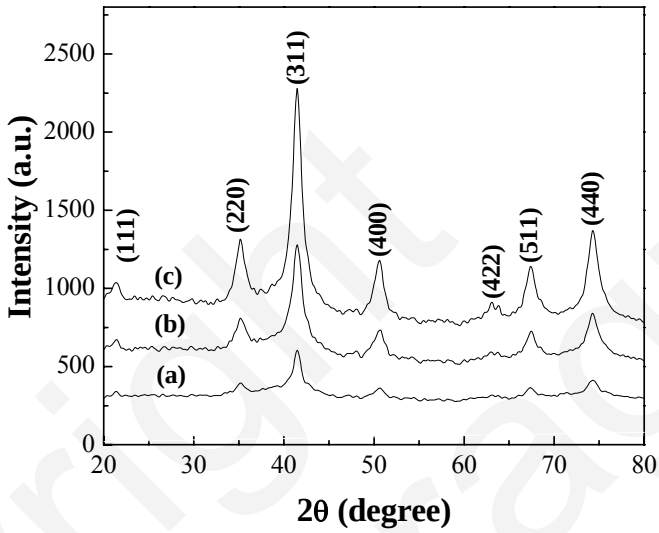

Fig. 5.1: X-ray diffraction pattern of Fe_3O_4-EDBE-NPs synthesized with $FeCl_3$: EDBE ratio **(a)** 1:1 **(b)** 1:3 and **(c)** 1:5

At temperature below 120° C viz. 100, 105 and 110° C, particles showed very little or practically no magnetic response, indicating 120°C as the threshold temperature for the synthesis of magnetite nanoparticles under aerobic conditions. At 120°C, the reaction time over a range of 0.75 to 3 h seems to have a little effect on particle diameters. A thorough optimization of reactant concentration reveals an increased uniformity in particle shape, size and dispersion on changing the $FeCl_3$ to EDBE ratio from 1:1 to 1:5. Typically the 6 nm magnetite particles were synthesized with $FeCl_3$:NaOAc:EDBE:EG ratio of 1:1:5:50. Field emission scanning electron microscopy (FESEM) analysis demonstrated that with increasing EDBE concentration, the surface of the MNPs were composed of finer, more uniform, closely packed and well-aligned particles. The improved homogenity in particle size and dispersion with increasing amine (EDBE) is a good match with the well-known "Authiol" system, in which both size and dispersivity of thiol-stabilized Au nanoparticles improve with increasing thiol concentration [26]. Transmission electron microscopy (TEM) image shows that the average size of MNPs synthesized with an optimal metal precursor to ligand ratio (1:5) was 6 ± 0.75

nm, which is in the superparamagnetic size range (**Fig. 5. 2**). The value is in good agreement with the crystallite size of the NPs (5.7 nm) calculated from XRD the small deviation may creep in considering the fact that the very small particles are hardly discernable in TEM images and thus may be omitted in the measurements. The organization of these ultrasmall particles closely resembled a pomegranate with seeds, somewhat loosely packed into a large conglobulation. High resolution TEM (HRTEM) image further revealed that these ultrasmall seeds were nearly uniform and monodispersed in size with considerable dispersancy. The lattice spacing between two adjacent planes was calculated to be 2.95 A°, corresponding to the distance between (220) plane of bulk spinel magnetite (Fe_3O_4). The selected-area diffraction (SAED) pattern indicates polycrystalline nature of the as-prepared sample. The individual planes identified from the SAED pattern correlates well with that of the XRD pattern.

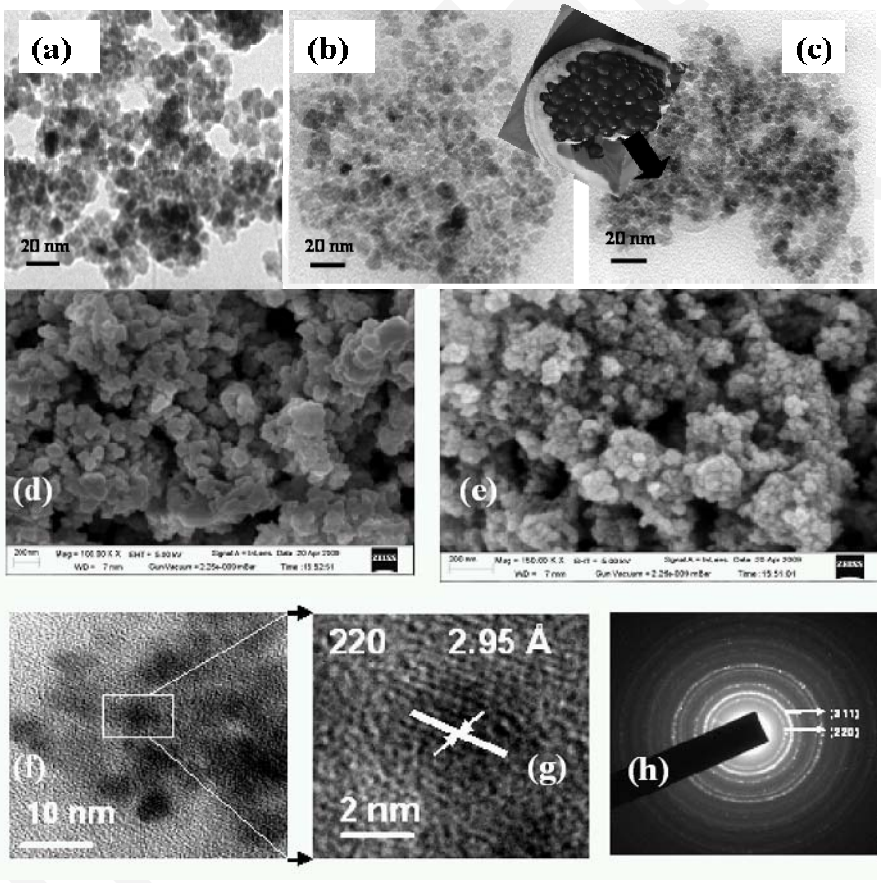

Fig. 5.2: (a-c) Transmission electron micrograph (TEM) of MNPs, synthesized with $FeCl_3$: EDBE ratio 1:1, 1:3 and 1:5 respectively (cross-section of a pomegranate presented as inset) **(d-f)** field emission scanning electron microscopic (FESEM) image of MNPs, synthesized with $FeCl_3$: EDBE ratio 1:3 and 1:5 respectively **(g-h)** HRTEM and single-particle HRTEM and **(k)** SAED pattern of the as-prepared 6 nm particles, synthesized with $FeCl_3$: EDBE ratio 1:5.

Dynamic light scattering (DLS) studies of the as-prepared MNPs further confirmed the presence of stable, non-aggregated particles with a mean hydrodynamic diameter (HD) of 105 nm and a zeta potential of 31.6 mV. As indicated by 4-nitrobenzaldehyde assay [27], an amine density of 40.56 nmol/ mg of MNP was detected. The physicochemical properties of Fe_3O_4-EDBE MNPs, synthesized with different concentrations of metal precursor and ligand have been summarized in **Table 5.1.** Due to the presence of surface-pendant amine groups, aqueous suspensions of the as-prepared MNPs were highly stable under slightly acidic conditions (pH 6.5-6.8), attributed to the obvious electrostatic repulsion between the protonated amine functions ($-NH_3^+$) on the nanoparticle surface as also the hydrogen bonding between water and hetero atom (-O-) of the surface ligand EDBE.

Table 5.1: Physicochemical properties of Fe_3O_4-EDBE-NPs synthesized with varying $FeCl_3$-EDBE ratio.

[$FeCl_3$]: [EDBE]	**Crystallite Size** (nm)	**Particle size** (nm)	**Hydrodynamic diameter (nm)** [at pH 6.5]	**Surface amine density** (nmol/mg)	**Zeta Potential (mV)** [at pH 6.5]
1:1	9.0	11.0	165	14.25	25.5
1:2	7.5	9.3	156	22.84	28.6
1:3	7.1	8.2	129	30.62	29.4
1:5	5.2	6.0	105	40.56	31.6
1:7	5.6	5.7	114	39.77	30.2

To provide direct proof for amine functionalization, the as-prepared Fe_3O_4-EDBE NPs were subjected to fourier transform infrared (FTIR) analysis. The results have been displayed in **figure 5.3.**

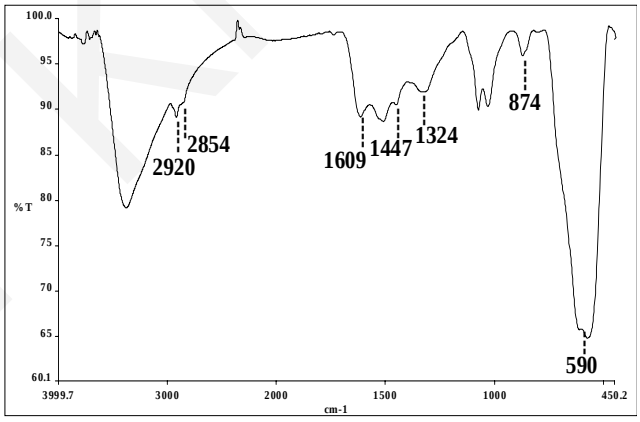

Fig. 5.3: FTIR spectrum of the as-prepared Fe_3O_4-EDBE nanoparticles

The strong IR band at 590 cm^{-1} is the characteristic of Fe-O vibration related to the magnetite core, while the transmissions around 874, 1447 and 1609 cm^{-1} matched well with that from free EDBE, indicating the presence of free amino groups on the nanoparticle surface. The observed red-shift of Fe-O vibration, as compared to bare magnetite (580 cm^{-1}) is due to the chemisorption of EDBE on the nanomagnetite surface. These results clearly reveal that the magnetite nanocrystals have been functionalized with amine groups in the course of the synthetic process.

From XPS measurements, the $Fe2p_{3/2}$ and $Fe2p_{1/2}$ doublets, observed at 711.8 and 725 eV, were identified with the magnetite core of Fe_3O_4-EDBE nanoparticles (**Fig 5.4)**. N, Fe and O peaks were corrected with reference to the C 1s peak at 284.5 eV. A symmetric N 1s peak for Fe_3O_4-EDBE nanoparticles appears at 398.6 eV, indicating the presence of N as a charged species. If the diamine remained coordinated to the Fe (III) centre, a very low intensity peak at 397.3 eV would have appeared, arising out of the iron (III)-amine complex. The binding energy region corresponding to the free amine group or bonded amine falls in the range of 398-400 eV. This peak suggests the involvement of electrostatic interactions, particularly with a nanoparticle surface, and is in good agreement with earlier observations [28].

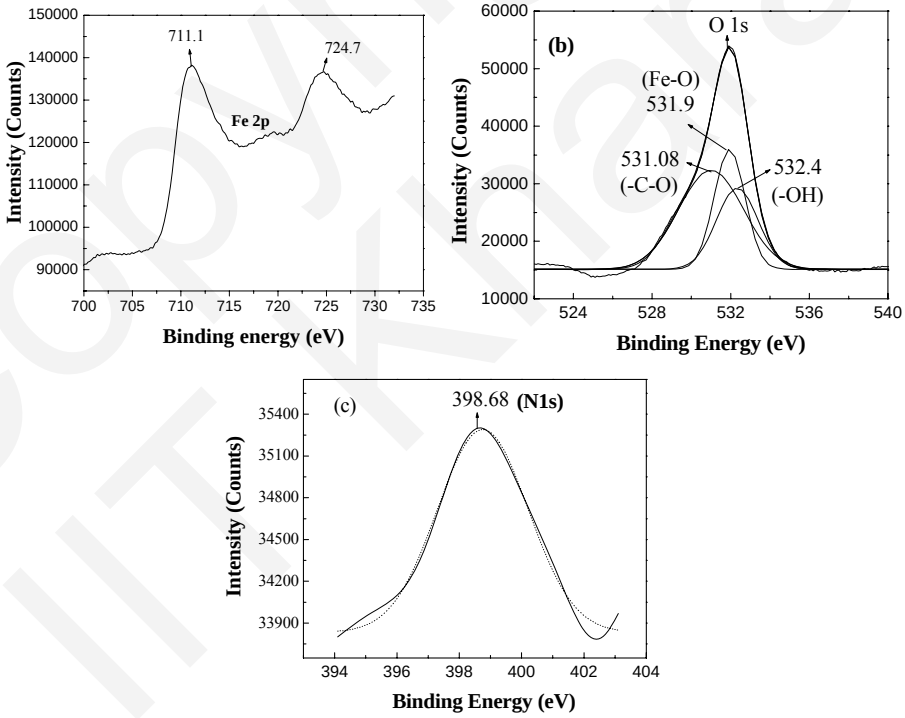

Fig. 5.4: High resolution **(a)** Fe 2p **(b)** O 1s and **(c)** N1s X-ray photoelectron spectrum of the as-prepared Fe_3O_4-EDBE nanoparticles

Illustrated in figure **5.5** is the magnetization curve of 6 nm Fe_3O_4-EDBE particles, measured at room temperature. Lack of coercivity and remenance in the magnetization loop corroborated the superparamagnetic nature of the as-synthesized sample. The sample could not be magnetically saturated at the magnetic field limit of our VSM (1T). The magnetization value obtained at 7000 Oe was 37.8 emu g^{-1}, which is pretty consistent with those of the [$N(CH_3)_4OH$] protected Fe_3O_4 nanoparticles (40 emu g^{-1}) reported previously by Cheng et al.[29], the MIONs used as MRI contrast agents by Weissleder *et al* [30] and γ–Fe_2O_3 based MION ferrofluid synthesized by Lu et al [31]. However the saturation magnetization value is much lower in comparison to that of bulk magnetite, which might be explained in the light of small-particle surface effect and internal cationic disorder.

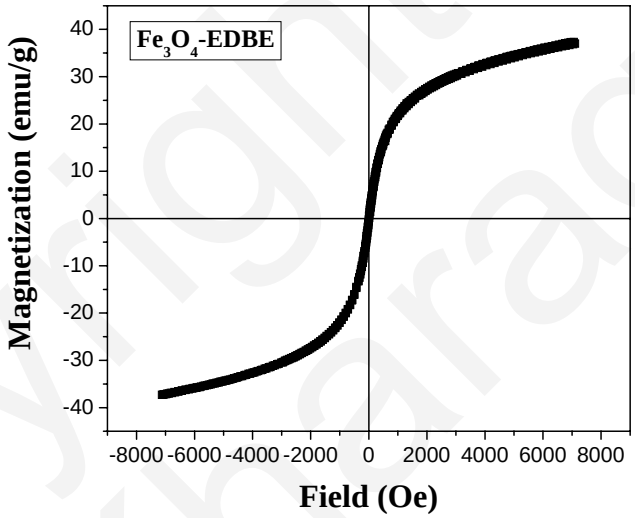

Fig. 5.5: Magnetization (M-H) curve of the as-prepared Fe_3O_4-EDBE-NPs

Although polyol synthesis provides a simple and versatile approach to the generation of metal and metal-oxide nanostructures with controlled shape and size, many fundamental aspects of the synthesis process, in particular, the mechanism of reduction of metal ions by ethylene glycol (EG) remains poorly understood. Fiévet et al. studied the mechanism of polyol reduction, focusing on cobalt and nickel hydroxide precursors [32]. On the basis of the detection of diacetyl after reaction at 197°C, acetaldehyde was proposed to be the possible reductant.

$$HOCH_2CH_2OH \rightarrow CH_3CHO + H_2O \qquad \textbf{(Eq. 5.1)}$$

$$2M^+ + 2CH_3CHO \rightarrow CH_3COCOCH_3^+ + 2M + 2H^+ \qquad \textbf{(Eq. 5.2)}$$

Although not discussed in their report, acetaldehyde formation was most likely promoted by the hydroxide anions from the metal precursors and thus cannot be a general explanation to account for the reductive power of EG under most reduction conditions. In addition, the proposed mechanism fails to rationalize many observations, which include **(i)** the inability to detect diacetyl at 150°C, even though reduction of many metal precursors occurs; **(ii)** high sensitivity of the reaction rate to reaction atmosphere. All these suggest the existence of an alternative reduction mechanism. Using a simple spectrophotometric method, Skrabalak *et al.* have recently shown that aerial oxidation of EG at higher temperatures lead to the generation of glycolaldehyde (GA), a reductant for many metal ions [33].

$$HOCH_2CH_2OH + O_2 \rightarrow 2\ HOCH_2CHO + 2H_2O \qquad \textbf{(5. 3)}$$

This finding provides a critical insight into how the polyol synthesis can be used to generate metal nanostructures with controllable size and morphology. We considered this pathway and tried to prove the feasibility of GA mediated reduction in our system. To first discern, whether our MNPs were built up of magnetite ($Fe_3O_4 \equiv 2Fe^{3+}Fe^{2+}4O^{2-}$) or maghemite ($Fe_2O_3 \equiv 2Fe^{3+}3O^{2-}$), the existence of Fe^{2+} ions in the as-prepared MNP formulation was determined by redox titration with potassium dichromate. Significant Fe^{2+} concentration was determined in the titrand, suggesting magnetite phase as the crystalline phase. Moreover, the nanoparticle dispersion presented a black color, as is expected for magnetite solutions instead of reddish brown color corresponding to maghemite dispersions. These observations, along with physicochemical characterization data suggested the involvement of some reducing agent throughout the course of the synthesis process, responsible for the partial reduction of Fe (III) to Fe (II).

Initially, we faced a lot of problem in identifying the actual reductant because in our case the situation turned a bit complicated due to the involvement of both EG and EDBE. Amines, being well known for their reducing behavior had every possibility to reduce the metal ions. So our first and foremost duty consisted in identifying the primary reductant for metal precursor, responsible for the generation of the mixed oxide, $FeO{\cdot}Fe_2O_3$. It was interesting to note that no nanoparticle formation occurred in the absence of either EG or EDBE, suggesting that both the reagents had some specific role in the synthesis of MNPs under the specified conditions. In absence of EDBE, the reduction of Fe (III) to Fe (II) occurred, as indicated by the presence of Fe (II) in the reaction mixture, determined by 1, 10 phenanthroline colorimetric assays [34]. On the other hand, carrying out the reaction in the absence of EG led to a reddish brown solution without any Fe^{2+} ion. This further suggests EG to be the source of actual reductant and EDBE as a nucleation and growth controlling reagent. Additionally, it

was believed to render some synergistic effect on the polyol reduction process, which allows the reaction to proceed under milder conditions, as compared to the existing literatures. Most of the reported syntheses of magnetite nanoparticles are typically performed under inert atmosphere and closed vessels. Prior to the addition of metal precursors, degasification of the reaction medium is mandetory, which suggests that the reaction is highly atmosphere sensitive. However, to the contrary of our expectations, the present reaction proceeded smoothly in gram-scale over a hot plate under simple aerobic condition. In line with the observations of Skrabalak et al., we assumed partial transformation of ethylene glycol to glycolaldehyde in presence of air and to establish our hypothesis, we carried out a blank experiment in which ethylene glycol was heated to 120 °C in open air for 25 minutes. Because of the limitation of NMR, gas chromatography (GC) and mass spectroscopic methods in detecting and quantifying microgram amounts of GA, mixed with a large amount of EG, GA production was ensured using a standard colorimetric method, adopted by Blanks et al. for the microanalysis of GA [35]. From these observations, it was inferred that during initial stages of the reaction, atmospheric oxygen as well as oxygen dissolved into water was continuously consumed by EG for its transformation to GA. This creates an oxygen-deficient atmosphere, which prevents any further oxidation of Fe^{2+} to Fe^{3+} in the later stages of the reaction. Rapid elimination of water from the reaction mixture also enhances the rate of GA production. To revalidate this hypothesis, the reaction was repeated in an argon-charged vessel, when only traces of GA could be detected after prolonged heating for 10-12 h (**Fig. 5.6**). All these observations indicate that the presence of air is crucial for GA production.

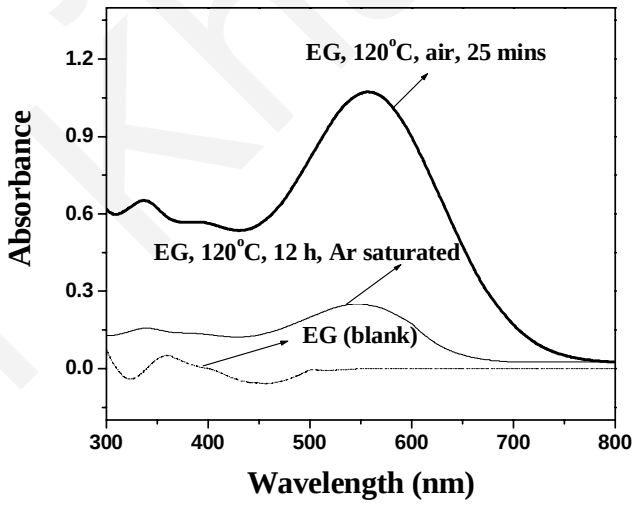

Fig. 5.6: Spectrophotometric determination of glycolaldehyde (GA) produced from ethylene glycol in air at room temperature, ethylene glycol heated to 120 °C in presence of air and ethylene glycol heated at 120 °C in argon charged closed container for 12 h.

Having the primary reductant identified, we tried to probe into the mechanism of NP formation. A plausible mechanistic pathway has been schematized in **Fig. 5.7.**

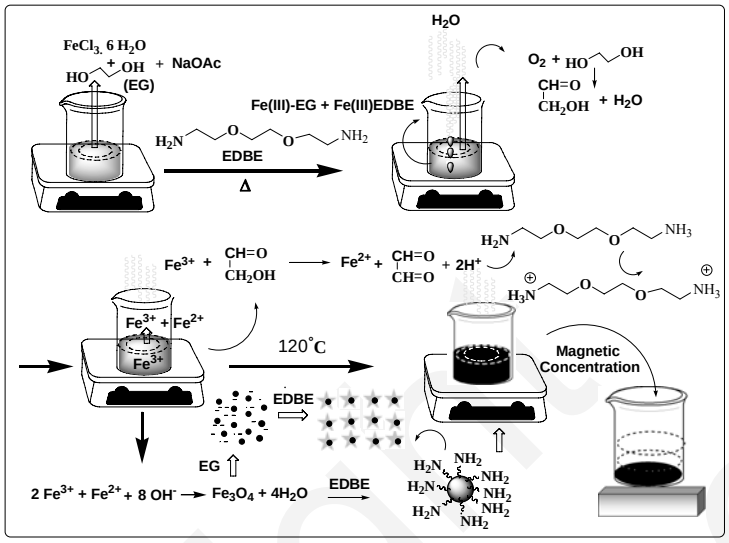

Fig. 5.7: Mechanistic interpretation of the low temperature polyol reduction and nanoparticle formation

Apart from its reducing action through GA production, during the initial stages of the reaction, EG complexes with Fe^{3+} and slows down the formation of hydroxide or oxide counterparts. EDBE has a stronger chelation affinity than EG. In the present work both EG and EDBE chelate iron-ions and form stable complex at low temperature, which is indicated by the color change from orange to deep reddish-brown and a temporary gelation of the reaction mixture, immediately with the addition of EDBE. Significant changes in the FTIR spectrum was observed in the 1400-1700 cm^{-1}, possibly due to the formation of metal-EDBE complex, in addition to the metal-EG complex (**Fig.5. 8**). Although we could not identify the exact structure of the complex formed, it can be speculated that this intermediate compound plays a crucial role in obtaining highly pure and well-crystallized nanocrystals. When the resulting mixture is heated over a hot plate, thermo- stated at 120˚C, the complex becomes labile and Fe^{3+} is gradually released into the solution. Meanwhile GA produced through the aerial oxidation of EG partially transforms $Fe^{3+} \rightarrow Fe^{2+}$ and itself oxidized to glyoxal, which being a highly volatile liquid is rapidly eliminated from the reaction mixture. The liberated Fe^{3+} and Fe^{2+} ions combine with OH^- ions slowly released by sodium acetate in appropriate stoichiometry and co-precipitate at once

$$HOCH_2CHO + Fe^{3+} \rightarrow Fe^{2+} + (CHO)_2 + 2H^+ \qquad \textbf{(5.4)}$$

$$2Fe^{3+} + Fe^{2+} + 8\ OH^- \rightarrow Fe_3O_4 + 4H_2O \quad \textbf{(5.5)}$$

At this stage, the high viscosity of EG as well as EDBE inhibits the mass transformation in the reaction system and results in a slow, controlled seed growth. The alkaline matrix provided by EDBE readily scavenges the H^+ ion liberated in course of metal precursor reduction, which not only increase the rate of the forward reaction but allows the reduction process to take place under such mild conditions. The diamine salt, formed through the protonation of EDBE interacts with the surface hydroxyl groups and caps the MNPs with a protective amine layer, which, in addition to inducing electrostatic repulsion between the nanocrystals prevents any further oxidation on the surface. FTIR spectrum of the mother liquor collected after magnetic concentration of the MNPs from reaction mixture corresponded to unreacted EG with traces of the diamine salt, as indicated by weakly intense IR absorption bands at 2200 cm^{-1}. This further suggests that the surface of as-prepared MNPs has been functionalized with EDBE.

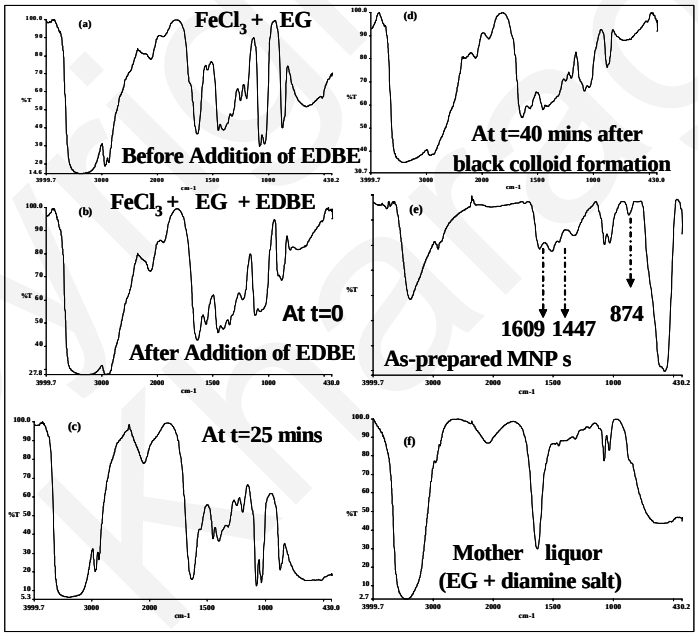

Fig. 5.8: FTIR spectrum of the reaction mixture **(a)** before addition of EDBE **(b)** after addition of EDBE **(c)** after 25 minutes **(d)** after 40 minutes of heating the reaction mixture at 120˚C **(e)** the as-prepared magnetite nanoparticles and **(f)** mother liquor.

In order to demonstrate their magnetic bioseparation and concentration implications in immunoassays, the as-synthesized 6 nm magnetite particles were bio-conjugated with goat immunoglobulin antigens (IgG-Ag) to form the antigen labeled MNPs (Fe_3O_4-EDBE-Ag) and then used in the magnetic separation of fluorescein isothiocyanate (FITC)-labeled rabbit

antigoat IgG antibody (FITC-Ab1), according to the procedure depicted in **Scheme 5.1.** In this bio-conjugation experiment, the antigens were attached to the surface of MNPs through covalent interaction between activated carboxyl groups of the antigens and the amino groups on the nanoparticle surface. These antigen-modified MNPs were subsequently used in the magnetic separation and concentration of FITC-Ab1. Based on the specific antigen-antibody interaction, FITC-Ab1 was concentrated and separated from the solution. Figure **5.9(a)** shows the fluorescence spectra of free antibody, Fe_3O_4-EDBE-Ag–Ab1-FITC nanocomposite solution, the supernatant after the magnetic separation and Fe_3O_4-EDBE (unmodified) respectively. As compared to free antibody, the fluorescence of the supernatant is very weak while that of the nanocomposite solution is very strong, which means that FITC-Ab was bound to the antigen and separated. Figure **5.9 (b)** shows the selectivity of the magnetic separation method, testified by the control experiment following a similar strategy. In brief, the antibody used for magnetic bioseparation in the control experiment was FITC-labeled rabbit antihuman IgG antibody FITC-Ab2 instead of the anti-goat FITC-Ab1. The fluorescence intensity of the supernatant was virtually unchanged before and after the magnetic separation. Meanwhile, the magnetic nanoparticle solution hardly exhibited any fluorescence, which revealed that FITC-Ag2 was not bound to the antibody modified magnetic nanoparticles. The results demonstrated the good selectivity of the present magnetic bio-separation technology based on the amine functionalized MNPs, as also the existence of amino groups on the outer surface of the magnetic nanocrystals.

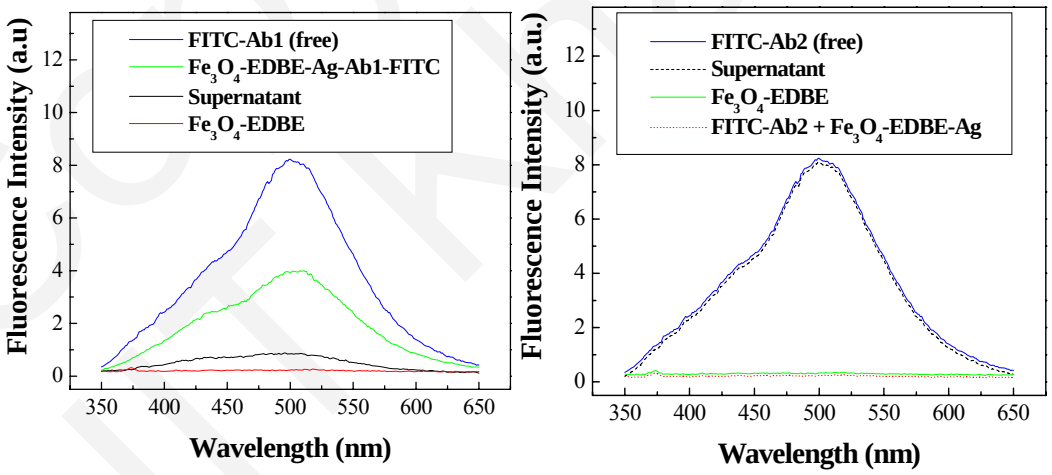

Fig. 5.9: (a) Fluorescence spectra of **(i)** FITC-Ab1 (free) **(ii)** Fe_3O_4-EDBE-Ag-Ab1-FITC **(iii)** Supernatant and **(iv)** Fe_3O_4-EDBE **(b)** Fluorescence spectra of **(i)** FITC-Ab2 **(ii)** Supernatant **(iii)** Fe_3O_4-EDBE and **(iv)** FITC-Ab2 + Fe_3O_4-EDBE-Ag

To investigate the MR signal enhancement effects, the aqueous as-prepared nanoparticles at different Fe concentrations were suspended in agarose and measured using a 0.3 T clinical MRI scanner. As shown in **Fig. 5.10**, the T_2 weighted images changed drastically in signal intensity with an increasing concentration of nanoparticles, indicating that the as synthesized nanoparticles were potential T_2 contrast agents. It was further observed that the relaxation rate $1/T_2$ varied linearly with the iron concentration, according to the following equation:

$$1/T_2 = 1/T^0_2 + r_2\,[Fe] \qquad \textbf{(1)}$$

where $1/T_2$ is the observed transverse relaxation rate in the presence of magnetite nanoparticles, $1/T^0_2$ is the relaxation rate of pure water, [Fe] is the concentration of magnetite nanoparticles and r_2 denotes transverse relaxivities. The transverse relaxivity, r_2, (corresponding to the slopes of the lines) was found to be 113.6308 Fe $mM^{-1}s^{-1}$ respectively.

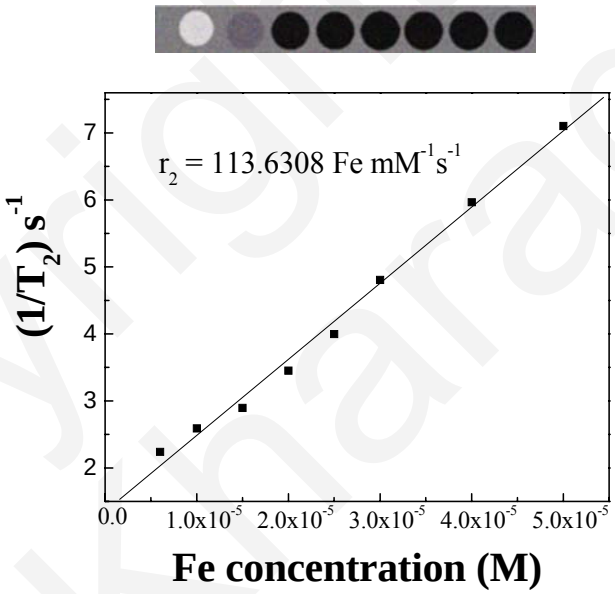

Fig. 5.10: (a) T_2 weighed MR phantom images and **(b)** T_2 relaxation rates ($1/T_2$) plotted against the Fe concentrations of as-prepared aqueous dispersions of amine functionalized MNPs suspended in agarose.

Since the pioneering work of Ogushi in 1978 [36], which established that nanoparticles with magnetic properties have the ability to shorten the T_2 relaxation times of water, superparamagnetic iron-oxide based nanoparticles have attracted decades of studies as MRI contrast agents. Large particles, e.g. conventional polycrystalline iron oxide aggregates, are rapidly phagocytosed by cells of the reticuloendothelial system (RES) and have been found unsuitable for target-specific biomedical applications, for which our ultrasmall, amine

functionalized MNPs might offer a solution. Moreover, *in-vivo* compatibility of large particles is limited by rapid immunologic recognition, which may elicit an immune response. Very small particles, in particular, those with size smaller than the fenestrations can enter the interstitium and entrapped into the tumor site. Until now, all the clinically approved iron-oxide nanoformulations are either wrapped with dextran, starch, albumin or other polymeric coatings. Although polymeric coatings prevent nanoparticle aggregation and improve surface bio-compatibility, their large overall size may significantly limit tissue distribution, intracellular penetration, intravenous delivery, metabolic clearance and also magnetic targeting ability *in vivo*. The ultrafine, amine functionalized magnetite nanoparticles developed in course of our research effort can be very well dispersed into aqueous colloid for MRI contrast agent, which opens a new alternative to the dilemma.

Cellular uptake of the as-synthesized magnetite nanoparticles in human cervical HeLa and MCF 7 breast cancer cell lines was preliminarily assessed using magnetically activated cell sorting. Time dependant study in the span of 0.5-24 h revealed certain interesting observations. While significant nanoparticle internalization was observed in both HeLa and MCF 7 cell lines as early as 4 h of nanoparticle incubation in the culture medium, uptake was nominal is case of normal peritoneal macrophages isolated from Swiss albino mice, even after 24 h of incubation (**Fig. 5. 11)**.

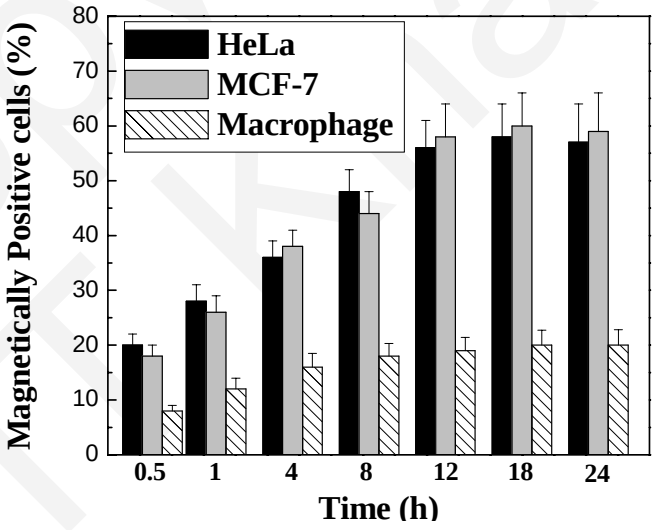

Fig. 5.11: Time dependant cell-uptake behavior of Fe_3O_4-EDBE-NPs against HeLa, MCF 7 and Macrophage cell lines, studied using magnetic cell sorting analysis (MACS).

It should however be noted that uptake of Fe_3O_4-EDBE-NPs in HeLa and MCF-7 cell lines did not show any remarkable improvement in the duration of 12-24 h, which suggests that internalization of MNPs by these cell lines reached to a saturation stage by 12 h and since macrophage uptake is quite low even after 24 h of incubation, these nanoparticles are expected to selectively target the cancer cells and avoid the undesired clearance by RES, when considered for *in-vivo* applications.

To revalidate the above findings, the MR images of the cells, cultured with 0.05 mg Fe /ml of the as-prepared nanoparticles for 1, 4 and 12 h were subsequently recorded with a clinical 0.3 T MRI scanner by suspending the MNP internalized cells in agarose. Within 4 h, the T_2 weighed MR phantom images showed a significant signal darkening for both HeLa and MCF 7 cell lines, as compared to normal macrophage cells (**Fig. 5. 12**)**,** which, did not show any remarkable change in signal intensity even after 12 h of NP incubation. The results, however, are in good agreement with the MACS data.

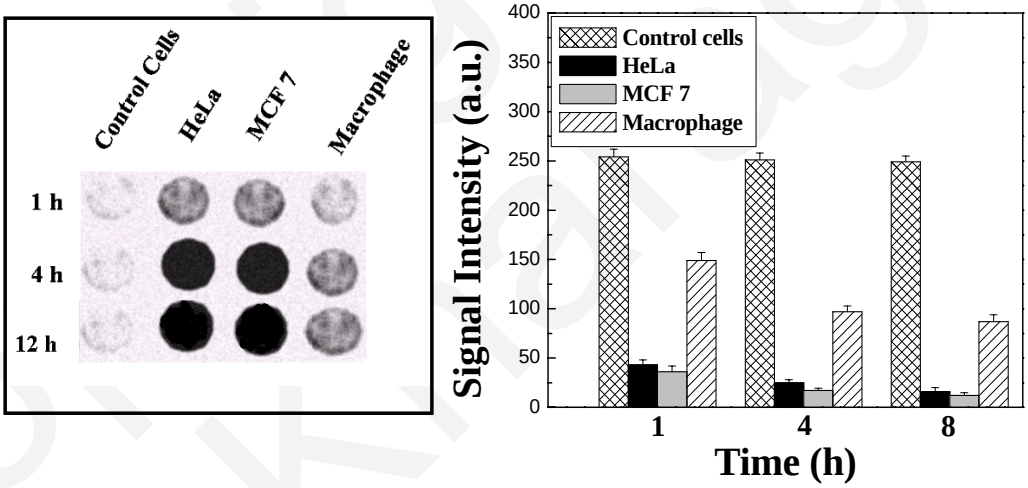

Fig. 5.12: Time dependant cell-uptake behavior of Fe_3O_4-EDBE-NPs against HeLa, MCF 7 and Macrophage cell lines, studied using *in vitro* cellular MR imaging

The strong interaction between the magnetite nanoparticles and cancer cell lines is believed to arise from ultrasmall size and unique surface chemistry of the nanoparticles coupled with the unusual metabolic activity of the cancer cells. Introduction of a cationic layer of EDBE on the top of iron-oxide nanoparticles not only improves their solubility in physiological buffers but also enhances their loading capacity into the cells presumably via the negatively charge bio-molecules on cell membrane. In addition, self-assembling of EDBE on the surface of iron-oxide affording a hydrophilic "mini-PEG" like backbone is believed to lower the uptake of

MNPs by the RES. The hypothesis is well-supported by hydrodynamic size and zeta potential analysis of Fe_3O_4-EDBE-NPs in the presence of culture medium, which showed that in the time span of 0-24 h, exposure of nanoparticles to the culture medium with or without serum had no significant influence on hydrodynamic size and charge of the nanoparticles after magnetic sorting. These results accord well [37] with a recent report on cationic lipid coated magnetic nanoparticles and implies that internalization of nanoparticles inside the target cells is likely to be facilitated by their ultrasmall size or positively charged surface and not via plasma protein adsorption, as in the case of aminosilane coated magnetite nanoparticles reported by Chen et al.[38] The findings are well-consistent with our earlier reports, which established that EDBE modification of MNPs significantly improves the hydrophilicity and bio-compatibilty of the magnetic nanosystem and when conjugated with targeting ligands, also increases their affinity towards the corresponding receptor sites, while minimizing non-specific uptake by macrophages of the mononuclear phagocytic system [39, 40].

The cytotoxicity of the as-prepared nanoparticles in HeLa, MCF-7 and macrophage cells, as evaluated by MTT assay, indicated that the viability of the cells is not affected by the presence of MNPs upto 500 μg/ml, suggesting that our MNPs are highly biocompatible and safe for further *in vivo* evaluations (**Fig. 5.13**).

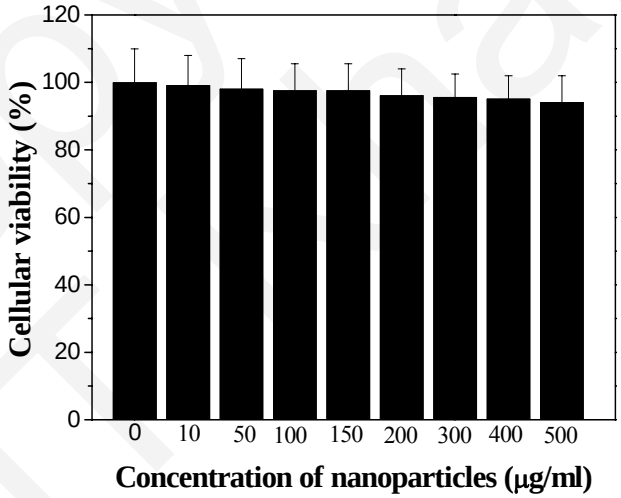

Fig. 5.13: Effect of the Fe_3O_4-EDBE nanoparticles on the viability of HeLa cells. Cells were incubated with as-prepared amine functionalized MNPs for 4h at 37°C, followed by viability assay by MTT method. No significant reduction in cellular viability was observed, the survival rate being higher than 90%, even at the highest nanoparticle concentration.

Since impetus of the present study stemmed in from the need to standardize a facile synthetic strategy towards the gram-scale preparation of biologically safe, water-dispersible MNPs for theragnostic applications, the major emphasis has been given on the process development of existing polyol chemistry and mechanistic investigations. Although preliminary studies have been completed to establish the potential applicability of the synthesized nanoparticles as a platform for cancer-specific targeting and imaging, further *in-vitro* and *in-vivo* evaluations are necessary for a thorough understanding of the intracellular pathway and mechanism of nanoparticle internalization inside target cells as also to ensure whether this newly synthesized probe can serve as a "*maximally stealth and maximally targeted*" carrier *in vivo*.

5.4. Conclusion

In a nut shell, ultrasmall amine functionalized magnetite nanoparticles with excellent aqueous dispersibility and biocompatibility have been synthesized in gram-scale, using a simplified polyol approach. The synthetic method consisted of reducing the single iron precursor $FeCl_3.6H_2O$ with the polyol ethylene glycol (EG) at 120˚C for 40±5 minutes in presence of an alkaline source, sodium acetate and a hydrophilic, nonpolymeric, electrostatic stabilizer 2,2′-(ethylenedioxy)-bis-(ethylamine). In addition to passivating the surface of as-prepared MNPs with a protective amine layer, EDBE affords an alkaline matrix, which, in course of neutralizing the acidic protons liberated in course of the metal precursor reduction, leads to a many-fold increase in reaction rate with subsequent lowering of reduction temperature. To the best of our knowledge, no previous reports have embarked on such a fast, low temperature, polyol synthesis of magnetite nanostructures, using simple aerobic conditions. HRTEM observations revealed the formation of ultrafine, nearly spherical particles with an average diameter of ~ 6 nm. With reasonably high magnetization and amine groups on their outer surface, we established the bio-conjugation of these ultrasmall nanoparticles with goat IgG-Ag and magnetic separation of target FITC-labeled rabbit antigoat IgG antibody. MRI studies indicated that these nanoparticles had the desired relaxivity for MR contrast enhancement *in vivo*. *In vitro* biocompatibility, cell-uptake and MR imaging studies established that these nanoparticles were safe in clinical dosages and owing to their ultrasmall size and positive charge showed high intracellular uptake against cancer cell lines. All these positive attributes make these functional MNPs, a promising platform for diagnostic imaging.

References

1. Raj, K.; Moskowitz, B.; Casciari, R. Advances in ferrofluid technology *J. Magn. Magn. Mater*. **1995**, *149*, 174-180.

2. Sun, S.; Weller, D. Self-Assembling magnetic nanomaterials. J. *Magn. Soc. Jpn*. **2001**, *25*, 1434-1440.

3. Weller, D.; Moser, A. Thermal effect limits in ultrahigh-density magnetic recording *IEEE Trans.Magn.* **1999***, 35,* 4423-4437.

4. Wu, P. G.; Zhu, J. H.; Xu, Z. H. Template-Assisted Synthesis of Mesoporous Magnetic Nanocomposite Particles. *Ad*v. *Funct. Mater.* **2004**, *14*, 345-351.

5. Weiss, W.; Ranke, W. Surface chemistry and catalysis on well-defined epitaxial iron-oxide layers *Prog. Surf. Sci.* **2002**, *70*, 1-151

6. Mohri, K.; Uchiyama, T.; Panina, L. V. Recent advances of micro magnetic sensors and sensing application *Sens. Actuators A* **1997**, *59*, 1-8.

7. Lacava, L. M.; Lacava, Z. G.; Silva, M. F.; Silva, O. D.; Chaves, S. B.; Azevedo, R. B.; Peregrine, F.; Gansau, C.; Buske, N.; Sabolovic, D.; Morais, P. C. Magnetic Resonance of a Dextran-Coated Magnetic Fluid Inravenously Administered in Mice *Biophys. J.* **2001**, *80*, 2483-2486.

8. Weissleder, R.; Bogdanov, A.; Neuwelt, E. A.; Papisov, M. Long-circulating iron oxides for MR imaging. *Adv. Drug Delivery Rev* **1995,** *16,* 321–334.

9. Zhang, Y., Kohler, N. and Zhang, M. Surface modification of superparamagnetic magnetite nanoparticles and their intracellular uptake *Biomaterials.* **2002,** *23* 1553–1561.

10. Gupta, A. K.; Gupta, M. Synthesis and surface engineering of iron oxide nanoparticles for biomedical applications. *Biomaterials* **2005**, *26*, 3995-4021.

11. Massart, R. Preparation of aqueous magnetic liquids in alkaline and acidic media. *IEEE Trans. Magn*. **1981**, *17*, 1247-1248.

12. Kang, Y. S.; Risbud, S.; Rabolt, J. F.; Stroeve, P. Synthesis and Characterization of Nanometer-Size Fe_3O_4 and γ-Fe_2O_3 Particles. *Chem. Mater.***1996**, *8*, 2209-2211.

13. Sun, S.; Zeng, H. Size-Controlled Synthesis of Magnetite Nanoparticles. *J. Am. Chem. Soc.***2002**, *124*, 8204.

14. Park, J.; An, K.; Hwang, Y.; Park, J. G.; Noh, H. J.; Kim, J. Y.; Park, J. H.; Hwang, N. M.; Hyeon, T. Ultra-large-scale syntheses of monodisperse nanocrystals. *Nat. Mater.***2004**, *3*, 891.

15. Park, J.; Lee, E.; Hwang, N. M.; Kang, M.; Kim, S. C.; Hwang, Y.; Park, J. G.; Noh, H. J.; Kim, J. Y.; Park, J. H.; Hyeon, T. One-nanometer-scale size-controlled synthesis of monodisperse magnetic iron oxide nanoparticles. *Angew. Chem. Int. Ed.* **2005**, *44*, 2872.

16. Hyeon, T.; Lee, S. S.; Park, J.; Chung, Y.; Na, H. B. Synthesis of highly crystalline and monodisperse maghemite nanocrystallites without a size-selection process. *J. Am. Chem. Soc.***2001**, *123*, 12798.

17. Lopez Perez, J. A.; Lopez Quintela, M. A.; Mira, J.; Rivas, J.; Charles, S. W. Advances in the Preparation of Magnetic Nanoparticles by the Microemulsion Method. *J. Phys. Chem. B* **1997**, *101*, 8045

18. Lee, Y.; Lee, J.; Bae, C. J.; Park, J. G.; Noh, H. J.; Park, J. H.; Hyeon, T. Large-Scale Synthesis of Uniform and Crystalline Magnetite Nanoparticles Using Reverse Micelles as Nanoreactors under Reflux Conditions. *Adv. Funct. Mater* **2005**, *15*, 503

19. Suh, W. H.; Suslick, K. S. Magnetic and Porous Nanospheres from Ultrasonic Spray Pyrolysis *J. Am. Chem. Soc.* **2005**, *127*, 12007.

20. Si, S.; Li, C.; Wang, X.; Yu, D.; Peng, Q.; Li, Y. Magnetic Monodisperse Fe_3O_4 Nanoparticles. *Cryst.Growth Des.***2005**, *5*, 391.

21. Daou, T. J.; Pourroy, G.; Begin-Colin, S.; Greneche, J. M.; Ulhaq-Bouillet, C.; Legare, P.; Bernhardt, P.; Leuvrey, C.; Rogez, G. Hydrothermal Synthesis of Monodisperse Magnetite Nanoparticles. *Chem. Mater.* **2006**, *18*, 4399-4404.

22. Li, D.; Teoh, W. Y.; Selomulya, C.; Woodward, R. C. Amal, R.; Rosche, B. Flame-Sprayed Superparamagnetic Bare and Silica-Coated Maghemite Nanoparticles: Synthesis, Characterization, and Protein Adsorption-Desorption. *Chem. Mater.***2006**, *18*, 6403-6413.

23. Li, Z.; Chen, H.; Bao, H.; Gao, M. One-Pot Reaction to Synthesize Water-Soluble Magnetite Nanocrystals, *Chem. Mater.* **2004**, *16*, 1391-1393.

24. Liu, J.; Sun, Z.; Deng, Y.; Zou, Y.; Li, C.; Guo, X.; Xiong, L.; Gao, Y.; Li, F.; Zhao, D. Highly water-dispersible biocompatible magnetite particles with low cytotoxicity stabilized by citrate groups. *Angew. Chem. Int. Ed.* **2009**, 48, 5875-5879.

25. Wang, L; Bao, J; Wang, L; Zhang, F; Li, Y. One-Pot Synthesis and Bioapplication of Amine-Functionalized Magnetite Nanoparticles and Hollow Nanospheres. *Chem. Eur. J.* **2006**, *12*, 6341-6347.

26. (a) Hostetler, M. J.; Wingate, J. E.; Zhong, C. J.; Harris, J. E.; Vachet, R. W.; Clark, M. R.; Londono, D. J.; Green, S. J.; Stokes, J. J.; Wignall, G. D.; Glish, G. L.; Porter, M. D.; Evans, N. D.; Murray, R. W. Alkanethiolate Gold Cluster Molecules with Core Diameters from 1.5 to 5.2 nm: Core and Monolayer Properties as a Function of Core Size. *Langmuir* **1998**, *14*, 17-30. (b) Chen, S.; Murray, R. W. Arenethiolate Monolayer-Protected Gold Clusters. *Langmuir* **1999**, *15*, 682-689. (c) Motte, L.; Pileni, M. P. Influence of Length of Alkyl Chains Used To Passivate Silver Sulfide Nanoparticles on Two- and Three-Dimensional Self-Organization. *J. Phys. Chem. B* **1998**, *102*, 4104.

27. Bruce, I. J.; Sen, T. Surface Modification of Magnetic Nanoparticles with Alkoxysilanes and Their Application in Magnetic Bioseparations. *Langmuir* **2005,** *21*, 7029

28. Aslam, M.; Schultz, E. A.; Tao, S.; Meade, T.; Dravid, V. P. Synthesis of Amine-stabilized Aqueous Colloidal Iron Oxide Nanoparticles. *Cryst Growth Des.* **2007**, *7*, 471–475.

29. Cheng, F. Y.; Su, C. H.; Yang, Y. S.; Yeh, C. S.; Tsai, C. Y.; Wu, C. L.; Wu, M. T.; Shieh, D. B. Characterization of aqueous dispersions of Fe_3O_4 nanoparticles and their biomedical applications. *Biomaterials* **2005**, *26,* 729–38.

30. Weissleder, R.; Elizondo. G.; Wittenberg, J.; Rabito, C. A.; Bengele, H. H.; Josephson, L. Ultrasmall superparamagnetic iron oxide: characterization of a new class of contrast agents for MR imaging. *Radiology* **1990**, *175***,** 489–93.

31. Lu, J.; Yang, S. H.; Ng, K. M.; Su, C.H.; Yeh, C. S.; Wu, Y.N.; Shieh, D.B. Solid-state synthesis of monocrystalline iron oxide nanoparticle based ferrofluid suitable for magnetic resonance imaging contrast application. *Nanotechnology* **2006**, *17*, 5812–5820.

32. Fievet, F.; Lagier, J. P.; Figlarz, M. Preparing monodisperse metal powers in micrometer and submicrometer sizes by the polyol process. *MRS Bull.* **1989**, *14*, 29.

33. Skrabalak, S. E.; Wiley, B. J.; Kim, M.; Formo, E. V.; Xia, Y. On the Polyol Synthesis of Silver Nanostructures: Glycolaldehyde as a Reducing Agent *Nano Lett.,* **2008**, *8,* 2077-2081.

34. Herrera, L.; Ruiz, P.; Aguillon, J. C.; Fehrmann, A. Journal of Chemical Technology & Biotechnology **1989,** 44**,** 171-181.

35. Banks, T.; Vaughn, C.; Marshall, L. M. Spectrophotometric Determination of Glyoxal Bis (2, 4-dinitrophenylhydrazone), Derivative of Glycolaldehyde *Anal*. Chem., **1955**, *27*, 1348-1349.

36. Ohgushi, M.; Nagayama, K.; Wada, A. Dextran-magnetite: a new relaxation reagent and its application to T_2 measurements in gel systems. *J. Magn. Reson.* **1978**, *29*, 599–601.

37. Huang**,** H. C.; Chang**,** P. Y.; Chang**,** K.; Chen**,** C.Y.; Lin**,** C.W.; Chen**,** J. H.; Mou**,** C.Y.; Chang, Z. F.; Chang, F. H. Formulation of novel lipid-coated magnetic nanoparticles as the probe for in vivo imaging. *J Biomed Sci.* **2009,** 16, 86

38. Chen, Z. P.; Xu, R. Z.; Zhang,Y.; Gu, N. Effects of Proteins from Culture Medium on Surface Property of Silanes- Functionalized Magnetic Nanoparticles. *Nanoscale Res Lett* **2009**, 4, 204–209

39. Das, M.; Mishra, D.; Maiti, T. K.; Basak, A.; Pramanik, P. Bio-functionalization of magnetite nanoparticles using an aminophosphonic acid coupling agent: new, ultradispersed, iron-oxide folate nanoconjugates for cancer-specific targeting. *Nanotechnology*, **2008**, *19***,** 415101

40. Das, M.; Mishra, D.; Dhak, P.; Gupta, S.; Maiti, T. K.; Basak, A.; Pramanik, P. Biofunctionalized, Phosphonate-Grafted, Ultrasmall Iron Oxide Nanoparticles for Combined Targeted Cancer Therapy and Multimodal Imaging; *Small* **2009,** 5, 2883-2893.